Modelling and Observing how Patterning the Cathode Catalyst Layer-Electrolyte Interface Influences the Power Density of a PEMFC

By

Sam Richard Eardley

A thesis submitted to
the University of Birmingham
for the degree of
DOCTOR OF PHILOSOPHY

Hydrogen Fuel Cells and their Fuels Research Group
School of Chemical Engineering
College of Engineering and Physical Sciences
University of Birmingham
September 2022

Abstract

To overcome the challenges faced by climate change and global warming, advances have to be made in renewable energy as we look to replace our dependence on fossil fuels as a primary energy source. One sector of renewable energy is Hydrogen Fuel Cells. Hydrogen Fuel Cells show promise, but currently can not make the world's energy demands. One way research has gone into Hydrogen Fuel Cells is through patterning the cathode-electrolyte interface of Polymer Exchange Membrane Fuel Cells (PEMFCs) to increase the active surface area of the interface, in an attempt to increase the amount of Oxygen Reduction at the interface.

In this PhD thesis, based on previous results achieved in research of patterned membranes in PEMFCs, the aim is to show that increasing the active surface area of the cathode-electrolyte interface via patterning can result in an improvement in power density output. Improving the power density is beneficial because it means more energy can be more quickly drawn from a fuel cell stack, making it easier to meet higher energy demands when required. Alternatively, the presence of a patterned interface, can allow for less platinum usage within the catalyst layers, reducing production costs, improving the power output to cost ratio.

Rather than building individual rigs for each patterned interface, an alternative approach was used of simulating models through a LiveLink between Matlab and

COMSOL Multiphysics, allowing multiple simulations to be run consecutively. The advantage of this is the time saved from running multiple models in quick succession in the same time it would take for very few experiments rigs to be built and run.

A variation in parameter will be used to generate an array of models with patterned interfaces differing in height and frequency of peaks, whilst making sure to maintain a constant volume of the catalyst layer and membrane, to ensure all results are a direct consequence of the patterned interface. It has been shown that increasing surface area has a positive influence on PEMFC performance. However, given it has also been shown that the patterned interfaces can help with water management at the cathode-electrolyte interface, multiple geometries will be generated and compared with one another. This is important, because finding an optimal geometry via simulations saves time, and can be immediately applied to real life experiments in the aim of obtaining improvements in power performance.

Lastly, roughness will be applied to the surface of the interfaces. This will provide a more realistic model, as opposed to having perfectly smooth interfaces. If it can be shown that the application of roughness has little impact on the power performance, it can be assumed that the models consisting of smooth interfaces are accurate to practical experiments.

Acknowledgements

All my life, I've known that I wanted to pursue a career in science. Observing the world around me, and trying to understand it has always been interesting to me. By the time of my early teens, I was particularly interested in renewable energy, and wanted to focus my attentions on a field of science that I knew I could say I had made a difference. It was still a long way in the future to be looking, but I knew even then that I wanted to eventually complete a PhD in the field of renewable energy.

However, when I became paralysed in 2007, I was no longer sure if that was even possible. That was, until I became increasingly interested in the work of Stephen Hawking. Although our disabilities differed on many levels, the fact it didn't stop him pursuing his love of physics was a significant inspiration to tell me that even though the life I previously had was gone, I could still do what I wanted in regards to my dream of getting my PhD.

I owe a massive thank you to the whole of the fuel cell group. Not just those at Birmingham, but everyone I met during the six years of my time as part of the CDT across all of the four other universities, Loughborough, Nottingham, UCL and Imperial College. However, there are a few in particular I would I like to thank individually. To Alex, Alex, Bea, Marcus, Oliver and Rhi, my original cohort that started my PhD journey with me. I'm a very introverted person, so having such welcoming

people made the whole experience so much easier for me. The fact that it was also whilst at an induction course in Athens probably helped as well! I also have to thank Oujen, Melissa, Abu and Pushpa, who lit up my day every time I saw them in room 119. I would also like to extend my greatest appreciation to Yang, who carried out experiment assessments of some of my simulated work. Something that I personally could not do, and which was very important to my research.

I'd like to thank everyone who has been part of the staff within the Chemical Engineering department during my time there. Especially to the IT department, who had to deal with my constant emails of frustration whenever there was a problem with connecting to the server, or there was an issue with my Matlab to COMSOL Multiphysics Livelink license, and John Hooper, who had the patience of a saint when dealing with my multiple concerns over the past six years.

Thank you to Shangfeng and James for being my supervisors. The guidance you both have given me throughout my time at Birmingham is greatly appreciated. Especially all the work James did in helping me understand how to use Matlab and COMSOL Multiphysics to do my modelling. Without their help, I definitely would still be stuck at square one. And thank you to the Engineering and Physical Sciences Research Council for funding my PhD.

Finally, thank you to my family. To my Mum, Dad, Sister Zoe, and my Brother-in-law, Joel, who have all had to endure my slow decline into delirium over the past six years. Especially my mum, who over the last two years has had to handle the on-going medical nightmare I have had since the start of 2021.

Contents

List of Figures

9

List of Tables

List of Publications

Conference Presentations

1. "Simulation of Patterned Cathode Catalyst Layer-Electrolyte Interface, with Gaussian Roughness, for Improved PEMFC Power Performance". 237th ECS Meeting with the 18th International Meeting on Chemical Sensors (IMCS 2020), 10-14th May 2020. ***Oral presentation. (Cancelled due to Covid-19)***

2. "Modelling of the Cathode-Membrane Interface for the Development of High Performance PEMFCs". CARISMA 2019. $27^{th}-30^{th}$ August 2019. ***Poster presentation.***

3. "Modelling of Patterned Catalyst-Electrolyte Interfaces for Improved PEMFC Performance". EFCF 2019: Low-Temp. FUEL CELLS, ELECTROLYSERS & H2 Processing. $2^{nd}-5^{th}$ July 2019. ***Oral presentation.***

4. "Modelling the Cathode's Patterned Catalyst Layer-Electrolyte Interface for Improved PEMFC Performance". H2FC SUPERGEN. $18^{th}-19^{th}$ 2018 ***Poster presentation (prize awarded).***

5. "Modelling the Cathode's Patterned Catalyst Layer-Electrolyte Interface for Improved PEMFC Performance". FCH2 2018 Hydrogen and Fuel Cell Technical conference. 14th March 2018. ***Poster presentation.***

Chapter 1

Introduction

1.1 Introduction

The industrial revolutions, which took place during the late 18th and early 19th century, are considered to be some of the most important periods in history in regards to advancements in the standard of living, and having a huge influence on modern day technology [37][38]. However, the observation that releasing carbon stored in fossil fuels, by combustion, to power this revolution, and the simultaneous increase in greenhouse gases, such as carbon dioxide, can't be seen as a coincidence. Since the invention of the steam engine, by James Watt in 1769 [39], the concentration of CO_2 in the atmosphere has increased from 280 to 412 ppm [40]. To give some context, over the 10,000 years prior to the industrial revolution, the concentration of CO_2 had only increased from approximately 265 ppm [41]. Not too surprisingly, it is clear that the two biggest culprits of greenhouse emissions, electricity and heat, and transportation [42], are heavily reliant on fossil fuels as their source of energy. However, there has been a shift in the market towards using fuel sources that are more environmentally friendly.
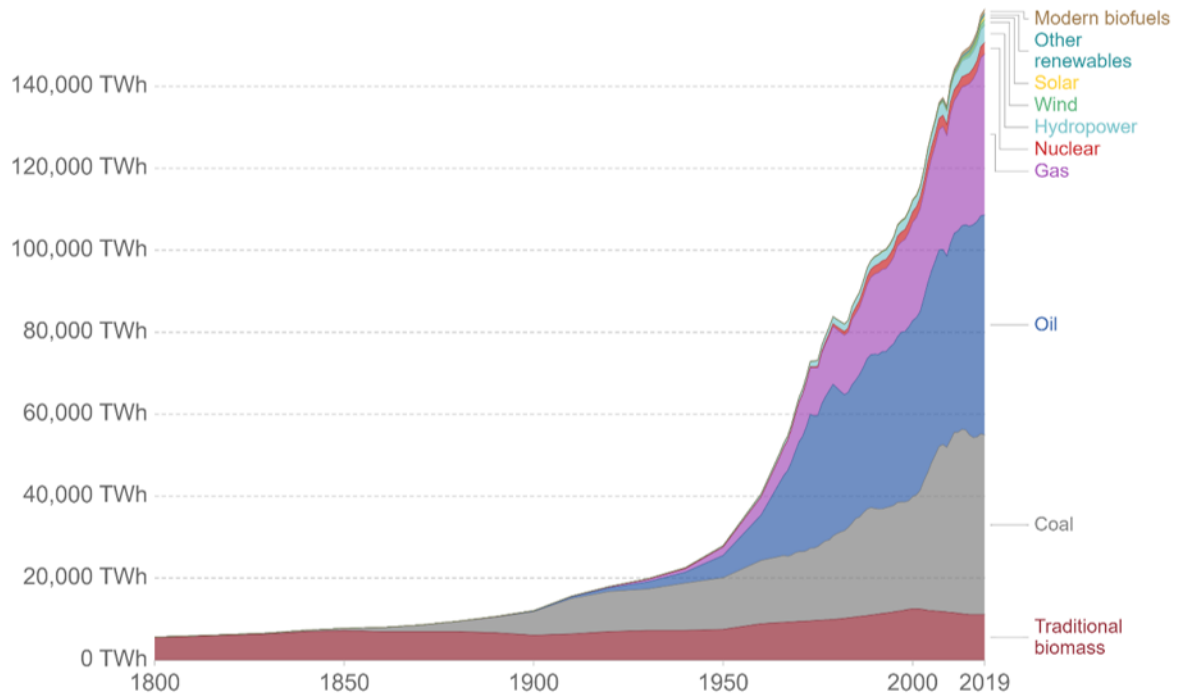
Figure 1.1: Chart Showing How The Consumption of Energy Sources has Changed Over the last 220 Years [1].

As shown in Figure 1.1, fossil fuels have played a huge role in the world's energy demands ever since the industrial revolutions. The consumption of fossil fuels allows energy to be supplied to different countries via their respective national grids. However, whenever there is a surplus of energy greater than what is demanded, this energy must be stored in a way, such that it can be easily supplied to the grid when it is needed.

The most common form of energy stored is 'Pumped Hydroelectric', where electricity is used to pump water up a reservoir. When the water is released from the reservoir, it flows down through a turbine, generating electricity [43]. Another alternative form of energy storage are 'Flywheels', where electricity is used to accelerate a flywheel,

which converts the energy into kinetic rotational energy. When the energy is required, the flywheel is released, so the spinning force of the flywheel can be used to generate electricity [44]. Batteries can also be used to store electricity, however, this requires very large batteries, which take up a lot of space, in order to store the amount of energy in question [45].

One potentially concerning aspect of renewable energy that has not been addressed yet is grid inertia. Grid inertia refers to the energy stored in large rotating generators and industrial motors, which have the tendency to keep rotating, providing a back-up source of power in the event of a power plant failure [46]. Grid inertia is a key component in the current grid in ensuring reliable power. This means as the grid shifts from using fossil fuels to power generators to modern renewable methods, there will be less inertia in the system, which could be a problem. A relatively newly researched way of storing energy is hydrogen. Hydrogen has the highest energy density, 100 MJ/kg, out of any other possible fuels. This is more than double that of gasoline and diesel, sitting at 45.8 and 45.3 MJ/kg respectively [47]. This alone makes it a very desirable energy storage medium. Additional, hydrogen is extremely abundant and when converting it to electricity, there are no greenhouse gas by-products, which were two of the main concerns with fossil fuels [48]. When needed, in order to convert the hydrogen back into electricity, the compressed hydrogen can be fed into a hydrogen fuel cell, which via two electrochemical reactions, can convert hydrogen and oxygen into electricity and water [49].

Compressed hydrogen would mainly be advantageous as an alternative to fossil fuels in refuelling commercial vehicles, since it can provide a similar mileage to fossil fuels, and has a comparable refuelling rate of approximately 3-5 minutes. Significantly

faster than it takes for plug-in electric vehicles to recharge [50]. Furthermore, fuel cells can be used in combined heat and power (CHP) to provide both electricity and heat to buildings, or even used as back-up power. This is particularly beneficial for the consumer, because not only are CHP systems a lot more energy efficient than relying on the national grid, at around 80% compared to 35-50% [51], but any waste heat can be used for heating, or in cooling apparatus.

Besides storing hydrogen as a compressed gas, hydrogen can also be stored as liquid hydrogen, by cooling below 33 K. This has been found to be more economical than compressed hydrogen for transporting hydrogen over long distances [52].

Hydrogen can also be stored in a solid state, such as in Metal Hydrides, where hydrogen is adsorbed and desorbed within a metal lattice. This has been shown to achieve a high volumetric density of hydrogen [53]. However, they are comparatively very heavy and expensive compared to other hydrogen storage options [54].

1.2   Hydrogen Fuel Cells

Depending on the desired functionality of the hydrogen fuel cell, and their operating temperature, ranging from 80-100°C (Polymer Electrolyte Membrane Fuel Cells) up to 800-1000°C (Solid Oxide Fuel Cells), there are a variety of different fuel cells that work best for these different requirements.

There are several different types of fuel cells, with varying names depending on the materials used, and the chosen fuel source. Solid Oxide Fuel Cells (SOFCs) operate at relatively very high temperature compared to other fuel cells, typically around 700-

1000°C [55], and are called so due to their solid oxide or ceramic electrolyte. SOFCs offer a number of advantages over other types of fuel cells, such as being able to achieve an efficiency of over 60%, with the current reported world record held by Elcogen's SOFC stack at 74% [56], the ability to function without requiring expensive catalysts such as platinum, due to their high operating temperatures, as well as being able to tolerate impurities being present, allowing for a less stringent protocol in purifying the hydrogen supply. However, the requirement of operating at high temperatures comes with its own drawbacks, as the materials used are thermally challenged, and resulting in high costs and complex fabrication techniques. Also, the high temperatures limit their practicality for portable applications and transportation [57], meaning they are mainly used for combined cycle power plant, cogeneration/trigeneration and residential applications.

Besides SOFCs, there are also Direct Methanol Fuel Cells (DMFCs), which operate at temperatures of roughly 50 to 120°C, and as the name suggests, are powered by methanol rather than hydrogen. This is a significant advantage when it comes to transportation, since it is much easier to transport methanol, than it is to transport hydrogen. However, because of methanol crossover, which results in wasted fuel, methanol can only be fed as a weak solution, decreasing efficiency to around 30 to 40% [58]. DMFCs are limited in the power they can produce, only capable of producing a small amount of power over a long duration of time. This makes them unsuitable for large vehicles, but ideal for smaller vehicles such as forklifts and tuggers [59].

There are also Molten Carbonate Fuel Cells (MCFCs), which are high temperature fuel cells consisting of an electrolyte composed of a mixture of molten carbonate salts suspended in a porous, chemically inert lithium aluminium oxide matrix. Costs can

be reduced by using non-precious metals for the anode and cathode, because of operating at high temperature of 650°C [60]. MCFCs can reach efficiencies of around 65%, and due to their high temperature operating conditions, an external reformer to convert fuels such as biogas and natural gas to hydrogen, is not required, as other fuel sources such as methanol and other light hydrocarbons can be converted into hydrogen within the fuel cell, saving costs. However, the high temperatures and corrosive electrolyte accelerates breakdown of components, reducing the life of the cell [61].

Alkaline Fuel Cells (AFCs), which operate at ambient temperatures up to 90°C, were one of the first fuel cell technologies developed, where they were used in the US Space programme. Unlike SOFCs or DMFCs, which use a solid oxide or polymer electrolyte respectively, AFCs use a solution of potassium hydroxide in water as the electrolyte. Although they show a high efficiency of 55 to 60%, a major drawback to them is the degradation of the electrolyte due to carbon dioxide, meaning AFCs typically require operating in pure oxygen [62]. Although they were the first fuel cells to be used in vehicular applications, they have since seen reduced usage, having been largely displaced in favour of Polymer Electrolyte Membrane Fuel Cells (PEMFCs) [63].

A fuel cell that has a greater potential for being suitable for portable applications and transportation are Polymer Electrolyte Membrane Fuel Cells (PEMFCs) [64]. Below is a schematic illustration of a PEMFC which operates in the 80-100°C temperature range. Within a PEMFC, there are four main components. An anode and cathode, separated by a polymer electrolyte membrane, all of which are enclosed in bipolar plates.
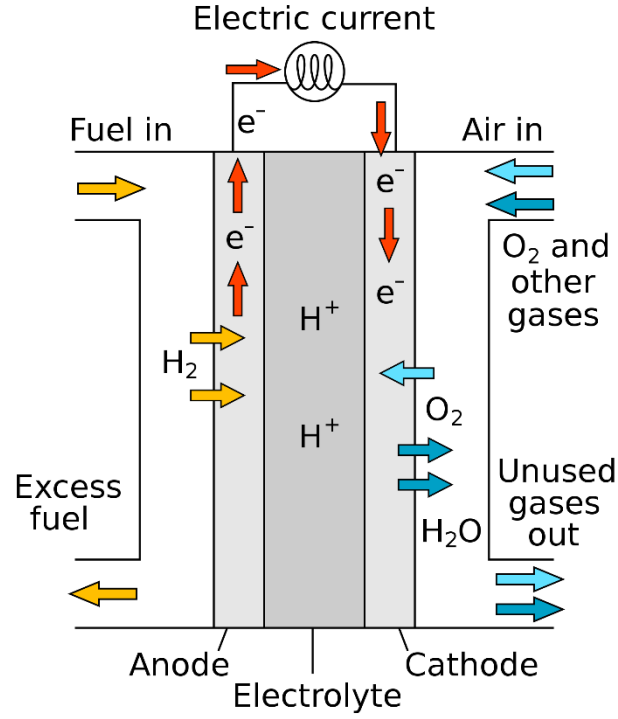
Figure 1.2: Schematic Illustration of a PEMFC [2].

There are two main chemical reactions that occur within the fuel cell.

1. Hydrogen Oxidation Reaction (HOR), at the anode:

$$2H_{2(g)} \rightarrow 4H^+_{(aq)} + 4e^-$$ (1.1)

2. Oxygen Reduction Reaction (ORR), at the cathode:

$$4H^+_{(aq)} + O_{2(g)} + 4e^- \rightarrow 2H_2O_{(l)}$$ (1.2)
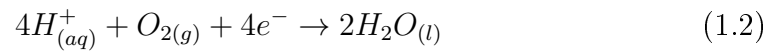
This gives an overall equation of:

$$2H_{2(g)} + O_{2(g)} \rightarrow 2H_2O_{(l)}$$ (1.3)

The electrons that are separated from the hydrogen ions, via HOR at the anode pass through an electrical circuit, via the bipolar plates, which creates a usable electric circuit, which can be directed into the national grid, or on a smaller scale, directly into an electrical device. The electrons pass through the electrical circuit until they reach the cathode, where they rejoin up with the hydrogen ions, which have passed through the polymer electrolyte membrane, and oxygen, which flows through the gas diffusion layer (GDL) of the cathode. This results in a by-product of water, which ideally completely leaves the system [65].

Each of the four key components have a specific function, which requires materials with specific characteristics. The anode and cathode both need to be excellent electrical conductors, but also very poor ionic conductors. Conversely, the membrane material needs to be an excellent ionic conductor, whilst being a terrible electrical conductor. This is important, as any electrons that cross through the membrane are wasted, since they would not pass through the electrical circuit via the bipolar plates. Similarly, the membrane should be impermeable to hydrogen molecules. Otherwise, hydrogen would pass through the membrane without undergoing Hydrogen Oxidation, and thus not contributing to the electrical output. This is known as Hydrogen Crossover [66]. As implied by the name, the GDL's primary role is to uniformly distribute reactant gases to utilize the whole area of the catalyst layer effectively. However, additionally, the GDL must also have effective transport properties, such as low interfacial contact resistance, for the removal of the water by-product from the active area to the flow field, and due to the compressive load of the assembly, must have high mechanical integrity to provide structural support to the membrane and catalyst layer [67].

With all these characteristics in mind, we can look at which materials would be most suitable for each component. For both the anode and cathode, the only important regions are their surfaces, since these are the only regions where the Hydrogen Oxidation and Oxygen Reduction reactions will be occurring. As such, this means we can use a relatively cheap electrically conductive material for the bulk of the electrodes, but with a very thin layer of another material on their surfaces that can act as a catalyst for these two reactions. An example of a suitable material for the bulk component of the electrodes, that meets all these requirements, and has been used is carbon black Vulcan XC-72R [68]. The best candidate for a material used as a catalyst is platinum, due to it being an excellent material for allowing adsorption of hydrogen ions to its surface, but does not require too much energy for the desorption of the hydrogen. Nafion is the prime candidate of choice for the electrolyte, due to its ability to permit hydrogen ion transport whilst preventing electron conduction [69]. There are many different types of Nafion that have been experimented with, which are characterized by the three numbers that proceed 'Nafion'. For example, the most widely used type of Nafion for electrolytes in PEMFCs is Nafion 212 [70]. The number '212' indicates an electrolyte with 2100 g/mol equivalent weight and 0.002 inches in thickness [71]. The bipolar plates need to be very electrically conductive, highly chemically resistant to operating conditions, and highly thermally conductive for better heat transfer across the cell [72]. A wide range of metals fit these criteria, however, an assessment by Ballard et al [73], showed carbon bipolar plates are superior due to providing better performance at a lower cost and with longer product lifetimes.

The main drawbacks of hydrogen fuel cells can be allocated into two categories. Price and efficiency. The main culprit for the high price is the need for using platinum as a catalyst for the two electrochemical reactions. It has been previously stated why

platinum is such a good choice for the catalyst material. As shown by the volcano plot below, there are several options for catalyst materials, however, platinum is clearly the best.
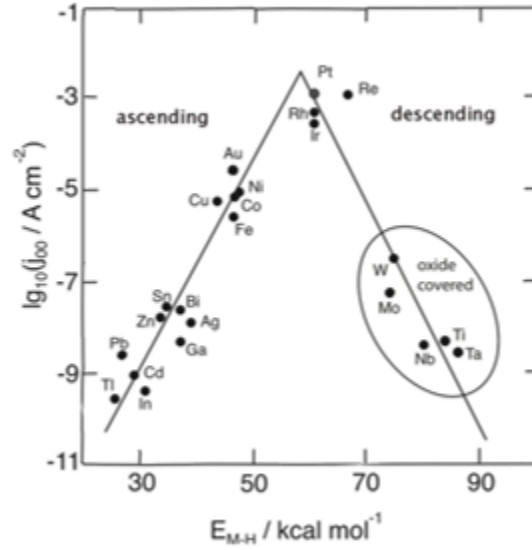
Figure 1.3: Volcano Plot of all the Viable Catalyst Materials for the ORR at the Cathode [3].

This would not be a huge problem, if it was not for there only being a finite amount of platinum available [74], and thus its resultantly very high price, sitting at roughly £25.83 per gram [75].

As such, in an attempt to reduce the amount of platinum used for the catalyst, platinum can be grown on a, cheaper, metal substrate. Since the electrochemical reactions occurring with the fuel cell happen at the surface, the small performance drop of the fuel cell by using this money saving technique is worth it overall [76].

1.3   PEMFC Polarisation

The standard Gibbs free energy change ($\Delta \mathrm{G}^{\Theta}_{298K}$) of the formation of liquid water from hydrogen and oxygen gases, is -237KJmol^{-1} (at standard temperature and pressure, STD). Using the below equation, we can rearrange it to solve for E^{Θ} , the standard cell potential of 1.23V [77].

$$\Delta G^{\Theta}_{298K} = RTln(K_{eq}) = -nFE^{\Theta}_{298K} \tag{1.4}$$

The theoretical maximum cell potential (E_{Nernst}) can be calculated by rearranging this equation and factoring in the empirically derived temperature dependency of E^{Θ} [78].

$$E_{Nerst} = E^{\Theta}_{298.15K} - 0.000846(T - 298.15) + \frac{RT}{nF}ln(pH_2{}^2.pO_2) \tag{1.5}$$

Given under STD, the electrochemical activities of O_2 and H_2 are considered to be a value of 1, and since liquid H_2O is in abundance, the activity is conventionally taken as unity.

However, the Nernst potential is only the theoretical maximum cell potential, and doesn't account for any cell potential loses as current is drawn from the PEMFC, as shown in Figure 1.4.

Losses in cell potential, overpotential, can be categorized into three reasons [79]:

- Activation Lose

- Ohmic Resistance

- Mass Transport

Activation lose is the initial losses resulting from overpotential related to the kinetics of HOR and ORR ($\eta_{ORR/HOR}$) at the surface of the electrodes. Both the HOR and ORR follow in accordance with the Bulter-Volmer kinetics on a heterogeneous catalyst as per the following equation [80]:

$$i = i_0 \left(\left(\frac{C_{Red}}{C_{Red}^0} \right) exp \left[\frac{\alpha nF\eta}{RT} \right] - \left(\frac{C_{Ox}}{C_{Ox}^0} \right) exp \left[\frac{-(1-\alpha)nF\eta}{RT} \right] \right) \qquad (1.6)$$

Ohmic resistance is the internal resistance of the PEMFC. That is to say, a material's opposition to the flow of electric current [81]. Therefore, as you increase the electrical current drawn, you decrease the available voltage. Ohmic resistance can be roughly calculated by taking the inverse of the gradient of the straight part of a polarisation curve, after the region of activation lose, and before the region of mass transport losses,

$$\frac{1}{R} = \frac{\Delta I}{\Delta V} \qquad (1.7)$$

Mass transport losses occur when there is an insufficient supply of reactants at the surface of the electrodes within the fuel cell. The porous structure of the GDL can also contribute to mass transport losses, since the catalytic material suffers from oxygen depletion since it is mainly located in the interior of the carbon support, as well as hydrogen crossover through the membrane, meaning less hydrogen oxidation and oxygen reduction at the anode and cathode respectively [82].

At a limiting current (maximum), the concentration at the catalyst surface is practically zero, as the reactants are consumed as soon as they are supplied to the surface [83].

When talking about overpotential, that is referring to the combined total of all three of the types of voltage losses,

Overpotential = Activation Losses + Ohmic Losses + Mass Transport Losses

1.4   Polarisation Curve

As previously stated above. There are two main reactions that occur in a hydrogen fuel cell. In the case for a PEMFC, there is the HOR at the anode, and the ORR at the cathode. The best way to improve the overall performance of the fuel cell is to improve the rate and efficiency of these two reactions. However, the ORR is five to six orders of magnitude slower than the HOR, making the ORR the rate limiting step [84]. This means there is little emphasis on speeding up the HOR, if the ORR is so substantially slower. Consequently, almost all research is focused on improving the ORR.
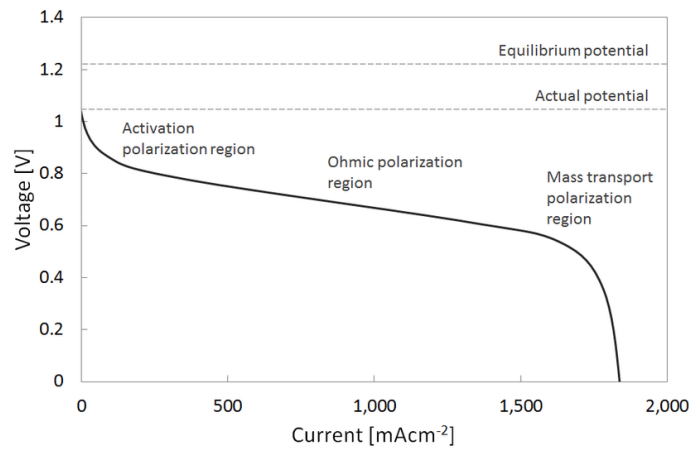
Figure 1.4: A typical polarisation curve for PEMFCs showing the major losses which explain the deviations in measured cell potential compared to the theoretical Nernst equation [4].

Another reason for the ORR being significantly poorer than the HOR is the degradation of the reaction interface over time, which can be caused by a combination of chemical, mechanical and thermal stressors [85]. It could also be due to the build-up of water on the surface of the interface [86]. As displayed in equation 1.3, the only by-product of the two reactions is water, which is obviously good from an environmental front. However, if this water does not leave the system upon formation, and instead builds up on the surface of the catalyst layer-electrolyte interface, where the ORR takes place, this can reduce the active surface area of the interface, and therefore reduce the rate of the ORR.

There are two main ways the ORR can be improved. One way is finding different ways to utilize platinum electrocatalyst on a carbon support [87]. The other is to alter the morphology, or patterning, of the catalyst layer at the cathode, to increase the active surface area of the interface with the membrane, to increase the rate of the ORR [88]. Simultaneously, if a patterned morphology can be designed that also benefits the flow of water away from the interface, this will also have a positive effect on the ORR.

On a more quantitative level, increasing the rate of the ORR can be seen as improving the overall power performance of the PEMFC. This can be achieved by either increasing the current density, and/or reducing the overpotential. It is proposed that altering the morphology of the interface where the ORR occurs, via patterning, may help achieve these targets.

1.5   Motivations

There has been interest into the development of patterned ORR interfaces, believing that characteristics such as an increased active surface area could yield improved fuel cell performance. This has resulted in a growth in literature focusing on the experimental results of modifying the morphology for the ORR interface. However, although there has been research into modelling PEMFCs with planar interfaces via computer simulations, there has not been any studies into simulating PEMFC with patterned morphologies. This blank space in the field of patterned interfaces in PEMFCs is the motivation behind this PhD thesis.

1.6   Outline of the PhD thesis

The objective of this thesis is to build on the previous research done into attempting to improve the Oxygen Reduction Reaction, by finding the optimal patterned cathode catalyst-membrane interface design to achieve the best possible ORR rate, and thus, the best power performance.

After a brief introduction to the context and fuel cell principles in Chapter 1, Chapter 2 will review recent progress in the field of practical patterning of PEMFCs with the goal of improving water management, and optimizing for improved power performance.

Chapter 3 will continue this review, looking into recent developments in the simulations of fuel cells, addressing the advantages and disadvantages of different approaches.

Chapter 4 will discuss how we have used modelling simulations to compute data for a planar model which does not consist of any additional patterning to the ORR interface, where all the data collected will be used as a baseline for comparing patterned morphologies with. This will also be compared to practical experimental data.

Chapter 5 will observe how patterning the interface with a Prismatic morphology can impact the power performance of a PEMFC, looking specifically at how the power performance is influenced by changes in surface area, and comparing results with the planar model.

Chapter 6 will continue with this analysis, but with more complex geometries, allowing for more thorough comparison between them, to determine which can provide the best power performance.

Chapter 7 adds a layer of realism to the model, with the inclusion of roughness to the models. A comparison will be made to see how roughness improves or worsens results compared to their non-rough counterparts.

Chapter 8 will conclude the thesis, discussing the overall results obtained, and what meaningful insight can be taken from these results, that can be used in future research.

Chapter 2

Literature Review

This chapter will firstly look more deeply into the reaction taking place at the cathode of the PEMFC, the Oxygen Reduction Reaction (ORR), showing how variables and parameters can be adjusted to maximize the ORR for optimal fuel cell performance. By drawing inspiration from previously carried out research studies, the goal is to provide a better understanding of how altering the morphology to the cathode/electrolyte interface, impacts the fuel cell power performance and can be optimized.

The two reactions taking place at the anode and the cathode [89] are fundamental to the functionality of a PEMFC. At the anode, the Hydrogen Oxidation Reaction (HOR) takes place [90] as shown in equation 1.1, where hydrogen molecules are split, as the hydride ions are separated from their electrons, as also shown in Equation 2.1.

$$2H_{2(g)} \rightarrow 4H^{+}_{(aq)} + 4e^{-} \tag{2.1}$$

The electrons flow across an electrical circuit via the external circuit, whilst the hydrogen ions pass through the semi-permeable electrolyte membrane. The electrons and hydrogen ions rejoin with one another at the cathode, at the other end of the membrane, where they react with oxygen to form a sole by-product of liquid water. This is known as the Oxygen Reduction Reaction (ORR) [91], as shown in equation 1.2 and also below.

$$4H^+_{(aq)} + O_{2(g)} + 4e^- \rightarrow 2H_2O_{(l)} \tag{2.2}$$
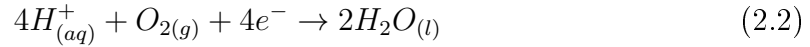
The ORR is five to six orders of magnitude slower than the HOR [92][93], making it the rate limiting step [94]. This means that even if we have significantly increased the rate of the HOR, it can not make much difference to the overall performance of the PEMFC, because the slow rate of the ORR would be holding it back. As such, most research is focused on improving the performance at the cathode side, both experimentally, and through numerical simulation methods.

2.1   Electrochemical Reactions at the Cathode

For the ORR to occur, there are three key factors that must be in place. There needs to be all the reactants present, i.e. oxygen, hydrogen ions and electrons, there needs to be optimal operating conditions, e.g. temperature and humidity [95], and there must also be an interface for which the reaction can occur. This is the interface between the polymer electrolyte membrane and the cathode. Below is a schematic showing the component layers of a PEMFC, with the interface where the ORR occurs highlighted in yellow.
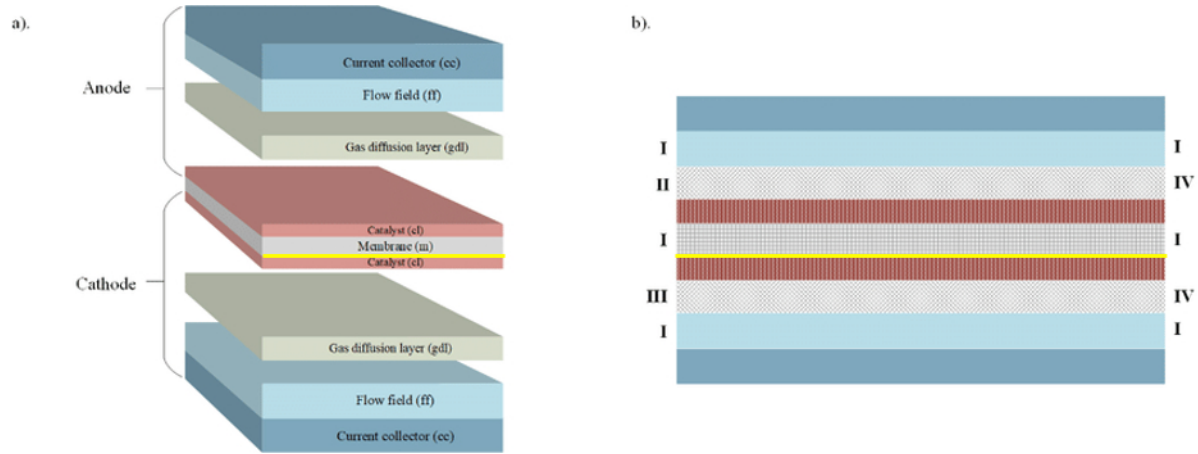
Figure 2.1: Schematic view of a single PEMFC (a) components of the PEMFC, (b) computational domains with boundaries: I-insulation/wall, II-anode inlet, III-cathode inlet, and IV-outlets [5].

Since the ORR is the rate limiting step, in order to improve the performance of PEMFCs, it is logical to prioritize improving the ORR.

There are a number of ways to improve the ORR. Firstly, research has been carried out into the material properties of the electrode. For example, different materials used for the substrate and catalyst layer, and how the catalyst layer is applied to the substrate, have been proven to impact the fuel cell performance [96]. Secondly, by looking into improvements in the membrane [97]. Nafion 212 is widely regarded as the best membrane for a PEMFC because of its excellent ionic conductivity, whilst being a membrane with very poor electrical conductivity [98]. By reducing the thickness of the membrane, the rate of ion diffusion through the membrane can be increased. However, this could lead to failure to the structural integrity of the membrane if it is too thin [99]. Thirdly, how the management of the system operating conditions, such as humidity, pressure and temperature, and how they are used to control water management at the ORR reaction interface, can affect the fuel cell performance [100].

The other proposed idea for improving the fuel cell performance, which is the main focus of this thesis, is by increasing the active surface area of the interface by patterning the morphology of the membrane-cathode interface [101]. By increasing the active surface area, more reactants can meet at the interface and a high fuel cell power performance can be achieved.

2.2 Interface Engineering for Power Performance Improvement

One of the main ways the ORR interface can be engineered for improved power performance is to increase the total ORR rate by increasing the active surface area of the interface. One way to do this is by fabricating membranes with patterned morphologies [102].
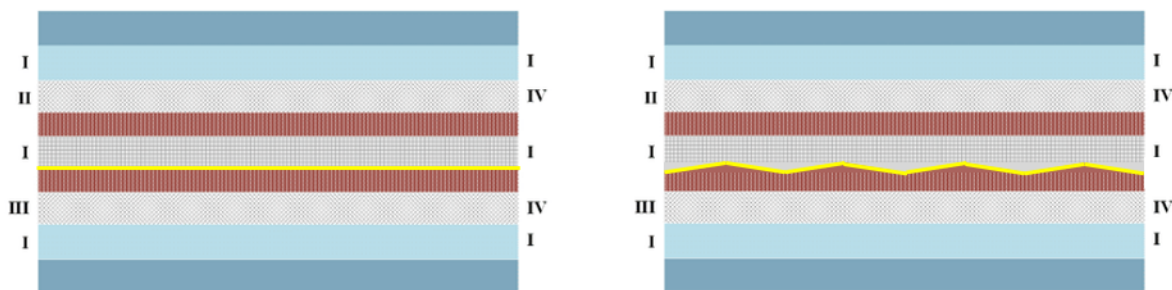
Figure 2.2: Schematic of a PEMFC with a planar interface compared to the PEMFC with a patterned interface.

Research has been conducted into this for nearly 20 years, with one research study published in 2003, carried out by K Shah et al., [103] looked into patterning miniature hydrogen-air proton exchange membranes by using a variety of different conventional

and non-conventional techniques. Over the course of these 20 years, the understanding of how patterning the ORR interface improves performance has increased, and so how to modify the morphology of the interface optimally for the best results. There are several variables that can determine how a patterned interface fuel cell can be compared to its planar counterpart, such as morphology, fabrication technique and operating conditions, making it difficult to compare different research studies with one another. However, most studies have shown improvements in both the peak power density and current density within a range of 10-25% and 10-40% respectively [10][12][104][17][105].

There are several different fabrication techniques available to be used. Each of them comes with their own advantages and disadvantages. This chapter will review the reported fabrication techniques reported so far with the power performance improvement.

2.2.1   Silicone Moulding

Injection Silicone Moulding (ISM) is an easy and flexible moulding practice that allows for the fabrication of structures of varying complexity [106]. It requires an original design to be made, which is placed within a moulding chamber. The silicone is then poured around the designed component and allowed to set. After removing the original design component, there is now a reusable silicone mould, that can be used to repeatedly make replicas of the original design [107]. Whilst silicone moulding has several advantages, such as the aforementioned flexibility and versatility, it is held back by the price of the silicone, which averages at $3131 per metric ton over the past three months [108], compared to other options, such as latex, which costs only

$2070 on average throughout 2021 [109]. There is also a limitation to the number of times that a silicone mould can be used before recurring defects in the mould start to present themselves.
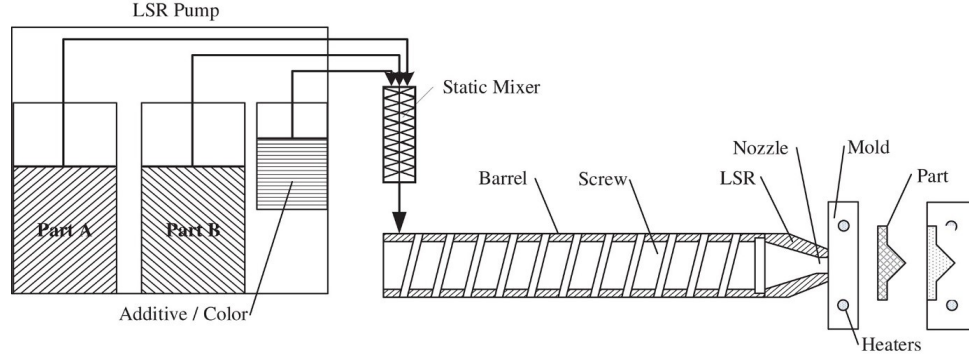
Figure 2.3: Injection silicone molding schematic [6].

Zhou et. al, in 2006, used the silicone moulding technique to fabricate a membrane interface consisting of 3 x 3 x 1.4 μm, 3 x 3 x 1.9 μm and 3 x 3 x 3.7 μm indented cubes with varying depths. The MEA test showed an improvement in power density from 127 mW/cm^2 to 220, 225 and 219 mW/cm^2 respectively, or an increase of 73.2%, 77.2% and 72.4% respectively [7].
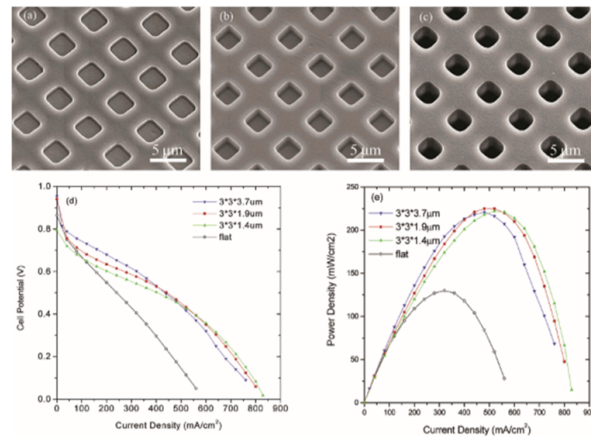
Figure 2.4: SEM images of the three patterned membrane samples fabricated via silicone moulding (a) 3 x 3 x 1.4 μm, (b) 3 x 3 x 1.9 μm, (c) 3 x 3 x 3.7 μm, their respective polarisation curves (d) and their power density curves (e) [7].

Compression Silicone Moulding (CSM) is an alternative to ISM which rather than filling a specifically shaped chamber with the casting material and letting it set, features the material being placed within a compression mechanism, and is quickly pressed into shape.

CSM offers many advantages over ISM, such as resulting in the constructed components having stronger mechanical strength, with fewer internal defects such as flow and knit lines. There is also a greater degree of flexibility in component design, and is a lot more cost effective. Crucially, CSM is not viable for manufacturing complex components, and since the patterned Nafion membranes are dealing on a nanoscale, this makes CSM difficult to be considered a viable technique moving forward [110].
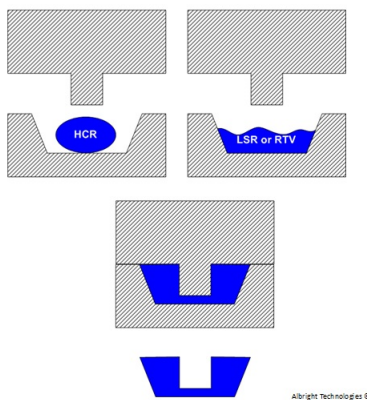
Figure 2.5: Schematic of Compressed Silicone Moulding [8].

2.2.2   Thermal Lithography

An alternative to the silicone moulding method is thermal lithography [111], which uses a very fine heated tip to heat up, decompose and evaporate parts of the surface of the membrane to create a patterned interface. The main benefits of using thermal lithography over other fabrication techniques is that the tip used to pattern

the interface, can also be used to inspect the surface morphology via atom probe microscopy [112], and due to the extremely small tip size used, the accuracy of the resolution is very high, resulting in patterned interfaces as fine as less than 10 μm. This is achieved whilst causing no damage to the interface material from a charge particle beam.
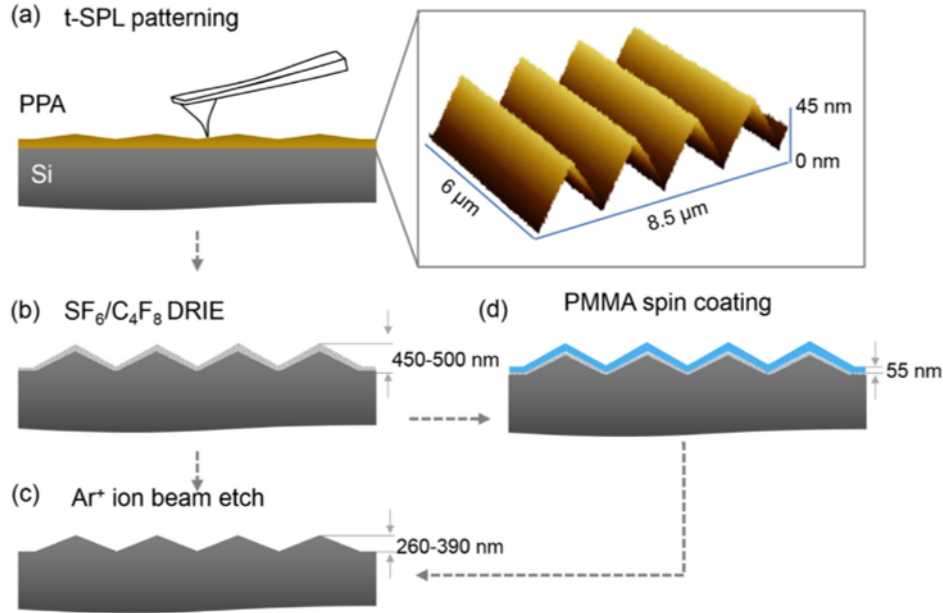
Figure 2.6: Schematic of the process flow of ion beam smoothening of the t-SPL pattern transferred in silicon: (a) t-SPL pattern in 72 nm thick PPA film. The depth of the PPA pattern is 45 nm from AFM measurements, (b) PPA pattern transfer into Si using SF6/C4F8DRIE [9].

As great as thermal lithography sounds, it does have its limitations. The speed of the procedure is restricted by the mechanical scan movement of the cantilever in regards to writing speed, limiting itself to only a few millimetres per second. Also, due to friction and contamination during patterning and imaging, the tip can deteriorate, reducing the attainable resolution. Thus, regular exchange of the cantilever is an expensive requirement. There are also complicated calculations required for determining the tip-sample contact temperature, since it is dependent on the thermal

boundary resistance of the materials involved, the tip geometry, and the roughness, which varies between samples, and changes during patterning [113]. These make the thermal lithography a good method for research, but very difficult for practical applications due to the very high cost and the low fabrication speed.

Masato Aizawa et. al, [114] in 2010, patterned pillar structured membranes via thermal lithography, with pillars of varying heights. Whilst they found a reduction in performance for 3.4 μm tall pillars, they experienced superior results, compared to unaltered interfaces, for the 6.7 and 10 μm tall pillars, with the latter showing a 6-11% improvement in current density.
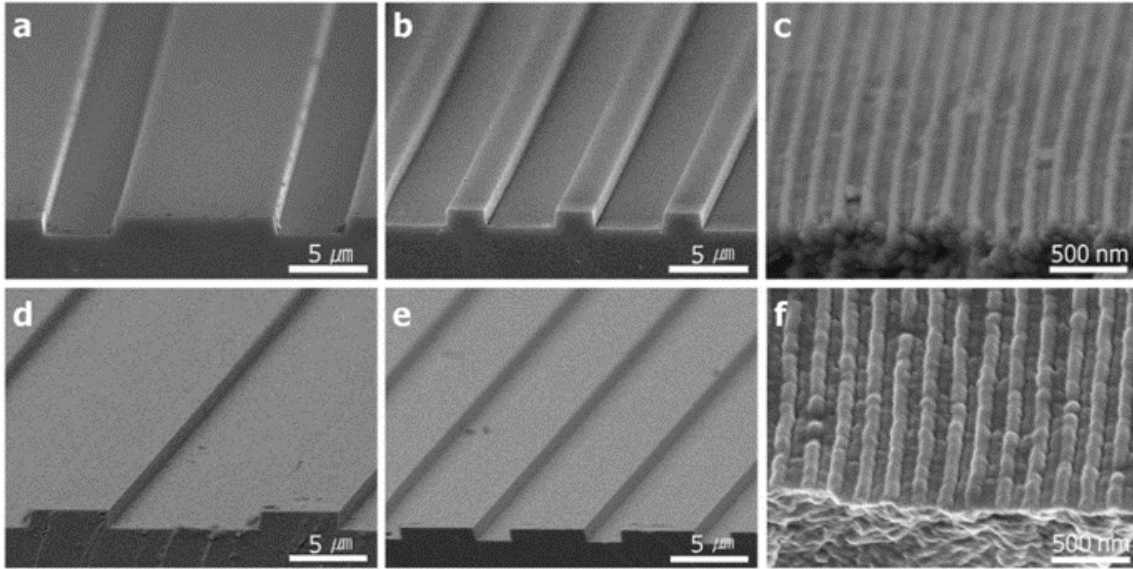
Figure 2.7: FE-SEM images of (a-c) the master mould surfaces and (d-f) the replicated membrane surfaces[10].

As opposed to pillars, in 2012, Bae et al [10], reported enhanced power performance by using thermal imprint lithography to generate a line-pattern on the top of Nafion membrane for PEMFCs.

The characteristics of the patterned membrane and the power performance obtained are listed in Table 2.1. As can be seen, patterning the membranes resulted in an, as expected, increase in the specific surface area of the membranes. On a micro-scale, this yielded an improvement in outcome performance, with a shown improvement of 30% and 25% in the current density and maximum power density (Figure 2.8) respectively, from an increase in specific surface area of 29%. On a nano-scale, although they were able to increase the specific surface area by 70%, they actually recorded a reduction in performance of 8% and 10% in the current density and maximum power density respectively. This is reflected in the resultant polarisation curves for pristine and each of the patterned membranes. This reduced performance in the nano-scale patterned membrane is apparently due to the mismatch in the size between the line pattern and the catalyst particles. Since the spacings of the line pattern, 90 nm, was smaller than the conventional agglomerate size of the Pt/C catalyst particles used, which had an average diameter of around 200-500 nm, the catalyst particles were too big to fit in the gaps, resulting in a poor interface between the catalyst and the membrane.

Table 2.1: Characteristics of the electrolyte membranes and electrochemical properties in the prepared MEA.

Properties	Pristine	MP1	MP2	NP
Line pattern (width/spacing/height)	None	5/10/1 μm	5/2/1 μm	110/90/70 nm
Specific surface area	1.00	1.13	1.29	1.70
Current density at 0.6V [Acm^{-2}]	0.77	0.86	1.00	0.71
Maximum power density [Wcm^{-2}]	0.56	0.61	0.70	0.50
R_Ω[Ωcm^2]	0.079	0.067	0.061	0.083
R_C[Ωcm^2]	0.208	0.193	0.191	0.207
ESA [m^{2}g^{-1}]	32.9	32.4	32.3	32.8
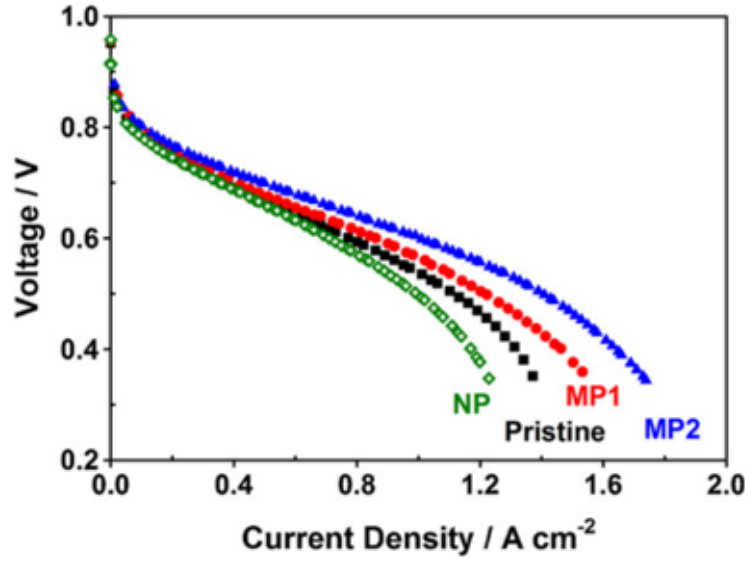
Figure 2.8: Polarisation curves of the MEAs [10].

2.2.3   Hot Embossing

Hot embossing involves the use of heat and force to press a master mold into a polymer substrate, transferring the inverse structure of the master mold into the polymer substrate [115].

The master mold can be used multiple times to quickly generate many patterned polymer substrates, making hot embossing suitable for mass production. Whilst it is very straightforward, one of the major drawbacks of using hot embossing is the time and relatively high costs associated with the fabrication of the master mould [116]. The required features of the master mould, e.g. lifetime, or precision of structural features, will determine which fabrication technique is used to make the mould.

The micro-milling [117] method has been commonly used with a miniature drill bit to carve out structures to make a strong master mould, that can be reused many times.

However, due to the large-scale size of the drill bit (about 25 μm), it is not suitable for making moulds with very small nanoscale structures.

The master moulds are typically made from a range of polymers. For example, poly-methyl methacrylate is widely used because it is transparent and can be moulded at lower temperatures compared to other substances. As the polymer is heated to its glass transition temperature, Tg, it changes from being hard and brittle, to softer and more flexible. As the polymer is heated above its Tg [118], it becomes softer, and can flow into the mould during the embossing process.

There are four key steps to fabricate a patterned membrane by using the hot embossing method: heating, embossing, cooling and demolding [119] (Figure 2.9).
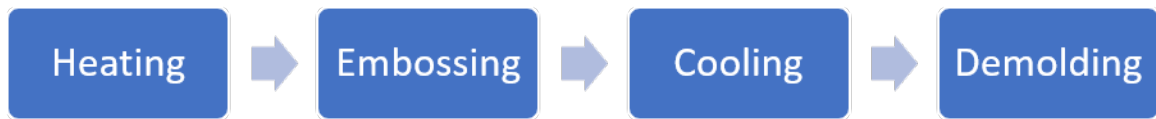
Figure 2.9: Hot Embossing Flowchart.

The detailed steps are schematically shown in Figure 2.10. In the heating step, the master mould and polymer substrate are independently heated in a vacuum chamber to just above the glass transition temperature of the substrate. This takes place in the vacuum, to remove gasses trapped in between the mould and the substrate, as well as to remove any water vapour that has evaporated out of the substrate.

In the embossing step, a controlled force is used to press the substrate and mould together. The force and temperature are kept constant for a set amount of time.

In the cooling step, the system is cooled below the glass transition temperature of the polymer, so that the substrate returns to a rigid state.

Finally, in the demoulding step, the mould and polymer are separated from one another. This has to be done very carefully, due to the large shear and friction forces that the master mould acts on the polymer substrate.
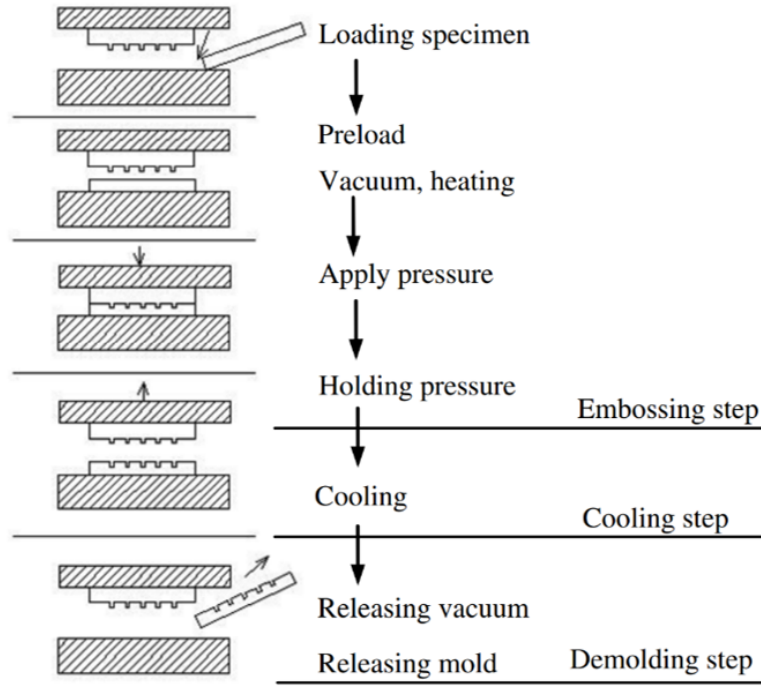
Figure 2.10: Schematic showing the Patterned Membrane fabrication process via Hot Embossing [11].

In 2010, Yildrim et al [12], fabricated linearly patterned Nafion 117 membranes by using this hot embossing method. Improved power density performance was compared to the normal unpatterned membranes, increasing from 205 mW/cm^2 to 230 mW/cm^2 (Figure 2.11). They ascribed this improvement to the increased catalyst utilization, and also due to the hot embossing treatment making the structure more compact, reducing membrane swelling.
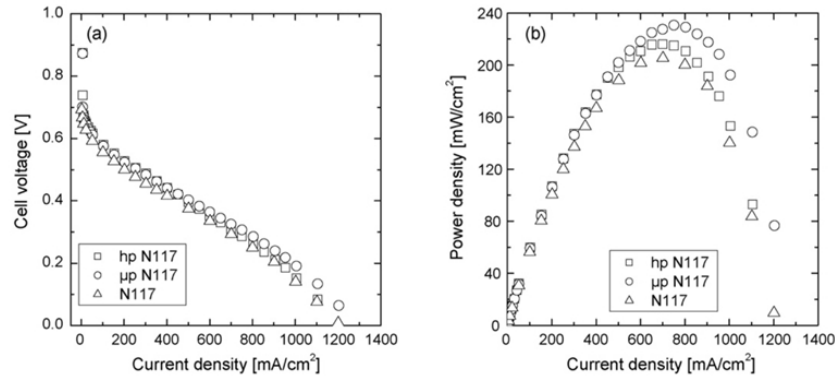
Figure 2.11: (a) Polarisation and (b) Power Density curves of mirco-patterned (μp), heat and pressure treated (hp) and normal N117 membranes [12].

2.2.4   Plasma Etching

Wet, or isotropic etching uses liquid chemicals to etch away a material, with a photoresist mask used to cover regions of the material from the chemicals. This, in theory, means only the unmasked region of the material is etched away, leaving the patterned material as desired. However, the chemicals used in wet etching can cause horizontal etching, seen as an undercut of the material underneath the edges of the mask, making it difficult to have detailed patterned accurately fabricated [120]. Thus, a superior alternative to wet etching is dry etching, e.g., using plasma instead of chemicals to etch away the undesired material [121].

Plasma etching involves a material being bombarded with ions in plasma. Unlike the wet etching process, the plasma causes the removal of material in only one direction.

Compared to other fabrication techniques, such as thermal lithography and hot embossing, plasma etching is relatively slow, at a rate of 100-1000 nm/min depending
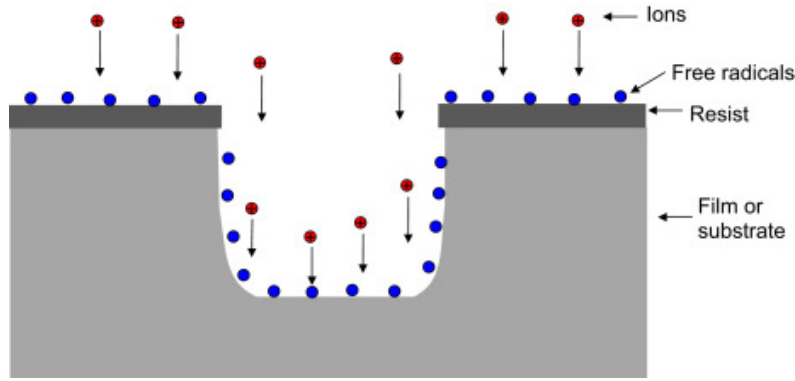
Figure 2.12: Schematic showing the Etching of a film using Plasma [13].

on temperature and pressure (19-26 nm/s for etching Nafion with a combination of oxygen and trifluoromethane gas plasma). Specifically, for etching Nafion, it appears the etching rate is independent of temperature, and a slight reduction in the etching rate as pressure is increased [122].

However, the plasma etching process can achieve a uniform modification of the membrane over a large area, without damaging the master mould, because it is a non-contact based method [15][123][124].

In 2010, Deshmukh et. al [14], used plasma etching to imprint parallel trenches, 55 μm apart with width and height of 40 μm and 25 μm respectively, into a Nafion 1135 membrane (Figure 2.13). Results showed an improvement in not only current and power density at elevated temperatures, measured up to 80°C, but also significant benefits to the performance of the fuel cells at higher humidities. This is thought to be due to the nature of the parallel trenches that provide a route for water produced from the ORR to escape via these channels, rather than diffusing through the cathode and blocking the pathways of the oxygen trying to reach the catalyst surface.
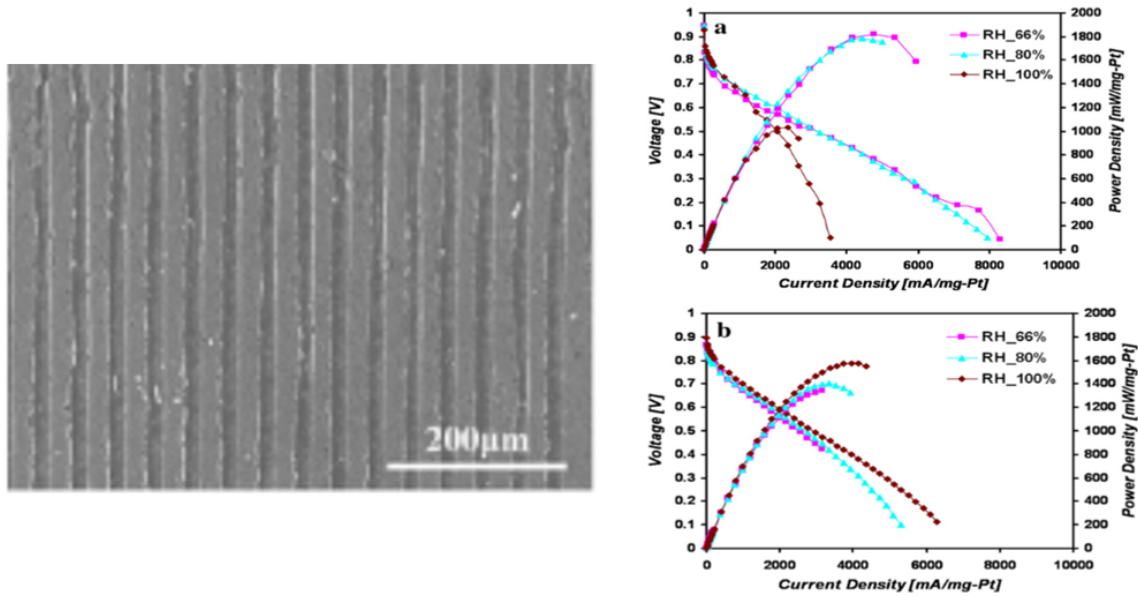
Figure 2.13: SEM image of the Linear-patterned membrane, and the polarisation curves/power density curves of the patterned sample at varying temperature and humidity (a), (b) [14].

Rather than generating line-patterned membranes, Seol et. al [15], in 2021, generated membranes with an array of microholes via the plasma etching process (Figure 2.14).

Four MEAs were tested. Three MEAs consisting of the patterned membranes, and a reference conventional MEA. Each of the three patterned membranes consisted of microholes, with 40 μm spacings between them and depths of 4 μm (PE4), 8 μm (PE8) and 12 μm (PE12) respectively.

Figure 2.15 shows an improvement in both the polarisation curves, and the maximum achievable power density. It can be seen that although a larger depth of the microholes would result in a larger specific surface area, it was the MEA consisting of 8 μm deep microholes that was superior in performance, with an improvement in maximum power density of 21.9% compared to the conventional MEA. It is believed
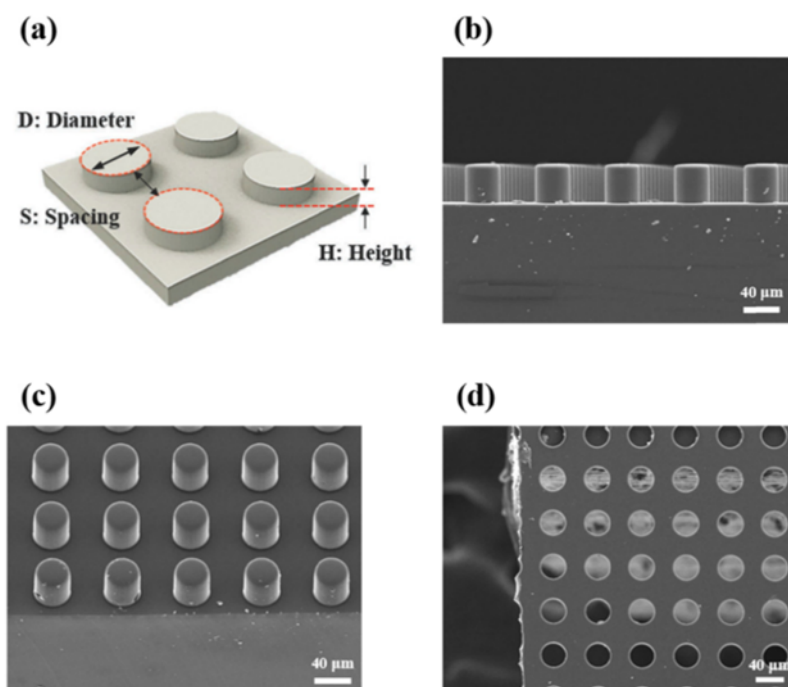
Figure 2.14: (a) Schematic illustration for structural information of the micropillar array. (b,c) SEM images of the PDMS mould with micropillars with a diameter of 40 μm, spacing of 40 μm, and height of 40 μm with cross-section (b) and titled view (c). (d) SEM images of the free-standing polymeric stencil with microhole patterns in diameter of 40 μm, spacing of 40 μm, and thickness of 40 μm [15].

that the reduced performance in the PE12 MEA compared to the PE8 MEA could be due to the increased depth of the microholes resulting in extremely thinned etched regions which adversely affect charge transfer kinetics on the cathode side, resulting in increased hydrogen crossover [125].
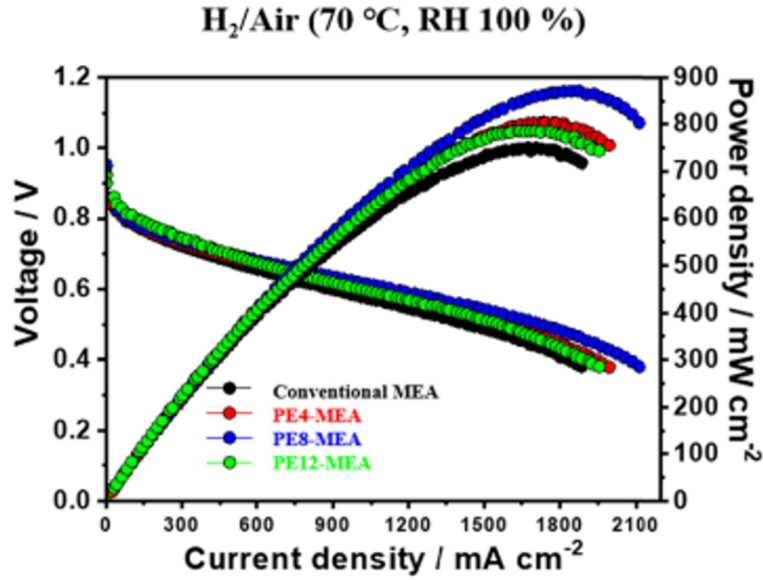
Figure 2.15: Graph showing the polarisation curves and power density curves, of the PEMFCs, at 70°C with 100% RH, consisting of membranes fabricated with an array of microholes [15].

2.2.5   Electron Beam Lithography

Whereas photolithography is very similar to other etching techniques, electron beam lithography uses a focused beam of electrons for exposure. The beam is accurately directed to positions on the wafer to form a pattern. Depending on whether a positive or negative electron beam resist is used will determine whether a chemical used will either etch away the resist targeted or not targeted by the electron beam, respectively (Figure 2.16) [126].

The electron beam is used to expose the pattern dot by dot or in lines. This is also very time consuming. However, there is no need for the expensive mask as that in the photolithography or chemical etching, which means the method offers a lot more flexibility. Also, due to the size of the electron beam, precise patterns with detailed feature sizes of below 10 μm can be achieved [127]. It should be noted that the

expenses saved on the lack of a mask are noticeable in comparison to the expensive
and complex electron-compatible optics required to focus the electron beam into a
spot of a few nanometres [128].
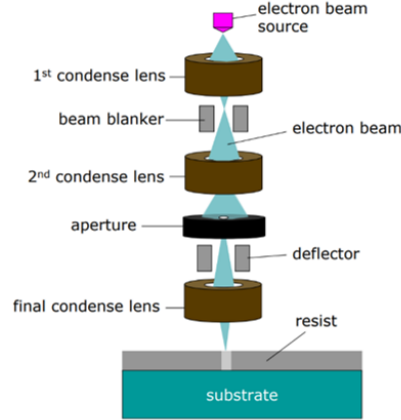
Figure 2.16: Schematic of the patterned membrane fabrication process via Electron
Beam Lithography [16].

Common applications of electron beam lithography include cryo-electric devices, opto-
electronic devices and quantum structures [129].

Omosebi et. al [104], in 2012, used electron beam lithography to pattern Nafion 212
with pores with diameter and depth of 2 μm and 5 μm respectively. When comparing
to pristine Nafion 117, they showed a possible improvement in the maximum current
density of 18.4%, going from 240 mA/cm^2 to 284.2 mA/cm^2, and an improvement of
25.9% in the maximum power density, going from 50.1 mW/cm^2 to 63.1 mW/cm^2.
However, it should be noted that this comparing patterned Nafion 212 with pristine
Nafion 117 is not scientifically appropriate, and although it is the same material used
for a PEMFC. The Nafion 212 has a thickness of 50 μm, which is much thinner than
the 183 μm of Nafion 117 membrane, and a higher power density is expected in the
single cell test due to the much enhanced ionic conductivity.
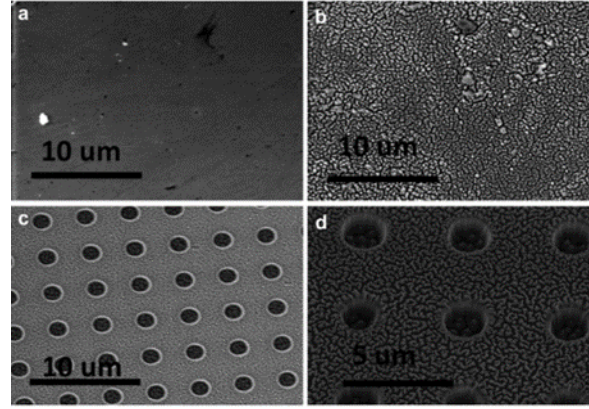
Figure 2.17: SEM images of (a) pristine, (b) Blanket-etched, and (c)(d) patterned Nafion 212, with pores with diameter and depth of 2 μm and 5 μm, respectively [17].
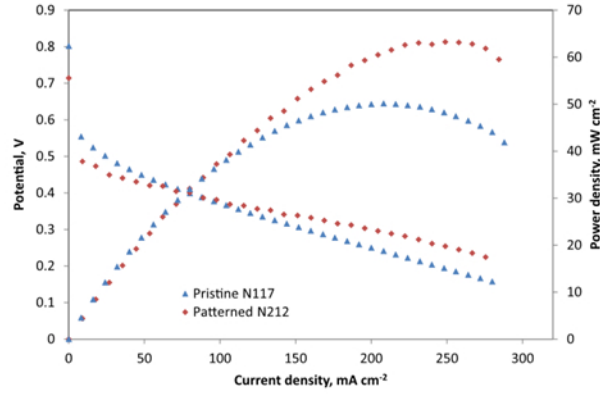
Figure 2.18: Graph showing the improvement of current density and power density as a result of patterning [17].

Omosebi et. al [130], in 2013, also fabricated in-membrane micro-fuel cells by using electron beam lithography for pattern creation, followed by dry etching for pattern transfer and aspect ratio manipulation. Figure 2.19 shows a schematic of the procedure for how the in-membrane micro fuel cells were fabricated.
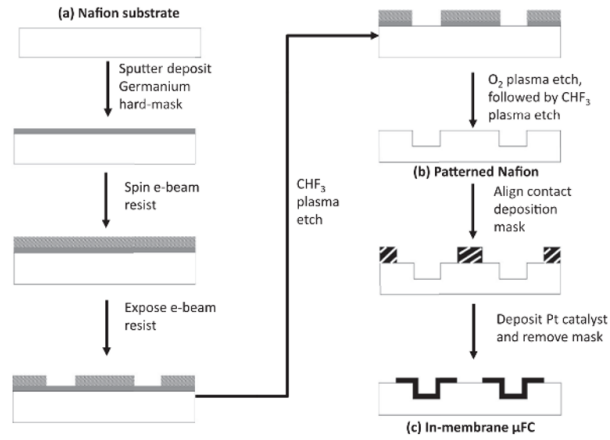
Figure 2.19: Flow diagram for the fabrication of the in-membrane μFC [16].

The resultant patterned in-membrane micro-fuel cell were characterized by featuring two channels 100 μm in width, 10 mm long, and a depth of 10 μm, which is equivalent to 20% of the total thickness of the Nafion 212 membrane used. In their analysis, they observed the patterned micro-fuel cell compared to a conventional fuel cell in both dry and humid conditions. Figure 2.20 shows the polarisation curves and power density curves of the four samples.
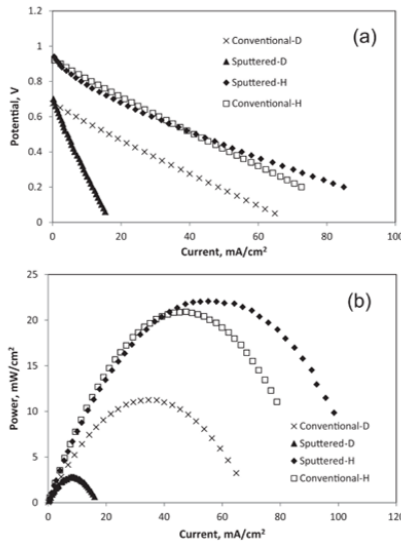
Figure 2.20: Polarisation curve (a)and power density curves (b) for the conventional and Patterned micro-fuel cells under dry and humid conditions.

The polarisation curve plot shows a reduced open current voltage (OCV) of about 0.65 V for both the sputtered and conventional cells under dry conditions, compared to the sample readings in humidified conditions of about 0.92 V. This indicates the significant gas crossover during testing under dry conditions by gas permeation at the sealing interfaces [131]. A reduction in the volume of gas available for crossover when in humidified conditions because H_2O condensation, and swelling of the membrane to better contact the sealing plate can significantly mitigate gas crossover. The ohmic resistance of the conventional fuel cells in both conditions, and the patterned fuel cell under humidified conditions appear to be very similar. However, the ohmic resistance of the patterned fuel cell under dry conditions is significantly larger. This is believed to be due to the dry patterned fuel cell being exposed to further dehumidification while sitting in a vacuum for several hours during the sputtering process, which would result in an increased resistance.

The power curves show that the patterned fuel cell, under humidified conditions, exhibited the best power performance, whilst the patterned fuel cell, under dry conditions, was the worst performing fuel cell in terms of power. This was similarly seen when comparing maximum power densities. It can be seen that there is a correlating trend between ohmic resistance, which was found via EIS measurements, and maximum power density, as can be seen in Table 2.2.

Table 2.2: Table comparing the Fuel Cell performance depending on their morphology and operating conditions.

Sample	Ohmic Resistance (Ωcm^{-2})	Maximum Power Density ($mWcm^{-2}$)
Conventional - Dry	7.5	11.2
Conventional - Humid	5.9	20.8
Patterned - Dry	25.0	3.0
Patterned - Humid	2.6	22.1

2.2.6   Technique Comparison

It could be seen that quite a few methods have been reported for the fabrication of patterned membranes. While most of them improved power performance, some also showed some disadvantages. Table 2.3 summarises the techniques reported for fabricating patterned membranes, with a collection of their advantages and disadvantages.

Table 2.3: Table showing the Advantages and Disadvantages of different Membrane Patterning Fabrication Techniques.

Fabrication Technique	Advantages	Disadvantages
Silicone Moulding	Simple process available for mass production Can fabricate structures of varying complexity	Silicone mould is relatively expensive Defects occur in silicone mould after repeated use Low accuracy
Thermal Lithography	Includes Atom Probe Microscopy of the surface Very high resolution	Slow process – restricted by the mechanical scanning speed Expensive to regularly change the cantilever
Hot Embossing	Different fabrication methods can be used to make the master mould, depending on desired characteristics Master mould can be used multiple times	Time and cost of fabricating the master mould
Plasma (Dry) Etching	No horizontal etching as would be present in wet etching High accuracy	Very Slow Not suitable for mass production
Electron Beam Lithography	Expensive masks are not required, allowing more flexibility Precision below 10 μm can be achieved	Very Slow Not suitable for mass production

It can be seen that both silicone moulding and hot embossing are suitable for mass production although the pattern that can be made has a relatively lower accuracy, and a master mould is required. As a comparison, both the lithography methods and plasma etching can provide a very high accuracy, however, their speed is slow and might be mainly used for research rather than a large scale production.

Table 2.4 provides a thorough analysis of the different fabrication techniques with the power performance recorded for the as-prepared patterned membrane. Along with the differing pattern morphologies from the various studies, we can use the collected data to create a better understanding of which geometries are most promising for improving both maximum power density and current density. Comparing different fabrication techniques, and assessing which method is best is initially very challenging, given not only can the fabrication technique be a key variable, but more importantly, the differing pattern designs will have a big influence on the output results. However, we are able to compare Thermal Lithography, Hot Embossing, Plasma Etching and Electron Beam Lithography more reliably, because each of these fabrication techniques include studies featuring a linear-pattern design. All of the results for this morphology were positive compared to their respective planar morphologies, unless the dimensions of the linear channels were too small, as was also seen by Bae et al [10], where the dimensions of the linear channels were smaller than the size of the catalyst agglomerates, resulting in a poor interface between the catalyst and the membrane. However, as long as the dimensions of the patterned morphology were greater than the size of the catalyst particles, it can be seen that there is a positive trend towards improved performance when the patterning dimensions are decreased. This is primarily due to an increased active surface area for the ORR to occur on.

Table 2.4: Table showing a collection of experiment results from the literature showing how performance improvement varied depending on fabrication technique and morphology, compared to their respectively planar morphologies.

		Results				
		Pattern Design			Performance	
Fabrication Technique	Morphology	Geometries	Schematic	Surface Area Increase	Maximum Power Density Increase	Current Density Increase
Silicone Moulding [7]	Indented Cubes (Width x Depth x Height)	3 x 3 x 1.4 μm 3 x 3 x 1.9 μm 3 x 3 x 3.7 μm		46% 66% 120%	73.2% 77.2% 73.2%	28.1% 68.8% 100.0%
Thermal Lithography [114][10]	Pillar Structure (Width x Pitch x Height)	7.0 x 14.2 x 3.4 μm 7.0 x 14.2 x 6.7 μm 7.0 x 14.2 x 10 μm				6-11%
	Linear Pattern (Width x Spacing x Height)	110 x 90 x 70 nm 5 x 2 x 1 μm 5 x 10 x 1 μm		70% 29% 13%	-10.7% 25.0% 8.9%	-7.8% 29.0% 11.7%
Hot Embossing [12]	Linear Pattern (Width x Spacing x Height)	19 x 25 x 20 μm		45%	12.2%	33.3%
Plasma (Dry) Etching [14] [15]	Linear Pattern (Width x Spacing x Height)	40 x 55 x 25 μm - RH 66% 40 x 55 x 25 μm - RH 100%			-26.3% 52.7%	11.3% 79.5%
	Mircoholes Array (Diameter x Spacing x Depth)	40 x 40 x 4 μm 40 x 40 x 8 μm 40 x 40 x 12 μm			6.6% 16.2% 4.0%	8.0% 15.0% 5.5%
Electron Beam Lithography [104][130]	Pores (Diameter x Depth)	2 x 5 μm		50%	25.9%	18.4%
	Linear Pattern (Width x Spacing x Depth)	100 x 400 x 10 μm			6.3%	15.4%

Deshmukh et al [14] also demonstrated a reduction in performance for their patterned morphology at a relative humidity of 66%. This is more of a reflection on the performance of the planar geometry sample, which was significantly poorer at the 100% relative humidity, suggesting that any potential negative effects of the geometry were heavily outweighed by the involved water management due to the linear-patterned structure providing a preferential route for water to leave from the surface of the ORR interface. This could be a great advantage for using the patterned membrane.

Comparatively between the four mentioned fabrication techniques for the linear-patterned morphologies, the aforementioned results from the study of Deshmukh et al showed the best maximum power density of a 52.7% improvement, but this was the only study to mention it was done at 100% relative humidity. Besides this one potential outlier, Bae et al [10], had the most promising results, with the samples fabricated by thermal lithography resulting in an improvement in maximum power

density and current density of 25.0% and 29.9% respectively.

Other than the linear-patterned morphology studies, the Direct Spray Deposition fabrication technique stands out due to the results from the study by S. Cuynet et al [105], who found that generating a morphology consisting of an array of knolls resulting in very significant improvements in maximum power density and current density. Ignoring the two results of an improvement in current density of 77.8% and 407.4%, most of the samples fabricated with an array of knolls yielded maximum power density and current density figures of between 19-26% and 30-40%, which are much larger figures than the other studies produced.

2.3 Interface for Water Management

Water management is a key issue in the design of a fuel cell during operation. Water, as the only by-product of a hydrogen fuel cell, if it cannot leave the reaction site after being formed, it will cause flooding and cover the reaction sites on the catalyst surface and also block the transport path of the reactant, e.g., oxygen or air gas in PEMFCs, finally resulting in reduced fuel cell performance. For fuel cells operating at very high temperature, such as solid oxide fuel cells (SOFCs) between 700-1000°C, or high temperature PEMFCs between 160-180°C, the high temperatures cause the water to evaporate and there's no flooding concern. However, for fuel cells that operate at a temperature below 100°C, the boiling point of water [132], such as PEMFCs, the water management is thus a big issue. The current research suggests increasing the operating temperature to above 100°C to help solve this water management issue. However, for the current perfluorosulfonic acid (PFSA) membrane (e.g., Nafion) commonly used in PEMFCs, a lower option temperature below 80°C is essential to

maintain a high water content to ensure a high ionic conductivity [133]. The research on patterned membrane demonstrated some improvements in the water management in PEMFCs, so this issue is briefly reviewed here to further the understanding.

2.3.1   Optimal Operation Conditions

Operation conditions such as inlet humidity of the feed stream, operating current density, cell temperature, air and fuel stoichiometries, and back pressure can all be manipulated in a way to attempt to improve water management. If the humidity level of the inlet gas at the anode increases in the PEMFC, this would lead to the current distribution heterogeneities increase due to the decrease of liquid water transferred from the cathode to the anode via back-diffusion [134]. Water can also be flushed out of the cell system through evaporation and advection if the reactant flow rate of cathode reactants is increased, improving the performance of the cell due to the high stoichiometry [135][136][137][138][139]. A large pressure gradient can even be applied between the cathode and the anode, forcing liquid water through the membrane from the cathode to the anode, known as 'anode water removal' [140]. However, this strategy comes with the downside of causing parasitic losses linked to pressure, volume flow rate and pressure drops, as well as the risk of potentially rupturing the membrane design [141].

2.3.2   Cell System Design

Internal humidification, or 'self-humidification' is based on the idea that the membrane retains absorbed water under operating conditions [142]. However, it is difficult to control the humidity, and a large external water humidification system is required, as well as the potential for steady-state multiplicity to occur [143]. With an external

humidification method, the desired temperature and relative humidity of the gas can be controlled independently. However, using an external humidifier requires additional apparatus [144], Nguyen et al [145]. found an extremely effective method of water management was injecting liquid water directly into the fuel cell, in conjunction with the interdigitated flow fields as a humidification technique. However, the possibility of flooding the fuel cell is a risk of direct water injection.

Based on this finding, Kim et al [146]. developed a sub-scale gas humidifier consisting of an injector, an enthalpy mixer and a water-retrieval unit, where rather than having the direct injection of water into the fuel cell, water injected into the enthalpy mixer is chosen, preventing water flooding or clogging in the gas channels of the fuel cell.

2.3.3 Flow Field Design

The most successful strategy for dealing with water flooding issues is having an appropriate flow channel design that transports water from the GDL via these flow channels [147]. There are three mainly adopted typical flow fields. The conventional flow field, the serpentine flow field and the interdigitated flow field.

In the conventional flow field, the dominant mechanism for the transport of reactants and products is diffusion, which limits the rate of transport of reactants, showing a high trend for the accumulation of liquid water and water flooding [148][149].

Serpentine flow channels [150][151] are the most widely used flow field design, because of their capability to bring reactant gas to the catalyst layer for the electrochemical

reaction, whilst removing the water by-product from the reaction sites and electrodes, by creating a large pressure gradient across the porous electrode as a result of the pressure drop and concentration change along the channel.

The interdigitated flow field design forces the gas to flow through the porous GDL, transporting the reactants by a forced convection mechanism. The force resulted from the gas flow prevents flooding by flushing water out of the electrode, improving the cell performance [145]. However, the higher pressure needed to force the gas through the GDL can result in additional power loss and drying of the membrane at low current densities.
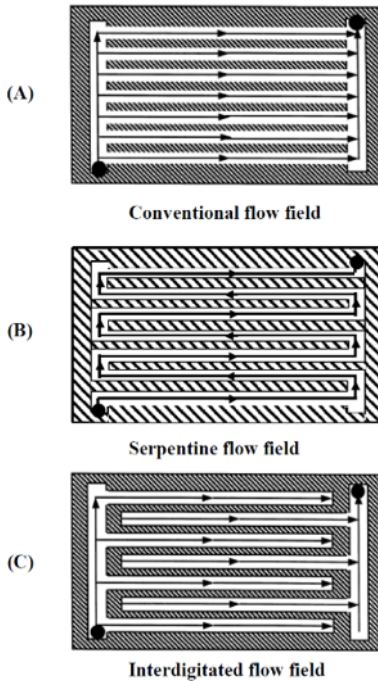
Figure 2.21: Three typical flow field designs (A) conventional flow field, (B) serpentine flow field and (C) interdigitated flow field [18].

2.3.4 Hydrophobic and Hydrophilic Coating

In 2011, Tatsumi Kitahara et. al. [152] found that water management could be improved by coating the GDLs of the cathode with a double microporous layer consisting of a hydrophilic layer and a hydrophobic layer. The hydrophilic layer was effective for conserving humidity at the catalyst layer whilst the hydrophobic layer between the hydrophilic layer and the substrate prevented the removal of water in the hydrophilic layer via dry air in the substrate. Reducing the maximum pore diameter of the hydrophobic layer to 20 μm proved to improve the fuel cell performance, but if the pore diameter became too small, the concentration overpotential increases, lowering the overall performance.
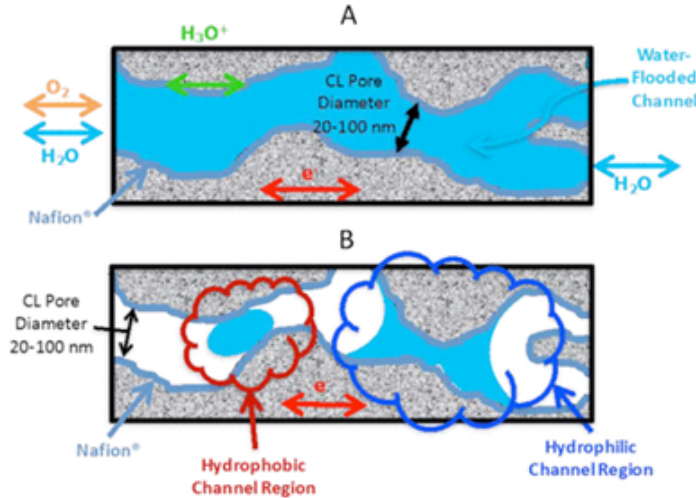
Figure 2.22: Cross-sectional side view of (A) water-flooded cathode layer channel and (B) engineered cathode layer polymer surface.

In 2016, Regis P. Dowd Jr. et. al. [153] showed that specific heat treatment conditions could be used to tailor the wettability of the cathode catalyst layer as displayed in Figure 2.22. They were able to create a hydrophobic polymer-gas interface inside the gas pores of the cathode catalyst layer which gave preliminary results of 33% increase in peak power.

2.3.5   Interface Patterning

Some studies, which have been previously mentioned, have shown that by patterning the interface with certain morphologies, it is possible to influence the flow of water away from the interface, such as the research carried out by Deshmukh et. al [14]. They demonstrated this observation when they patterned the interface with a linear-pattern. There was an observed improvement in fuel cell performance, believed to be due to the water by-product preferentially flowing away from the active reaction site, because of these linear channels.

2.4   Summary and Perspectives

If we are going to find a way of reducing the impact of the climate change by replacing internal combustion engines with PEMFCs, improvements have to be made into increasing the cost effectiveness of the current technology. Although there are several avenues that can be taken in trying to achieve this objective, one key method would be to increase the rate of the ORR, the rate limiting step of the reactions that occur in a PEMFC. It has been shown that changing the morphology, by patterning the interface between the membrane and the catalyst layer of the cathode, the active surface area of the interface can be increased, resulting in improved fuel cell performance. Additionally, it has been shown that some geometries offer benefits in water management, which has been a key factor in the poor ORR performance in the PEMFC with planar interfaces.

Chapter 3

Simulations of PEMFCs

As discussed in Chapter 2, research has gone a long way in terms of looking for a way to improve the overall performance of PEMFCs, by optimizing the structural and operation conditions to maximize the rate of the Oxygen Reduction Reaction (ORR) as the rate limiting step. However, building new experimental rigs for each individually patterned membrane requires a large amount of time and money. Computational Fluid Dynamics (CFD) could be used to speed up the process to find the best variables for optimal fuel cell performance. However, before doing so, it is important to understand how CFD works, and how exactly it can be used to simulate the reactions taking place within a PEMFC.

CFD is a branch of fluid dynamics that allows us to simulate real-life fluid flow, heat transfer and other operations such as chemical reactions, by solving a set of governing equations [154].

CFD offers the benefit of being a much more cost-effective means as opposed to solely relying on physical experimentation, being both faster and cheaper to simulate

multiple structures without building each individually required experimental rig.

The first known record of using computers to solve linearized potential equations, using conformal transformations of flow about a cylinder to the flow about an airfoil, dates back to the 1930s [155].

This technology was later built upon by Lewis Fry Richardson, who tried to predict the weather with calculations using finite differences and divided the physical space in cells, in what can be seen as one of the earliest type of calculations resembling modern CFD [156].

After decades of progressive improvements in the functionality and capabilities of various modelling software, CFD has become a well-recognized tool in a wide range of industries, such as [157]:

- Biomedical Engineering

- Mechanical Engineering

- Missile Engineering

- Architecture

- Food Industry

- Automobile Industry

There are many different types of modelling software for CFD simulation, with some being more suitable than others depending on whether your model needs to be physical, mathematical or conceptual. Many physical models look like the thing they

model. For example, a plastic skeleton of a human body. A limitation of this type of model is that it may look like the real thing, which can be useful for understanding how the body works, but since it is not alive it does not act exactly like a human body. Mathematical models can be made up of numbers, equations or other forms of data. A simple example of a mathematical model could be a Punnett Square used to predict certain traits of offspring of certain parents [158]. The third type of model, conceptual model, represent systems of ideas or compare unfamiliar things with familiar things. An example of a conceptual model would be scientists classifying the behaviour of animals to predict how they would respond to a certain action based on traits which have already been observed.

Modelling of a fuel cell would be characterised as mathematical. The three most suitable mathematical modelling software for modelling a fuel cell are COMSOL Multiphysics, Ansys-Fluent, Antodesk CFD and Sim Scale. A brief comparison of them are listed below in Table 3.1.

Table 3.1: Comparison Table of the Three Main Modelling Software for Fuel Cells [30][31][32][33][34][35].

Modelling Software	Advantages	Disadvantages
COMSOL-Multiphysics	- Enables multi-physics problems - User-friendly interface for visually building the model - Access to LiveLink to connect with other software tools	Does not provide optimized numerical techniques for fluid flow simulation
Ansys-Fluent	- Simple interface - Better processing - More stable	- When simulating porous media, the non-equilibrium thermal model is not supported with radiation and/or multiphase models - No Boundary zone extrusion possible from faces that have hanging nodes
Autodesk CFD	- Simple interface - Can model individual parts and combine them to complete assemblies - Multiple additional features	- Uses a large amount of CPU memory - Limited meshing capability so not recommended for complex geometries
SimScale	- Easy to copy design scenarios - Geometric non-linear analysis	- Setup information can sometimes be dropped from the models - Cylindrical based boundary conditions

Scientists have been modelling PEMFCs since the middle of the 19th century. However, it took a considerably long time before our understanding of the science, and the improved modelling technology allowed us to reach the current models that are used today.

3.1 Development of the Interfacial Double Layer

Here, we show how modelling of the electrode-electrolyte interface has changed over the past 150 years.

3.1.1 Helmholtz Model
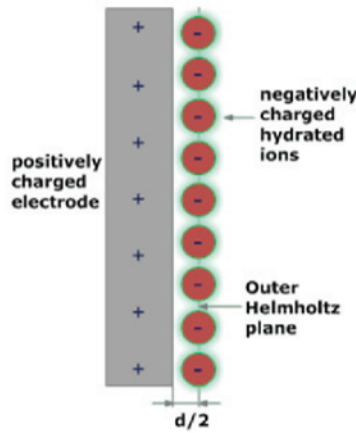
Figure 3.1: Helmholtz Model of the Double Layer.

The first developed model of the interface between the cathode and the electrolyte in PEMFCs was built by the German physicist, Hermann von Helmholtz, in 1879 [159]. It was a very simple double layer model which considered the concept of the charge separation at the interface between a metallic electrode and an electrolyte solution as shown in Figure 3.1 [160].

Due to an excess or deficiency of electrons at the electrode surface, the electrode holds either a negative or positive charge respectively. This charge is balanced by a reorganisation of charged ions in the solution of the electrolyte, with oppositely charged ions being attracted to the electrode surface. This creates two layers of opposite charge separated by some distance $x = \frac{d}{2}$ limited to the radius $\left(\frac{d}{2}\right)$ of the

attracted ions and a single layer of solvation around each ion. The line that passes through the ions attracted the electrode is called the 'Outer Helmholtz Plane' and the region within it is the electrical double layer.

The Poisson's equation in 1D is used to relate the potential with the charge distribution,

$$\frac{\partial^2 \varphi}{\partial x^2} = -\frac{\rho(x)}{\varepsilon_r \varepsilon_0} \tag{3.1}$$

Where φ is the electrical potential, ρ is the charge density, x is the distance from the electrode, ε_0 is the permittivity of a vacuum and ε_r is the relative permittivity of the medium.

The model used the following boundary conditions:

$$\text{At x=0, } \phi = \phi_0 \text{ and } \lim_{x \to \infty} (x) = 0 \tag{3.2}$$

Helmholtz simplified the model by assuming the ions could be treated as point charges, meaning the right-hand term of the Poisson's equation is equal to 0.

$$\frac{\partial^2 \varphi}{\partial x^2} = 0 \tag{3.3}$$

This means the model defines the system in a similar behaviour to a parallel plate capacitor, meaning the electric double layer is capable of storing electrical charge and having a capacitance per unit area of,

$$C_H = \frac{\varepsilon_0 \varepsilon_r}{l} \tag{3.4}$$

Where l is the thickness of the double layer [161].
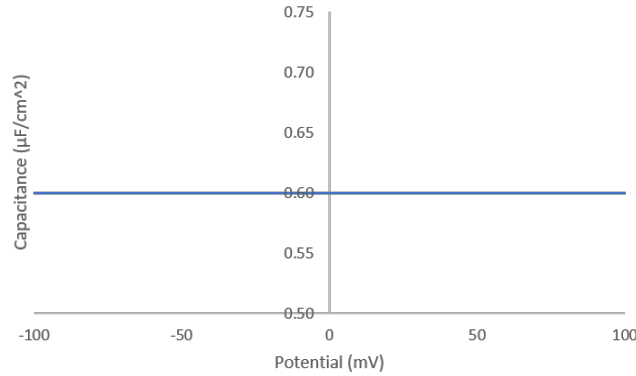
Figure 3.2: Helmholtz Model Capacitance Curve of an Electrode-Electrolyte Interface.

Following the Helmholtz model, Figure 3.2 shows what would be the expected capacitance curve for a cathode-electrolyte interface. However, this does not fit to the real experiment results shown in Figure 3.3. This could be due to the limitations of the model. Namely, the model does not account for the dependence of the measured capacity on potential or electrolyte concentration. The model also does not consider interactions that occur away from the Outer Helmholtz Plane.
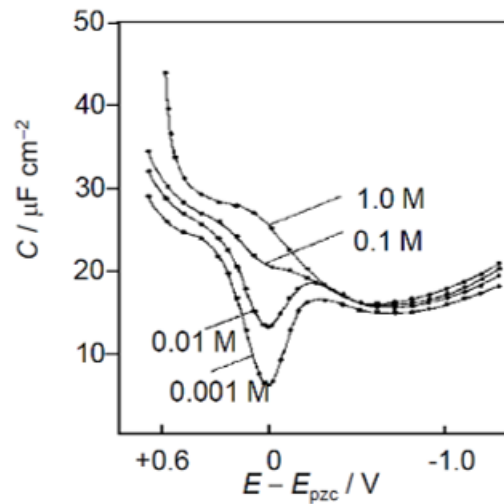
Figure 3.3: Experiment results of capacitance curve of an electrode-electrolyte interface [19].

3.1.2 Gouy-Chapman Model
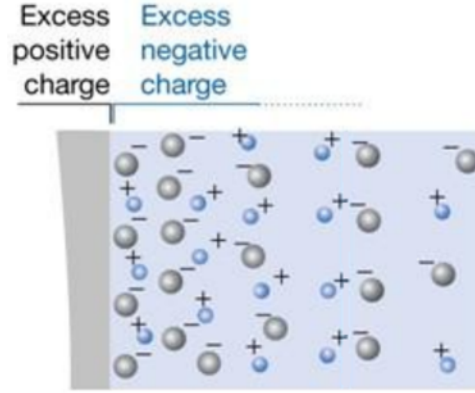
Figure 3.4: Gouy-Chapman model of the double layer [20].

In 1910 and 1913 respectively, Louis Georges Gouy and David Leonard Chapman tried to build their own model for the interface simulation (Figure 3.4). The charge on the electrode was still confined to the surface, but the charge in the solution was not exclusively situated at the Outer Helmholtz Plane. The ions in the solution were, however, still considered to be point charges [162]. The concentration of the charge of the counter ions to the electrode surface decreases from the surface into the bulk, following the Boltzmann distribution,

$$n = n_0 e^{-\frac{ze\varphi}{kT}} \tag{3.5}$$

Where n_0 is the bulk concentration, z is the charge on the ion, e is the charge on a proton, k is the Boltzmann constant and T is temperature in degrees Kelvin.

The distribution assumes that activity is equal to molar concentration. This is true for the bulk solution but is not accurate for the place near the electrode surface [163].

The thickness of the double layer can be computed by combining the Boltzmann distribution with the Poisson equation and integrating under appropriate limits, and then rearranging the solution. This gives,

$$\lambda_{double} = \left(\frac{\varepsilon_r kT}{4\pi e^2 \sum n_{i0} z_i^2} \right)^{\frac{1}{2}} \tag{3.6}$$

Which at room temperature can be simplified to,

$$\lambda_{double} = \frac{3.3 \cdot 10^6 \varepsilon_r}{z c^{\frac{1}{2}}} \tag{3.7}$$

For this equation, we see that the thickness of the double layer decreases with increasing valence and concentration.

The charge density of the diffuse double layer is used as,

$$\sigma_M = \varepsilon_r \varepsilon_0 \left(\frac{\delta \varphi}{\delta x} \right)_{x=0} \tag{3.8}$$

The differential capacitance can be obtained by differentiating the charge density,

$$C_{GC} = \frac{d\sigma_M}{d\varphi_0} = \left(\frac{2z^2 e^2 n_i^0 \varepsilon_r \varepsilon_0}{kT} \right)^{\frac{1}{2}} cosh\left(\frac{ze\varphi_0}{2kT} \right) \tag{3.9}$$

The capacitance curve at the electrode-electrolyte interface based on the Gouy-Chapman model is shown in Figure 3.5. This is closer to the real capacitance curve, showing a potential of minimum capacitance. However, the current curve is symmetrical so is still missing an important observation.
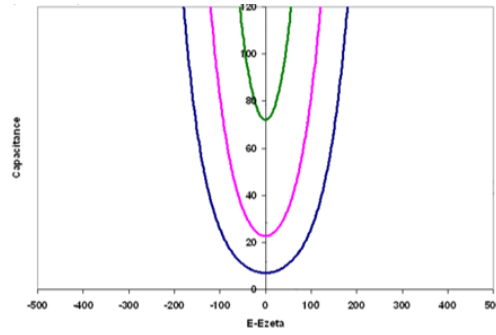
Figure 3.5: Gouy-Chapman Model Capacitance Curve of an Electrode-Electrolyte Interface [21].

3.1.3   Stern Model
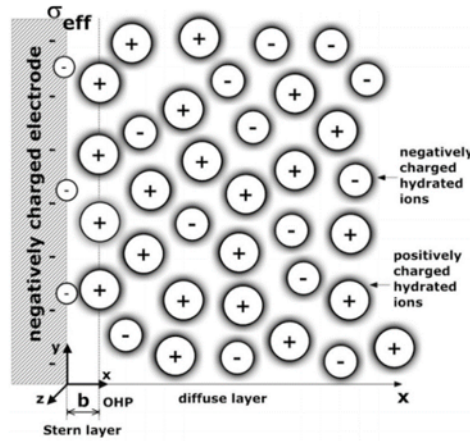
Figure 3.6: Stern Model of the Double Layer [22].

In 1924, Otto Stern improved the double layer theory by combining both the Helmholtz model and the Gouy-Chapman model together. However, Stern accounted for a flaw in the previous two models (Figure 3.6). Ions have a finite size, which had previously been ignored. This meant that the closest approach of the Outer Helmholtz Plane to the electrode varies with the radius of the ions. This region between the ions of the Outer Helmholtz plane and electrode is called the Stern Layer.

The total capacitance of the double layer is calculated as being equivalent to two capacitors, the Outer Helmholtz Plane and Diffuse Layer, in series [164]. Therefore,

$$\frac{1}{C_S} = \frac{1}{C_H} + \frac{1}{C_{GC}} \tag{3.10}$$

where C_S is the Stern capacitance of the whole model, C_H is the Helmholtz capacitance of the Outer Helmholtz Plane and C_{GC} is the Gouy-Chapman capacitance of the Diffuse Layer.
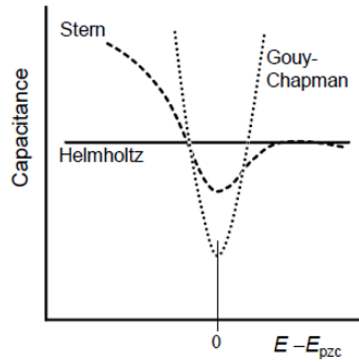
Figure 3.7: Stern Model Capacitance Curve of an Electrode-Electrolyte Interface by combining Helmholtz's and Gouy-Chapman's Capacitance Curves [23].

By following the equation for C_S, Stern was able to generate a capacitance curve similar to the actual data (Figure 3.7). Stern's modelled capacitance curve can be seen to the left as a combination of the two capacitance curves which Helmholtz and Gouy-Chapman modelled separately.

3.1.4 Grahame Model

In 1947, David Grahame modified Stern's model. In Stern's model, the closest that some ions can be to the charged electrode surface was along the Outer Helmholtz Plane. However, Grahame proposed that some ions or uncharged species could pen-

etrate this plane into the Stern layer [165]. This could occur if the ions lost their solvation shell upon approaching the electrode surface, allowing them to adsorb to the electrode surface. These adsorbed ions are classed as 'Specific adsorption' and would form another plane known as the Inner Helmholtz Plane [166].

3.1.5   Bockris/Devanathan/Müller

Up until now, there had been little consideration for how the solvent might impact the interface between the electrode and electrolyte. In 1963, John Bockris, Michael Angelo Vincent Devanathan and Klaus Müller proposed such a model. They suggested that molecules from the solvent such as water, attached to the electrode surface would have a fixed alignment with the electrode surface. The first layer of these solvent molecules would be strongly orientated with the electric field, which greatly influenced the permittivity of the solvent.

Figure 3.8 shows a schematic representation of the solvent molecules adjacent to the electrode surface, up until the Outer Helmholtz Plane. The first water layer has a relatively low dielectric constant (ϵ_L). The dielectric constant will be much higher in the second layer of water molecules(ϵ_H).

bulk water structure
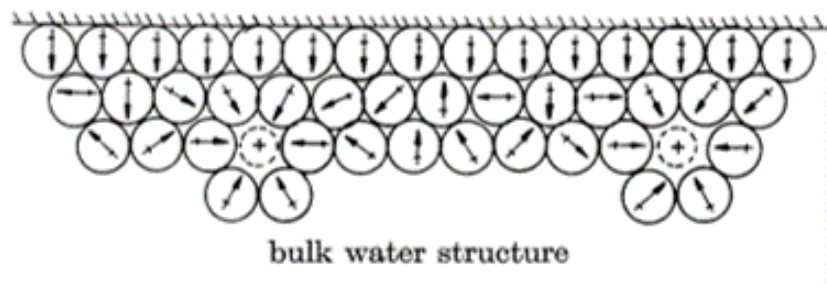
Figure 3.8: Model of the Interface to Explain Constancy of Cathodic Capacity [24].

As seen in Figure 3.8, the orientation of the water molecules' dipoles is strongly af-

fected by the presence of ions in the Outer Helmholtz Plane. This means the potential changes with the dielectric constant and the distance from the interface by,

$$4\pi q_M \sum \frac{x_i}{\epsilon_i} = \triangle\varphi \qquad (3.11)$$

where q_M is the charge per square centimetre of the electrode, ϵ_i is the dielectric constant, x is distance and ϕ is the potential.

Near the minimum capacity, K,

$$\frac{dC}{d\varphi} \to \varphi \qquad (3.12)$$

Therefore,

$$\frac{1}{K} = 4\pi \left[t \left(\frac{1}{\epsilon_L} - \frac{1}{\epsilon_H} \right) + \frac{\delta}{\epsilon_H} \right] \qquad (3.13)$$

where K is the minimum capacity and t is the diameter of the water molecule.

If $\epsilon_H \gg \epsilon_L$, then K will be independent of δ and r_{ion}.

So, as the dielectric constant of the water molecules decreases with distance from the interface, the change in electric potential increases in accordance with equation 3.9. The BDM model is now most commonly used.

3.2   Electron Transfer Kinetics

Whilst our understanding of the interface model has improved over time, so has our knowledge of the electron transfer kinetics, which are very important when attempting to understand how the ORR occurs at the interface.

3.2.1   Bulter-Volmer Approach

In 1930, John Alfred Valentine Butler, Max Volmer and Alexander Frumkin developed a theory for the kinetics of electron transfer at an electrode [167] by suggesting that the overall flux of a reaction was equal to the flux of the oxidation reaction minus the flux of the reduction reaction, i.e.

$$j_{tot} = j_{ox} - j_{red} \tag{3.14}$$

Given that,

$$I = nFAj \tag{3.15}$$

Where 'I' is current, 'n' is the number of electrons transferred, 'A' is the area of the electrode and 'j' is the flux of the reactant, and

$$j = k_n \left[X\right]_0^n \tag{3.16}$$

Where k_n is the nth order rate constant and $-[X]_0$ is the surface concentration. Hence, we see that,

$$I = nFA(j_{ox} - j_{red}) \tag{3.17}$$

Independently, Butler and Volmer found the reductive and oxidative rate, k_{red} and k_{ox}, of electron transfer were equal to,

$$k_{red} = k_0 e^{\frac{\beta F \eta}{RT}} \tag{3.18}$$

and,

$$k_{ox} = k_0 e^{\frac{-\alpha F \eta}{RT}} \tag{3.19}$$

Where η is the overpotential defined by $\eta = E - E_f^0$, and β and α are the transfer coefficients for the reduction and oxidation reactions respectively.

By combining all the terms together this gives us,

$$I = -nFAk_0\Big([A]_0\, e^{\frac{\beta F\eta}{RT}} - [B]_0\, e^{\frac{-\alpha F\eta}{RT}}\Big) \tag{3.20}$$

This is famous the Butler-Volmer equation [168].

By taking the sum of the transfer coefficients to be equal to 1, as would be the case for most single electron transfer, they could set the overpotential to either very large and positive, or very small and negative. By doing this and rearranging the equation, they were able to generate graphs of ln(I) against η called 'Tafel plots'. Tafel plots can be used to calculate the values of β and α [169]. In 1886, Walter Nernst showed by setting the current to 0A, which suggests the reduction reaction rate is equal to the oxidation reaction rate, the equation can be rearranged to give the Nernst equation [78],

$$E = E^0 - \frac{RT}{nF}ln\frac{[red]}{[ox]} \tag{3.21}$$

Where E is the potential, E_0 is the standard electrode potential, R is the gas constant, T is temperature in degrees Kelvin, n is the number of electrons transferred, F is Faraday's constant and [red] and [ox] are the concentration of the reductants and oxidants respectively.

3.3   Simulations of PEMFCS

Since this research on assessing which pattern morphologies will generate the most optimal performance is solely based on theoretical models of PEMFCs, it is worth having an understanding on how simulations of PEMFCs have previously been conducted, as a way of giving an insight into what is important to include in the model moving forward.

There are three different categories in which a fuel cell model can be described.

3.3.1   Analytical Models

An analytical model, such as Standaert et al [170][25], use simplified assumptions to develop an approximate voltage versus current density relationship, whilst predicting water management requirements, for both isothermal and non-isothermal cells (Figure 3.9). They are good for providing quick calculations for simple systems. However, the disadvantage of the analytical models is that they can only provide an approximation, not giving an accurate picture of transport processes occurring within the cell, and are limited to predicting voltage losses and water management requirements for simple designs.

3.3.2   Semi-Empirical Models

Semi-empirical models use a combination of empirically determined relationships and directed differential and algebraic equations. The main advantage of semi-empirical models is the reduction in computation time, allowing for calculations for large molecules to be executed. However, the results can be erratic and fewer properties can be reliably predicted [171].
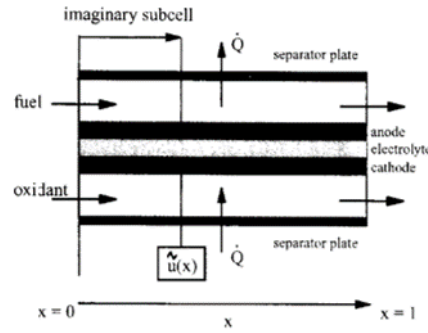
Figure 3.9: Schematic showing the Longitudinal section of the non-isothermal fuel cell modelled by Standaert et al. where x is the distance along the components perpendicular to the flow of ions, Q is heat transfer and $\tilde{u}$ is the local fuel utilisation [25].

Springer et al [172], made a semi-empirical model for a fuel cell with partially hydrated membrane, where empirically determined relationships were developed to find a correlation between the membrane conductivity and electrode porosity with the water content in the membrane (Figure 3.10). Many subsequent models have used these correlations to determine the conductivity of Nafion^{TM} membranes.
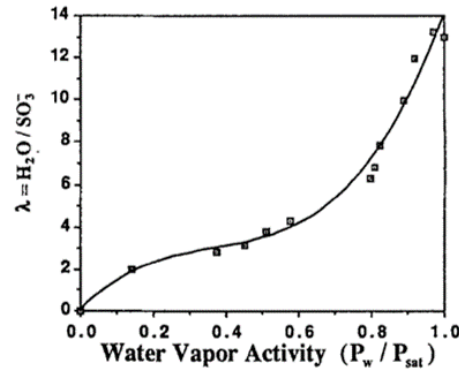
Fig. 2. Measured membrane water content vs. water activity for Nafion 117 at 30°C and according to Eq. [16].

Figure 3.10: Plot showing the correlation between the water vapour and water content in the membrane, λ, in accordance with Equation 3.22 [26]

$$\lambda_{(30C)} = 0.043 + 17.81a - 39.85a^2 + 36.0a^3 \text{ for } 0 < a \leqq 1 \tag{3.22}$$

Amphlett et al [173], estimated the potential losses, and fit coefficients in a formula for predicting the cell voltage, by using the semi-empirical relationships. The model accounted for activation loss and ohmic resistance overpotentials, whilst partial pressures and dissolved concentrations of hydrogen and oxygen were determined as a function of temperature, current density and gas channel mole fractions. Pisani et al [174], used a similar approach to study activation losses, ohmic resistance losses and transport limitations at the ORR interface.

3.3.3   Mechanistic Models

Most PEMFC models found in the literature use mechanistic modelling, which uses differential and algebraic equations derived from physics and electrochemistry governing the phenomena internal to the fuel cell, which are solved using computational methods. There are two sub-categories of mechanistic models: Multi-domain, and single-domain models.

Multi-domain Approach

As the name suggests, a multi-domain model has separate sections to the model, namely the anode and cathode gas diffusion regions, anode and cathode gas flow channels, membrane and catalyst layer. Each of these regions of the fuel cell has its own set of equations, which have to be solved separately and simultaneously.

One of the first mechanistic models for a PEMFC was the work done in the early 1990s, by Bernardi and Verbrugge [175][176], which involved modelling a one-dimensional (1D), steady state, isothermal model of a PEMFC that was fully hydrated at all times, which required calculations for the water input and removal to maintain a fully hy-

drated membrane. Maxwell-Stefan equations (Equation 3.23) were used to describe gas phase diffusion in the electrode regions, whilst the Nernst-Planck equation was used to describe dissolved species fluxes in the membrane and catalyst layers. Electrode rate kinetics and liquid water transport were described by the Butler-Volmer equation and Schlogl's equation (equation 3.24) respectively.

$$
\frac{\nabla \mu_i}{RT} = \nabla \ln a_i = \sum_{j=1; j \neq i}^{n} \frac{\chi_j}{D_{ij}} (\vec{v_j} - \vec{v_i}) = \sum_{j=1; j \neq i} n \frac{c_j}{c D_{ij}} \left(\frac{\vec{J_j}}{c_j} - \frac{\vec{J_i}}{c_i} \right) \tag{3.23}
$$

where ν is chemical potential, R is the gas constant, T is temperature in °K, a is activity, i and j are indexes for components i and j, n is the number of components, D_{ij} is the Maxwell-Stefan diffusion coefficient, $\vec{v_i}$ is the diffusion velocity of component i, c_i is the molar concentration of component i, c is the total molar concentration, and $\vec{J_i}$ is the flux of component i.

$$
v = \frac{k_\Phi}{\mu} z_f c_f F \nabla \Phi - \frac{k_P}{\mu} \nabla p \tag{3.24}
$$

where v is the pore-water velocity in the membrane, K_Φ is the electrokinetic permeability, z_f is the charge number of species f, c_f is the concentration of species f, F is Faraday's constant, Φ is potential, k_P is the membrane hydraulic permeability, μ is the pore-fluid viscosity and p is pressure.

Whilst the model was primarily used to predict the polarisation effects and water management requirements, it also predicted the dissolved hydrogen and oxygen concentrations within the catalyst layers, finding that at sufficiently high current densities, most of the electrochemical reactions occurred on the outer surface of the catalyst layer. Although this was a very basic model, it proved to be the foundation

for PEMFC modelling.

Single-domain Approach

Whereas Bernardi and Verbrugge developed a one-dimensional model, Gurau et al [177], developed a two-dimension (2D) model which could determine species concentrations within a fuel cell and the effect gas diffuser porosity, air flow rates in the gas channel, and temperature had on fuel cell performance. Although the model was based on the multi-domain approach, with three domains considered: the gas diffusers/flow channels, the catalyst layers and the membrane, by writing the governing equations for each region in a similar form, the gas diffusion and flow channels were combined into one domain. The only difference is that the materials properties and source terms are different for the two regions. This is what is defined as the single-domain approach.

Rather than combining multiple regions into one domain, the single-domain approach combines all regions of interest into a single domain. The entire fuel cell is governed by conservation equations. In each region, source or sink terms account for any differences between regions. All the conservation equations are normally written as a generic convection-diffusion equation, and all terms which do not fit that format are placed into the source or sink term. This allows computational fluid dynamics (CFD) methods to be used to find solutions.

Although CFD had been used in the modelling of other systems, it was not until Wang et al [178], in 1998 and Zhou et al [179], in 2001 that CFD was applied to fuel cells. In the unified approach, the governing differential equations can be arranged into a standard form, which can be approximated by using the principles of

CFD [180].

$$\frac{\partial \Phi}{\partial t} = \nabla(v\Phi) + \nabla(\Gamma\nabla\Phi) + S \tag{3.25}$$

where the terms in brackets are general variables, such as potential, temperature, pressure, velocity, concentration or phase fraction. The respective terms represent transient, convection, diffusion and the source.

3.4 Challenge with Current Research

As shown above, extensive research on the patterning of PEMFCs, with positive observed results in both current density and maximum power density, of as high as 77.1% and 41.1% improvements compared to their planar counterparts respectively. There is some scepticism to the validity of some of these results. Still, there is a strong correlation between patterning the morphology to generate a larger active surface area and an increased fuel cell performance.

Research also outlines how we can study the catalyst layer-membrane via computer simulations. However, there is significantly less theoretical research compared the experimental data reported. To our understanding, there is almost little to nothing currently researched in simulated work on the patterned interfaces. This is an essential field of interest in the quest to improve the validity of PEMFCs in the future and is something that this thesis hopes to build upon.

In subsequent chapters, a variety of different interface morphologies will be investigated. Varying the height and frequency of peaks impacts the power performance indicated by the polarisation curves and maximum power density output of the PEMFC.

Furthermore, the addition of surface roughness to the model interfaces will be considered as a more closer situation to the practical fuel cells.

Chapter 4

Methodology

This chapter focuses on the building of a coherent half-cell model for the cathode catalyst-membrane interface within a PEMFC. By first understanding the planar interface model, provided by the COMSOL Multiphysics model library, we can build a data base of results that can be used as a base point to compare all other results against. By patterning the morphology of the interface, we can begin to evaluate how varying the degree of patterning influences the current density, local overpotential, and overall power density of the modelled PEMFC, by comparing it to the base line results of the planar model.

The chapter also covers all the parameters used, as provided by the default model, and goes into detail over any changes made to these parameters, such as when building a user-defined mesh.

4.1   Introduction

In chapter 2, the literature reviewed show that varying the patterning on the morphology of the interface between the electrolyte membrane, and the catalyst layer at the cathode, can have a positive influence on the overall performance of a PEMFC by improving the oxygen reduction reaction (ORR). However, most research into altering the patterned surface of the interface has been through the addition of pillars, or channels. There has not been such research carried out on other geometries, which could be explored.

One of the leading issues which causes the reduction in the ORR over time is the build up of water at the interface. Patterning the interface with parallel channels, similar to Deshmukh et. al, in 2010 [14], was shown to improve power density performances at high humidity, suggesting the parallel channels offered a flow route for water to escape the system more efficiently. Building on this concept, it would be of interest to see how rather than opting for a cuboid prismatic channel structure, instead a triangular prismatic interface is used.

As a starting model to work on, we look into the model library in COMSOL Multiphysics. The model titled 'Mass Transport and Electrochemical Reactions in a Fuel Cell Cathode' shows a half cell consisting of a thin cathode catalyst layer adjacent to a thin electrolyte membrane, with an inlet region applied above the cathode, as shown below in figure 4.1. There is no anode adjacent to the opposite side of the membrane because we are only focusing on the ORR which takes place at the interface between the electrolyte membrane, and the cathode catalyst layer.
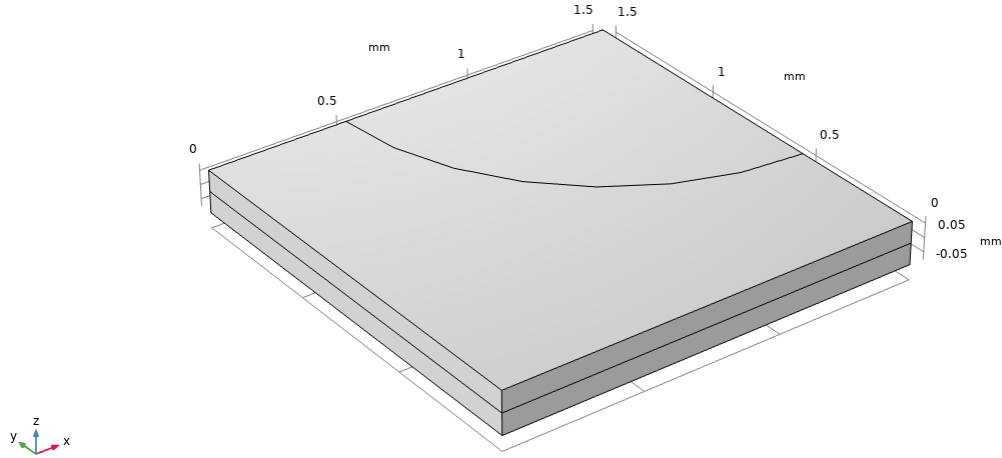
Figure 4.1: Model of PEMFC Half-cell with Planar Interface.

The model in Figure 4.1 consists of two domains, the electrolyte and the electrode, and can be further split into 12 boundaries. The images below show each boundary separately highlighted.
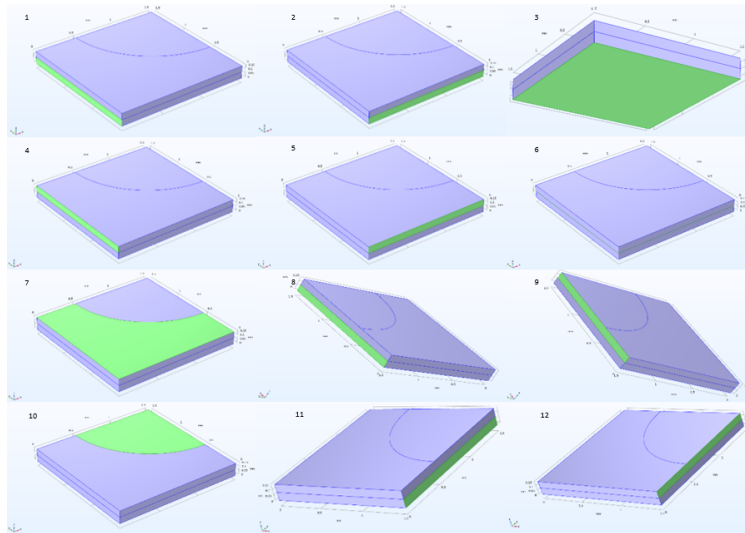
Figure 4.2: Image Showing all 16 Faces of the Default Model.

The geometry of the model supplied by COMSOL Multiphysics originally consisted of two blocks, which were defined as the membrane and the catalyst layer, with the

boundary between the two blocks acting as the site of the ORR. This simple geometric structure works very well for the planar model. However, generating more complicated geometries requires the use of a parametric surface between two domains. For the benefit of consistency, the provided model was rebuilt to include a parametric surface, and then data was recollected.

Before explaining how the model is structured, it is important to explain what the model represents on a larger scale. Figure 4.3. shows how the model used in COMSOL Multiphysics is a unit cell of a much larger system, which consists of a thin cathode adjacently above a thin electrolyte membrane, with an array of inlets that allow the inflow of oxygen. Obviously, due to practicality reasons, there is little benefit to modelling the whole system, when modelling power requirements running time can be greatly reduced by targeting the unit cell of the system.
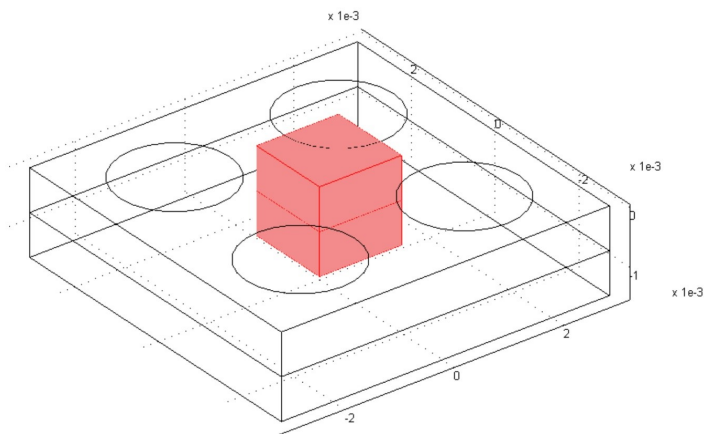
Figure 4.3: Schematic showing how the model is a unit cell of a larger system (units in metres) [27].

The model's geometry consists of a 1.5 mm by 1.5 mm base for the cathode and electrolyte membrane. Each with a thickness of 0.075 mm, with a quarter circle inlet with a radius of 1 mm.

The model is split into two domains. A lower domain, corresponding to a solid electrolyte interconnecting the anode and cathode of the fuel cell, and an upper domain, corresponding to the cathode. There are no pores present to allow gas flow, and there is not any electronically conductive material present.

4.1.1 Assumptions and Limitations

Whilst using the half cell model can provide beneficial information in predicting experimental outcomes in advance, in order to observe the influence of multiple variables, the model has to be simplified so that computation times are realistic for producing adequate amounts of data. Therefore, these required simplifications resulted in a number of assumptions and limitations.

Firstly, since the model is of a half cell consisting on only a membrane and catalyst layer, assumptions must be made in regards to the apparent anode on the other side of the membrane, where it is assumed there is a uniform inflow of hydrogen ions across the membrane towards the membrane-catalyst layer interface, as well as an equally uniform inflow of electrons through the bipolar plate.

This leads onto the second assumption of the model. Given the model only consists of a membrane and catalyst layer, there is not a bipolar plate or GDL within the model. As already mentioned, this limits the understanding of the inflow of electrons to the reaction interface, but also restricts our understanding of the inflow and outflow of reactants and products respectively via the GDL, which is important when discussing water management at the interface

Another assumption of the model is the assumption that there is perfect contact between the membrane and the catalyst layer. In practice, during the fuel cell fabrication process, when the membrane and catalyst layer are pressed together, pockets of air can be trapped at the interface, reducing performance by leading to the accumulation of liquid water in the interface voids.

Lastly, given the degree of randomness during the manufacturing process, it is not possible to accurately simulate any defects that may occur during the fabrication of the fuel cell. For example, any defects in the structure of the membrane due to the heat treatment required when fabricating the patterned membrane.

4.1.2 Materials

Although the most commonly used materials for the cathode and membrane in model fuel cells are a low-cost metal core, such as carbon, with a platinum coating, and Nafion respectively, these materials were not available in COMSOL Multiphysics' data base, and thus the key variables were included in the default model. These included the ionic conductivity of the membrane (5 S/m), the ionic conductivity of the cathode (1 S/m) and the electrical conductivity of the cathode (1000 S/m) [181].

4.1.3 Secondary Current Distribution

A Secondary Current Distribution interface is used to model the electronic and ionic current balances, accounting for the effect of electrode kinetics in addition to solution resistance [182].

Stationary equations shown below were used to solve for potentials ϕ_s and ϕ_l in the electrode and electrolyte phases respectively.

$$\nabla.i_l = Q_l \quad \text{and} \quad i_l = -\sigma_l \nabla \phi_l \tag{4.1}$$

$$\nabla.i_s = Q_s \quad \text{and} \quad i_s = -\sigma_s \nabla \phi_s \tag{4.2}$$

Where Q is the current source, and σ is the electrode or electrolyte's conductivity [183].

To solve for the potentials ϕ_s and ϕ_l, the anode side of the cell is grounded at 0V, whilst the current collector boundary at the cathode is set to a cell potential, which was defaulted at -0.19 V.

Within the electrolyte, whose potential is corresponding to equation 4.1, the model input temperature was set to 293.15 K, or room temperature, whilst the ionic conductivity was defined by its materials properties, at 5 S/m.

Thermal insulation properties, following:

$$-n.i_l = 0 \quad \text{and} \quad -n.i_s = 0 \tag{4.3}$$

were used.

4.1.4 Transport of Concentrated Species

A Transport of Concentrated Species interface was used to model the species mass transport in the cathode by the Maxwell-Stefan equations for the mass fractions of

oxygen, water and nitrogen in the gas phase [184][185][186].

$$\frac{\nabla \mu_i}{RT} = \nabla \ln a_i = \sum_{j=1}^{n} \frac{\chi_j}{D_{ij}}(\vec{v}_j - \vec{v}_i) = \sum_{j=1}^{n} \frac{c_j}{cD_{ij}}\left(\frac{\vec{J}_j}{c_j} - \frac{\vec{J}_i}{c_j}\right) \qquad (4.4)$$

where μ is chemical potential, χ is mole fraction, D_{ij} is the Maxwell-Stefan diffusion coefficient, c is total molar concentration and J is flux.

Inlet mass fractions of the three gas species are set corresponding to a humidified air mixture at 90% relative humidity (RH) at atmospheric pressure, with the pressure and resulting velocity vector solved by using the Darcy's Law interface.

Standard free energies of formation and reaction entropies were used to calculate the reference equilibrium potentials for the higher temperatures, according to [187]:

$$E_{eq,ref}(T) = \frac{\triangle G^0(T - T^0) \triangle S^0}{nF} \qquad (4.5)$$

where $T^0 = 25°C$ denotes the temperature of the standard state, whilst the cell operates at $80°C$.

The equilibrium potentials of the electrode reactions depend on the local partial pressures in accordance with the Nernst equation [188]:

$$E_{eq} = E_{eq,ref}(T) - \frac{RT}{nF}ln\prod_{i}\left(\frac{p_i}{p_{ref}}\right)^{v_i} \qquad (4.6)$$

where v_i are the stoichiometric coefficients of the reacting species, p_i is the partial pressure of the reacting species and $p_{ref} = 1$ atm is the reference pressure.

The Bulter-Volmer equation is used to define the cathode electrode kinetics across the whole cathode [168][189]:

$$i_{loc,O_2} = i_{0,ref,O_2} \left(\left(\frac{p_{H_2O}}{p_{ref}} \right)^2 \left(\frac{\alpha_{\alpha,O_2} F \eta_{ref,O_2}}{RT} \right) - \frac{p_{O_2}}{p_{ref}} exp \left(\frac{\alpha_{c,O_2} F \eta_{ref,O_2}}{RT} \right) \right) \quad (4.7)$$

where η_{ref} is the overpotential with respect to the reference state, and is defined as:

$$\eta_{ref,O_2} = \phi_s - \phi_l - E_{eq,ref,O_2} \quad (4.8)$$

Assuming ideal kinetics according to the mass action law,

$$\alpha_{\alpha,O_2} + \alpha_{c,O_2} = n \quad (4.9)$$

where α_{α,O_2} is the anode reduction charge transfer coefficient, α_{c,O_2} is the cathode reduction charge transfer coefficient, and n is the number of electrons transferred in the reaction. For this reaction, the value of n is 1. Tafel slopes can be used to calculate the values of α_{α,O_2} and α_{c,O_2}, although unless otherwise stated, they are normally both 0.5 respectively [190].

A volumetric current source term in the electrode domain is created by multiplying the local current density expression in the cathode by $10^9 m^2/m^3$.

Since the kinetics for the anode are assumed to be so fast, a linearized Butler-Volmer expression was used on the anode boundary [191]:

$$i_{loc,H_2} = i_{0,ref,H_2}\left(\left(\frac{p_{H_2}}{p_{ref}}\right)^2\left(\frac{\alpha_{\alpha,H_2}F\eta_{ref,H_2}}{RT}\right) - \frac{p_{H_2}}{p_{ref}}exp\left(\frac{\alpha_{c,H_2}F\eta_{ref,H_2}}{RT}\right)\right)$$
$$\approx i_{0,ref,H_2}\left(\frac{p_{H_2}}{p_{ref}}\right)^{\frac{\alpha_{c,H_2}}{n}}\left(\frac{nF\eta}{RT}\right) \quad (4.10)$$

Assuming $\alpha_{\alpha,H_2} + \alpha_{c,H_2} = n$

And since the anode boundary was grounded, the overpotential is defined as,

$$\eta = 0 - \phi_l - E_{eq,H_2} \qquad (4.11)$$

No mass transport effects or any current distribution along the depth of the anode electrode were considered because we assumed the partial pressure of hydrogen was constant on the anode boundary.

4.1.5   Meshing

The default model provided by COMSOL Multiphysics used a physics-controlled mesh consisting of evenly distributed elements defined with a fine element size, with the parameters shown in Table 4.1 [181].

Table 4.1: Default meshing parameters that the original model used

Parameter	Value
Maximum Element Size (mm)	0.12
Minimum Element Size (mm)	0.015
Maximum Element Size Growth Rate	1.45
Curvature Factor	0.5
Resolution of Narrow Regions	0.6
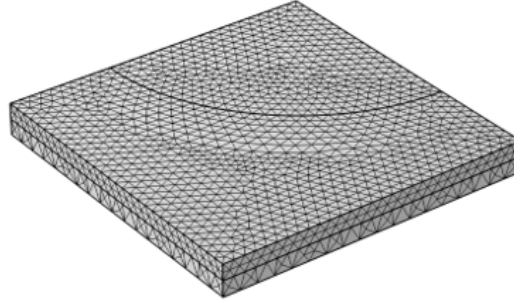
Figure 4.4: Resultant meshing profile given the default meshing parameters.

Although viable for simple geometries, such as the default planar model, moving forward, the more complex geometries, consisting of sharper angles at the ORR interface require a more detailed mesh. As such a user-defined element size was used, consisting of the parameters listed in the table below.

Table 4.2: Readjusted meshing parameters.

Parameter	Value
Maximum Element Size (mm)	0.02
Minimum Element Size (mm)	0.0025
Maximum Element Size Growth Rate	1.35
Curvature Factor	0.3
Resolution of Narrow Regions	0.85

A finer mesh could have been used. However, this would have led to significantly longer computation time, with the added precision not warranting the additional time taken, as shown in the analysis below.
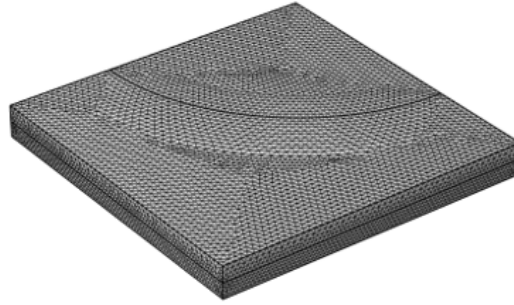
Figure 4.5: Resultant meshing profile given the adjusted meshing parameters.
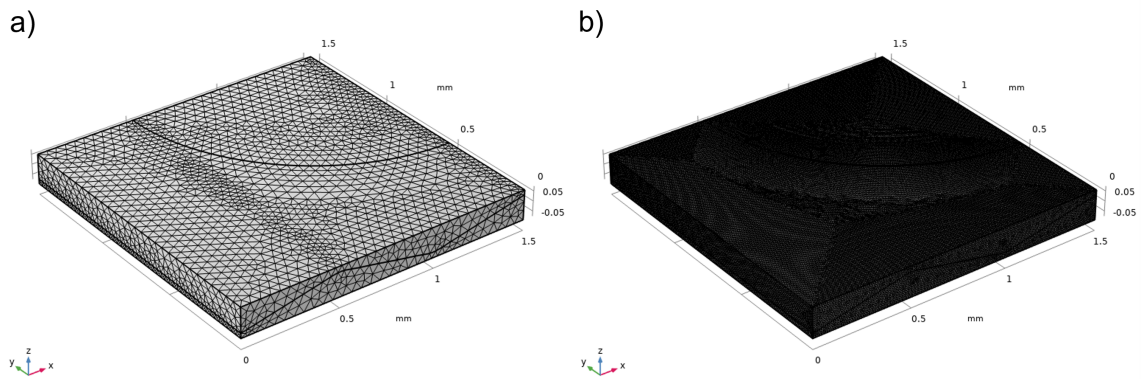
Figure 4.6: Images of models prismatically patterned with peaks of 0.1mm height at a frequency of 10 peaks per mm, with a maximum element size (mm) of a) 0.05 and b) 0.01.

Figure 4.6 shows a clear distinction in the number of elements present within the model when using a finer maximum element size. It would be expected that this would result in more accurate data, but at the cost of much larger computation times.
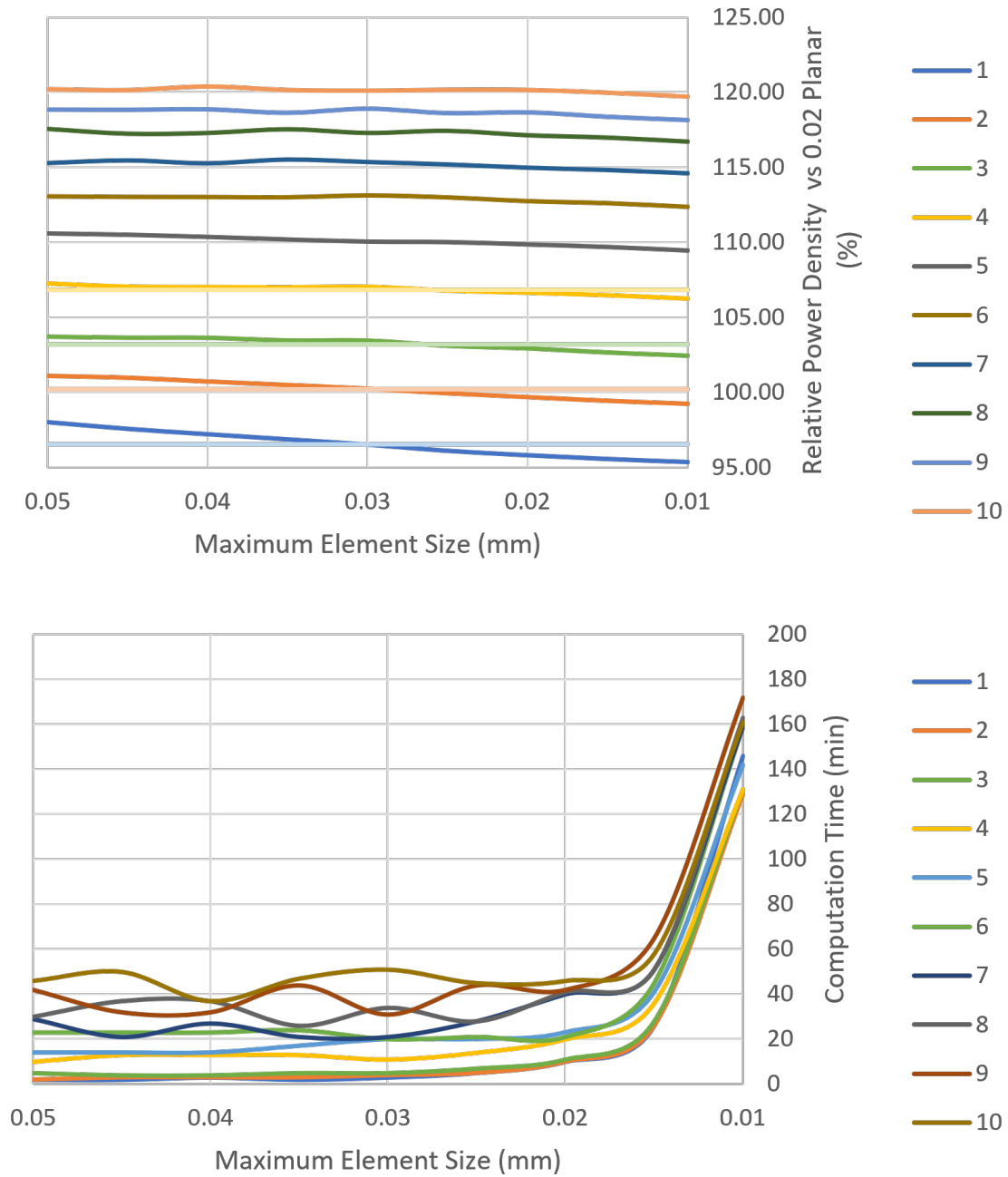
Figure 4.7: Graphs showing the impact of maximum element size on computation time and performance compared to a maximum element size of 0.02mm

Figure 4.7 shows that decreasing the maximum element size from 0.05 mm to 0.02 mm gives a minor improvement in the accuracy of data, without any noticeable change in computation time. For models consisting of a higher frequency of peaks, there was a fluctuation in computation time. This is believed to be due to the mesh struggling to uniformly build around the geometry of the more complex regions of the models. However, despite these fluctuations, the average computation times within the 0.05 mm to 0.02 mm range were fairly consistent.

However, reducing from 0.02 mm to 0.01 mm showed a jump in computation time from roughly 10-50 minutes per model, up to roughly 130-170 minutes per model, equivalent to a 340-1300% increase in computation time, for an improvement in the accuracy of the data of 0.05%.
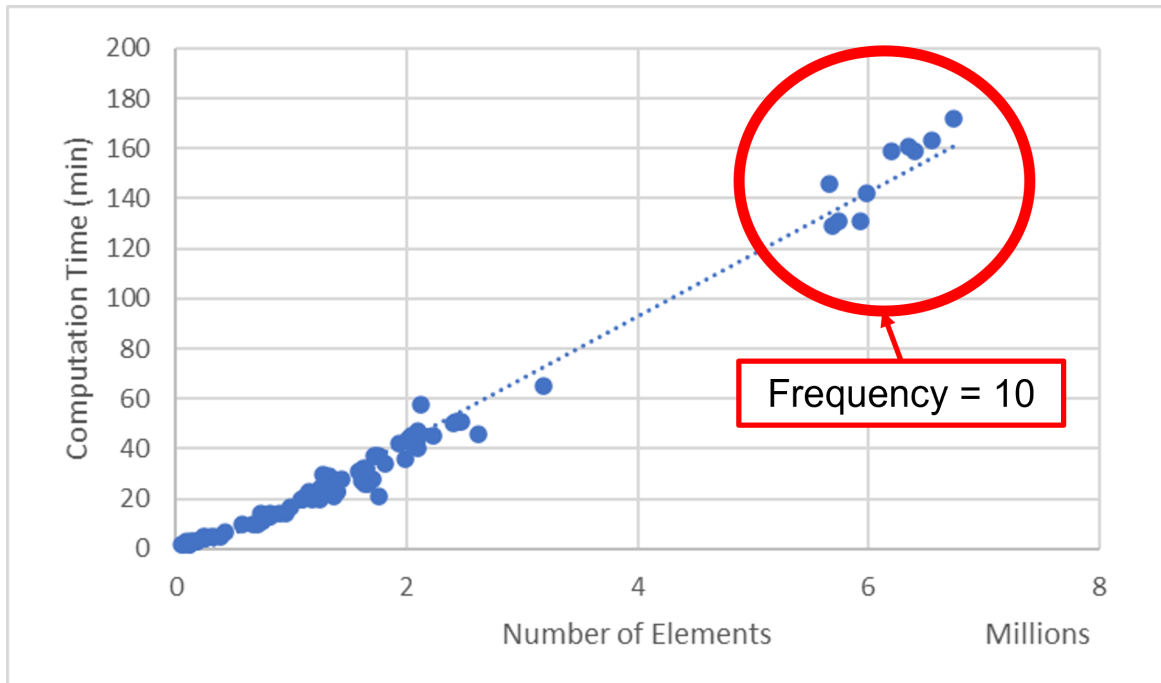
Figure 4.8: Graph showing the correlation between total number of elements in a model mesh, and the computation time.

The cause of the increase in computation time as the maximum element size is reduced, is because of the increased total number of elements. As shown in Figure 4.8, there is a very strong positive correlation between the total number of elements, and the resultant computation time. As shown by the data points within the red circle, which are the 'frequency = 10' models, there is a significant jump in the number of elements when the maximum element size is 0.01 mm, at around 5-7 million, compared to less than 3 million for all but one of the other data points.

The improvement in accuracy of data does not warrant the additional computation time required to run the models, so a maximum element size of 0.02 mm should be used.

Decreasing the maximum elemental growth rate (MEGR) means that the disparity between adjacent elements in the mesh will be smaller, leading to a finer mesh. Typically, the MEGR can only go up to 1.5, so having a MEGR of 1.45, as is the case for the default model, is very large. The curvature factor is an important component in defining the fineness of a mesh. The curvature factor controls the size of the boundary elements compared to the curvature of the geometric boundary. The size of the boundary elements is dependent on the product of the curvature factor and the curvature radius, so a smaller curvature factor would result in a finer mesh along curved boundaries, as would be seen by reducing the curvature factor from 0.5 to 0.3. A high resolution of narrow regions increases how close the elements are to form an equilateral shape. Having more equilateral triangles allows for better conditions for accurate Finite Element Method (FEM) modelling. This would be improved by increasing the resolution of narrow regions by increasing it from 0.6 to 0.85, as seen

when comparing Figures 4.4 and 4.5 with each other.

However, upon completing a mesh optimisation analysis on minimum element size, MEGR, curvature factor and resolution of narrow regions, it was found, as shown in Figure 4.9, varying the parameters had little to no impact on data results. As such, these would not be altered moving forward.
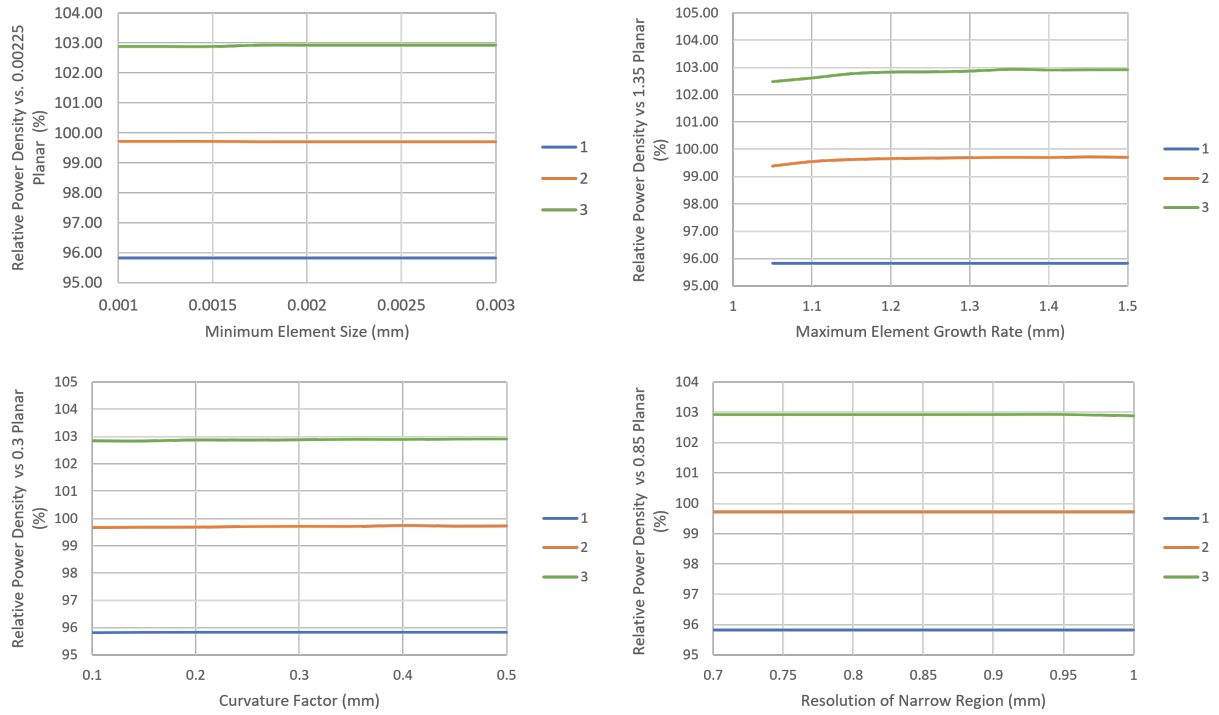
Figure 4.9: Graphs showing the impact of minimum element size, maximum element growth rate, curvature factor and resolution of narrow regions, on data results

Table 4.3 displays all the starting parameters used for building the planar model, taken from the COMSOL library. Further parameters are included in later models, but these will be shown when they become applicable.

Table 4.3: Table showing all used parameters for the default model [36].

Name	Value	Units	Description
i0	0.001	A/m^2	Exchange current density
S	1×10^9	1/m	Specific area
T	353	K	Temperature
sigma_s	1000	S/m	Effective conductivity, solid phase
e_por	0.4		Porosity
c_o2_ref	3.6641	mol/m^3	Oxygen reference concentration
p_atm	1.01×10^5	Pa	Ambient pressure
perm	3×10^{-13}	m^2	Permeability
mu	3×10^{-5}	Pa·s	Viscosity
k_d	3.16×10^{-8}	W/m	Emperical MS diffusivity expression prefactor
v_o2	1.66×10^{-5}		Diffusion volume, O2 (Fuller, Schettler, Giddlings relation)
v_h2o	1.27×10^{-5}		Diffusion volume, H2O (Fuller, Schettler, Giddlings relation)
v_n2	1.79×10^{-5}		Diffusion volume, N2 (Fuller, Schettler, Giddlings relation)
M_o2	0.032	kg/mol	Molar mass, O2
M_n2	0.028	kg/mol	Molar mass, N2
M_h2o	0.018	kg/mol	Molar mass, H2O
w_h2o_ref	0.1446		Inlet mass fraction, O2
D_o2n2	2.75×10^{-5}	m^2/s	Maxwell-Stefan diffusivity
D_o2n2_eff	6.95×10^{-5}	m^2/s	Effective MS diffusivity
D_o2h2o	3.50×10^{-5}	m^2/s	Maxwell-Stefan diffusivity
D_o2h2o_eff	8.86×10^{-5}	m^2/s	Effective MS diffusivity
D_n2h2o	3.50×10^{-5}	m^2/s	Maxwell-Stefan diffusivity
D_n2h2o_eff	8.85×10^{-5}	m^2/s	Effective MS diffusivity
E_pol	-0.19	V	Cathode Polarisation

Since the computational demands required to run each simulation is much greater than that can be met by a typical desk computer, a remote server was used to connect to a more powerful computer, which had access to both Matlab and COMSOL Multiphysics. At present, it would seem that the addition of having access to Matlab would not matter, given COMSOL Multiphysics is the only modelling software required. This is true; however, Matlab is very important for saving time. For the planar interface, the models can be simulated relatively quickly. However, with the intentions of patterning the interfaces, as well as eventually looking into the application of roughness to the interfaces, the expected running time for each simulation would

be substantially longer due to the complexity of the models. This is where Matlab could be beneficial. With the current set up, a model could be set up in COMSOL Multiphysics, and once the simulation is completed, the data can be collected, the parameters can be changed, and the new model can be re-run. The issue with this is that it is very time consuming, and requires someone being present at the computer, ready for when the simulation finishes. Matlab offers a superior alternative. By using LiveLink between Matlab and COMSOL Multiphysics, a list of parameters can be selected, for example, height = 0.01-0.1 mm, with 0.01 mm intervals, and frequency = 1-10 peaks per mm, with 1 peak per mm intervals. In this case, LiveLink could be set up to run all 100 models consecutively one after the other without the requirement of somebody being on-guard. This would allow models to be run during inconvenient hours, such as in the middle of the night, or during weekends, significantly improving the efficiency of data collection. Additionally, another benefit of using LiveLink between Matlab and COMSOL Multiphysics is that Matlab does not require building the graphical user interface (GUI) for each model, as would be the case for COMSOL Multiphysics. This would result in a time saving for each individual model as well.

4.2 Data Analysis

Whilst most PEMFCs traditionally have featured planar interfaces between the membrane and the electrodes, there has been interest in the potential for improved results in performance due to the patterning of these interfaces. Since the ORR at the cathode interface is significantly slower than the Hydrogen Oxidation Reaction (HOR) at the anode, and thus the rate limiting step, we have focused on how varying the morphology at the cathode/electrolyte influences the fuel cell performance.

The key performance output we are focusing on is power density output.

$$\text{Power Density output} = I(V - OP) \tag{4.12}$$

where V is the cell potential, I is the current density and OP is the overpotential voltage losses.

Before altering the morphology of the interfaces, we first needed to record statistical data for a half cell model with a pristine planar interface.

Table 4.4: Table showing the results of interest for the default model under a cathode polarisation of -0.19V

Fuel Cell Model Interface	Planar
Current Density (A/cm^2)	0.06779
Overpotential (V)	0.18868
Power Density (W/cm^2)	0.055
Surface Area (cm^2)	0.0225
Membrane and Catalyst Layer Volumes (cm^3)	$1.6875\text{x}10^{-4}$
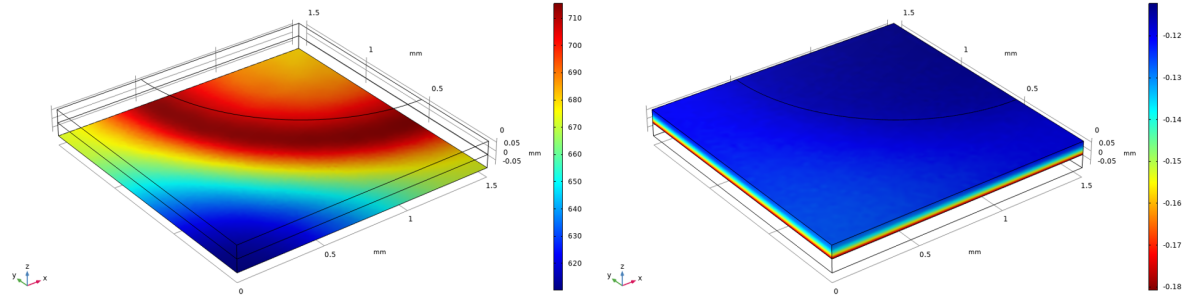
Figure 4.10: Visual display showing a) the average current density and b) the average overpotential of a half-cell with a planar interface.

Figure 4.11 shows the polarisation curve (blue) and power density (orange) curves produced by collecting data points at various cathode polarisations (E_{pol}). By changing the input value of E_{pol}, this causes a difference in the resultant current density and overpotentials of the PEMFC. This allows us to build a polarisation curve like shown below.
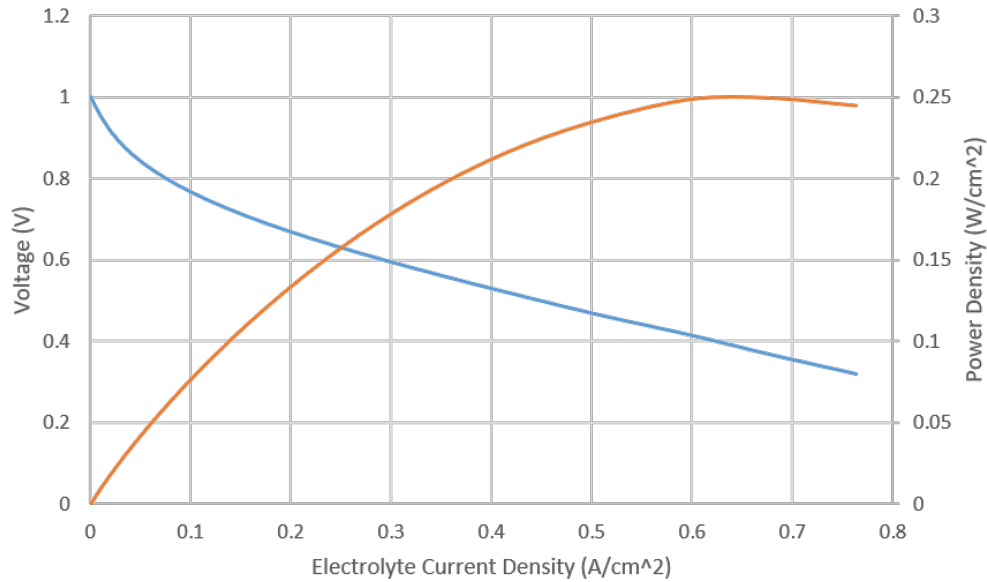
Figure 4.11: Graph showing the polarisation curve (blue) and power density curve (orange) for the default model.

Although the theoretical ideal voltage of a PEMFC, according to the Nernst equation (equation 4.6), is 1.23 V, due to the voltage losses throughout the fuel cell, this in practice is never achieved.

There are three types of voltage losses as indicated in Chapter 1.3; activation losses, ohmic losses and mass transport losses.

The activation losses are why the y-intercept of the curve is not at 1.23 V, but rather 1 V. A value of 1 V was chosen because this value is usually the open circuit voltage (when the current density is 0 A/cm^2) reported in the literature [192][193].

In commercial and industrial use, the optimal voltage required from a PEMFC is between 0.6-0.7 V [194]. For the polarisation curve above, this offers a current density of between 0.16-0.29 A/cm^2. This is significantly lower than the usual power performance for a single cell, which is 1 A/cm^2 at a voltage of 0.6 V [195].

The simplicity of this default model could be a feasible argument for why these values are so different from what is considered to be 'standard'.

4.3 Conclusions

In this chapter, an assessment was made into the default model provided by COMSOL Multiphysics, looking into the important parameters and variables chosen. A closer look was made into the model itself, and what it represents as part of a larger system, as well as understanding which equations were used to define certain operations, such as the Maxwell-Stefan equations being used to define the transport of concentrated

species, whilst the cathode electrode kinetics were defined by the Bulter-Volmer equation. Alterations were made when building a user-defined mesh which would result in a finer and more accurate model, producing more reliable results.

An explanation was made into the reasoning and benefits of some approaches into how the simulations would take place, such as using LiveLink between Matlab and COMSOL Multiphysics as a means to improve the efficiency of computational resources and time.

Lastly, an assessment of the default model's performance was made, namely the polarisation curve, power density curve and maximum power density, which will be used as a baseline when comparing all future models against which will be discussed in the following chapters.

Some experiments were also conducted to evaluate the results from the prismatic patterned membrane. Because this happens in Chapter 5, the experimental details will be included there.

Chapter 5

Prismatic Geometry

When looking into alternative interface morphologies, the first step is to decide upon which variables can be controlled. And, from there, the influence by varying these parameters on the power performance of the model can then be understood. In this chapter, a patterned membrane with prismatic geometry is studied, together with the pattern frequency and the prism height. The experiments are also conducted with hot embossing membranes to evaluated the simulation results.

5.1   The Interface

The first design that was considered is a prismatic interface with a zigzag design along the x-z face, which have peaks of varying frequency and height.

To build the interface with a prismatic morphology, the equation is calculated for the curve shown in Figure 5.1, which is then applied to a parametric surface.

Figure 5.1: 2D geometry of interface required for a prismatic morphology, where H is the height of the peaks and F is the frequency of the peak per mm.

The equation required to generate the above design is,

$$z = abs(F \cdot x - floor(F \cdot x) - 0.5) \tag{5.1}$$

where F is the frequency of the peak in the X-axis.

Currently, if this equation is used for building the morphology of the interface, there will be two significant problems:

1. There is no means of varying the height of the peak.

2. There is no consideration into maintaining a constant volume of the membrane and catalyst layer.

To allow for the height of the peaks to be easily controlled, the previous formula needs to be multiplied by 2*H,

$$z = abs(F \cdot x - floor(F \cdot x) - 0.5) \cdot 2H \tag{5.2}$$

where H is the height of the peak.

5.2 Maintaining a Constant Volume

With the adjustment to the equation made to allow for control over the height of the peak, the morphology can then be changed from the planar interface to complicated geometries similar to Figure 5.2.
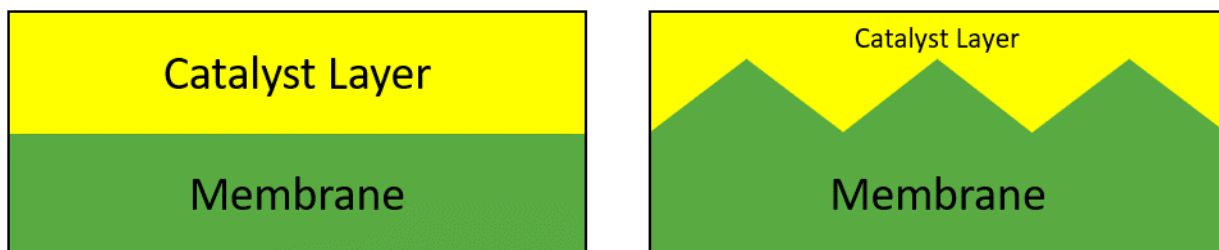
Figure 5.2: 2D Schematic showing the difference between the planar and prismatic interfaces.

It can be seen that the addition of these peaks not only increases the surface area, and thus the volume of the membrane, but also decreases the volume of the catalyst layer. This means any changes in output results can not be knowingly accounted for exclusively by the change in the morphology of the interface. For this to be the case, the starting position of the interface must shift downwards to accommodate for the change in the volume.
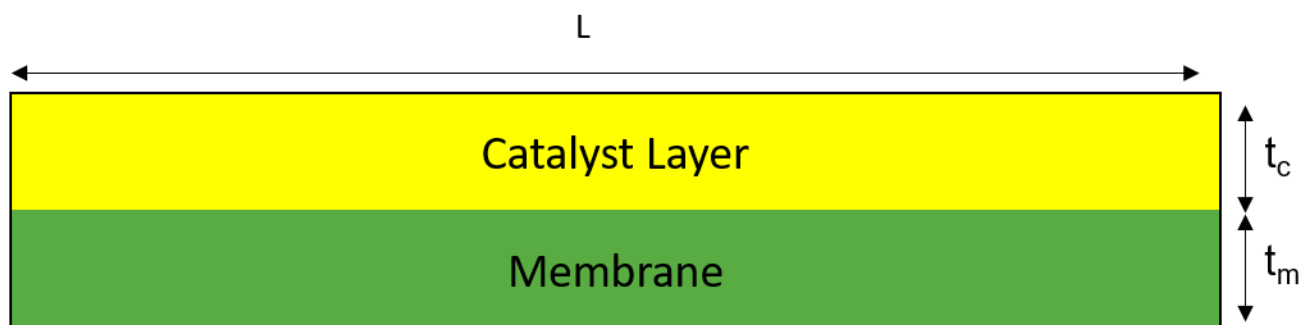
Figure 5.3: Schematic showing the original volumes of the catalyst layer and membrane with a planar interface, where t_c and t_m are the thickness of the catalyst layer and membrane respectively.

Before calculating the shift required in the z-axis, the volume of the catalyst layer

needs to first be calculated for the catalyst layer and membrane with a planar inter-

face.

$$V_M = Lt_m D \tag{5.3}$$

$$V_{CL} = Lt_c D \tag{5.4}$$

where V_M and V_{CL} are the volumes of the membrane and catalyst layer respectively,

D is the depth in the y-axis, and t_m and t_c are the thickness of the membrane and

catalyst layer respectively.
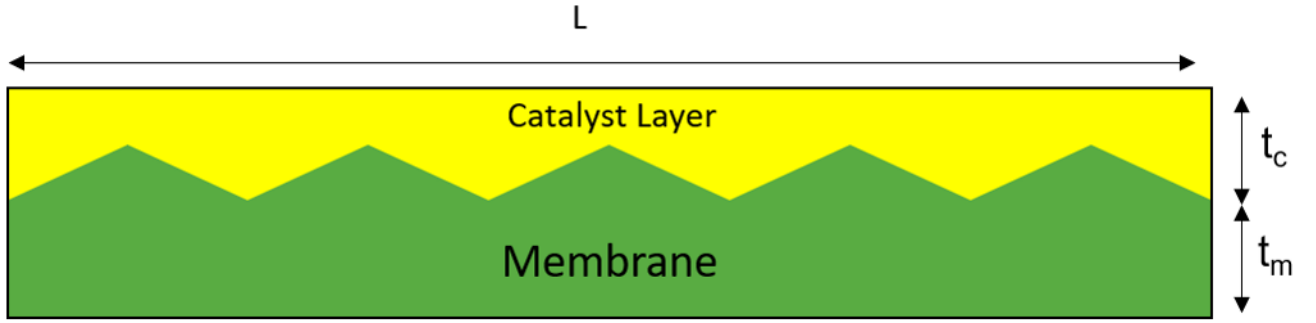
Figure 5.4: Schematic showing how not adjusting the position of the interface leads
to inconsistencies in the volumes of the membrane and catalyst layer.

To calculate the new volumes of the membrane and catalyst layer, the volume increase

due to the prisms needs to be added to the membrane's volume, and similarly deduct

the volume of the prisms from the original volume of the catalyst layer.

$$V_P = \left(\frac{H}{2F} \cdot D \right) \tag{5.5}$$

$$V_M = Lt_m D + LFV_P \tag{5.6}$$

$$V_{CL} = Lt_c D - LFV_P \tag{5.7}$$

Where F is the frequency of peaks per mm, and V_P is the volume of one prismatic peak.

By shifting the starting height of the interface on the z-axis, the constant volumes of the membrane and catalyst layer can be maintained.
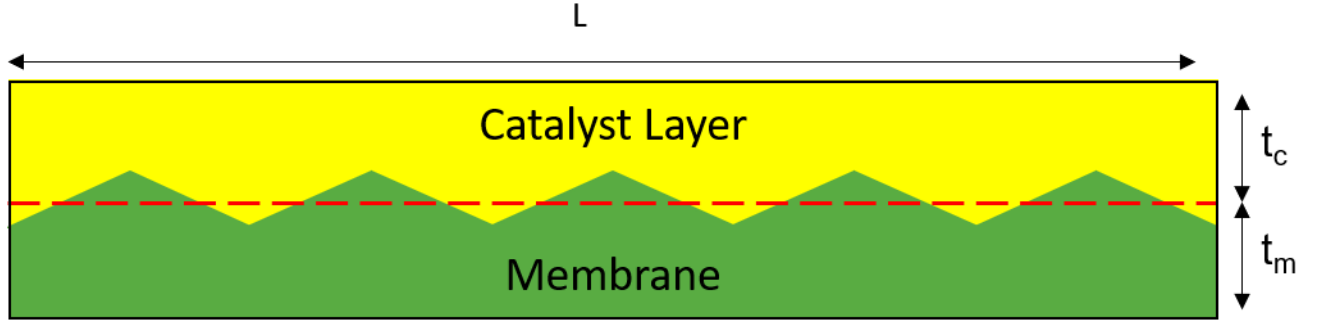
Figure 5.5: Schematic showing how adjusting the position of the interface can maintain constant volumes of the membrane and catalyst layer.

It can be shown that by shifting the starting position of the interface by half of the peak height, the peak creates an equal increase and decrease in both the volumes of the membrane and the catalyst layer, as shown in Figure 5.5.

$$V_M = Lt_mD + LFV_P - (LF - 1) \cdot V_P + 2 \cdot \frac{V_P}{2} = Lt_m \tag{5.8}$$

$$V_{CL} = Lt_cD + LFV_P + (LF - 1) \cdot V_P + 2 \cdot \frac{V_P}{2} = Lt_c \tag{5.9}$$

Therefore, to maintain a constant volume of the membrane and catalyst layer, we have to alter the starting position of the interface from (0,0,0) to (0,0,-$\frac{H}{2}$).

There are two approaches that can be used when building the models. Firstly, an option is to build each individual geometry for each specific set of parameters. This approach is the simplest and easiest in the short term, however, it takes a lot more

time to build and run each model, ultimately reducing the productivity. A faster and better approach is to build a script in Matlab, that can build and run a separate individual model in COMSOL Multiphysics for each variation of parameters.

When generating the models consisting of these new prismatic morphologies, it is important that all other parameters in the model are consistent with the original model. So, the only changes in the model are the frequency of the peak in the interface, and its height. Therefore, any changes in the model results can only be attributed to these variable changes.

Rather than writing the Matlab script directly into Matlab, a much faster approach used was to build the model in COMSOL Multiphysics, and then save that as an 'm' file, which could display the script automatically in Matlab. A new script was then written to allow for models to be consecutively run and saved automatically, whilst certain desired parameters were varied.

Models were generated, varying the height of the peaks from 0.01-0.1 mm, equivalent to 6.67-66.67% of the relative height of the model, and varying the frequency from 0.67-26.67 peaks per mm.

Figure 5.6 shows the four main stages required for building the geometry of the models. The example shows peaks of 0.1 mm in height, equivalent to 66.67% of the relative height of the model, and a frequency of 10 peaks per mm, equating to 15 peaks across the 1.5 mm base.
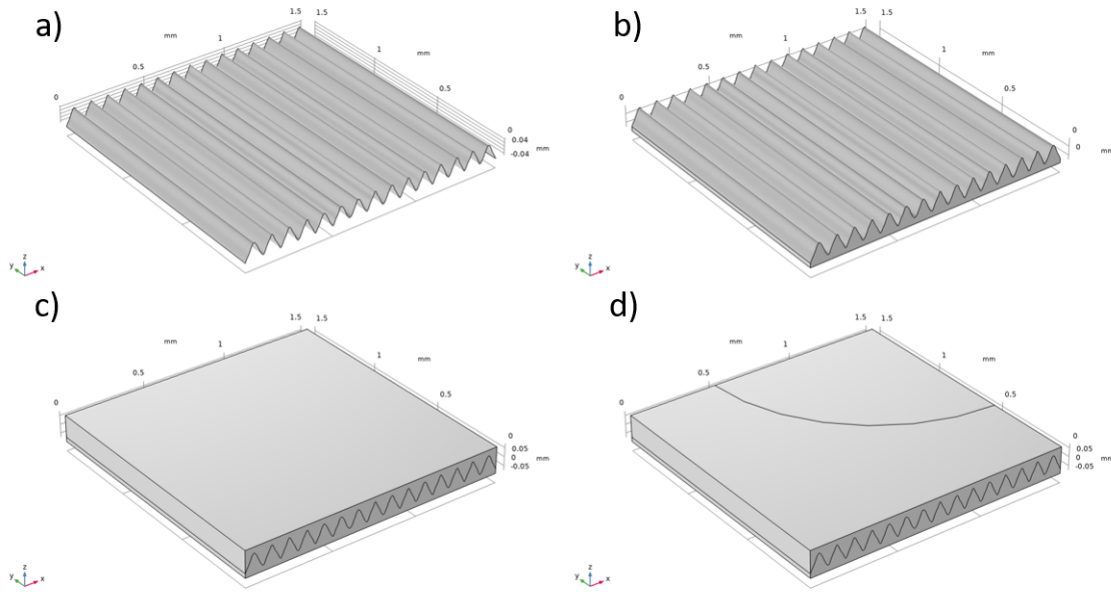
Figure 5.6: Images showing the progression of building the prismatic model geometry with a frequency of peaks of 5 peaks per mm and height of 0.1mm a) Constructing the interface b) Adding the membrane c) Adding the catalyst Layer and d) Applying an inlet.

Stage a) required building a flat parametric surface, and then changing the equation for the z-values of the starting coordinates calculated above. Stage b) involved the addition of a block, which was then partitioned into two domains, separated by the parametric surface, with the top domain being deleted from the model, leaving the membrane with the patterned interface. Stage c) involved a similar process to stage b) in order to build the catalyst layer above the interface. Finally, stage d) involved applying an additional boundary to the catalyst layer domain which would be the oxygen inlet.

5.3   Data Analysis

Figure 5.7 shows the relationship between frequency and relative height of the peaks with the cell power density. A strong positive correlation is obtained between increas-

ing the relative height and frequency of peaks, and a consequential increase in the cell power density compared to the planar interface, for all frequencies greater than two peaks per mm. Above F=2, increasing either the height, the frequency, or both always result in an improved power density output. This is believed to be due to an increase in the active surface area due to the patterning of the interface, increasing the available reaction cites for ORR. However, there is a noticeable drop in performance at very low frequencies. This can be ascribed to the disruption to the interface resulting from the inclusion of the patterning to the interface, which outweighs the positive influence of the increased surface area.
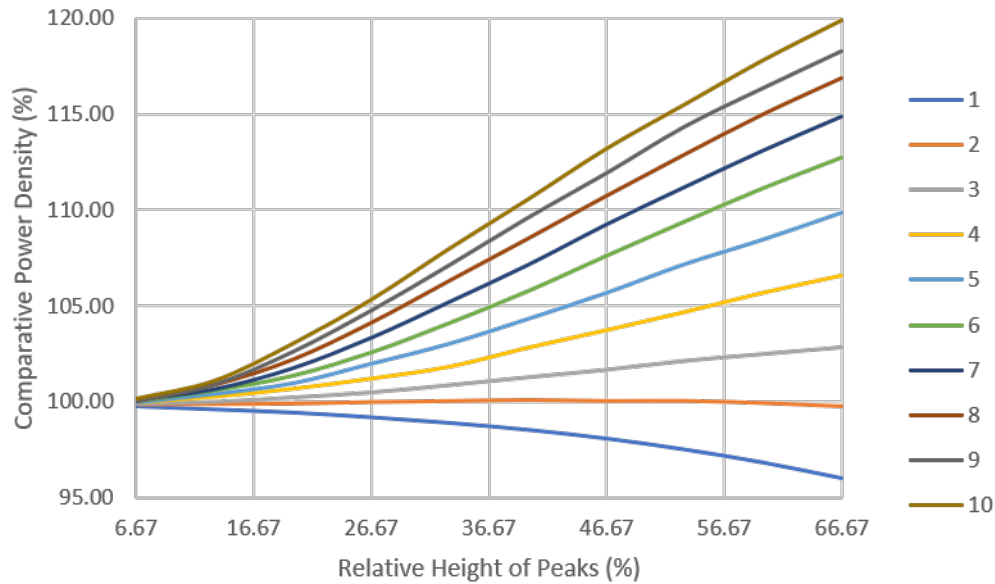
Figure 5.7: Chart showing the impact frequency (1-10 peaks/mm) of peaks and the relative height of the peaks has on power density compared to the planar model.

Quantitatively, although there is an improvement in performance at the lower frequencies, such as F=3, compared to the planar model, an increase of 2.86% is a lot smaller than, for example, the 19.89% improvement in power density observed for the interface prismatically patterned with peaks at a frequency of 10 peaks per mm at a

relative height compared to the total height of the model of 66.67%. This is to be expected, as once again, increasing the height of the peaks will directly result in a larger active surface area.

Previous research has also suggested that patterning the membrane can reduce the ohmic resistance because of the decreased thickness of the membrane at some points, as well as decreasing the mass transport resistance because of the generated void spaces between the catalyst layer and the electrolyte membrane [196][197][198].

However, these very promising results should be taken with caution. This data is very theoretical, and does not account for any defects to the membrane which is not practical during the fabrication process of patterned membranes. For example, if the membranes are patterned via a heat treatment method, this could lead to defects in the membrane, which would impact on the fuel cells performance. Unfortunately, the simulated models can not account for these concerns.

5.3.1 Surface Area

When assessing the plausible reasons for this improvement in the power performance, the most obvious reason is the increase in active surface area over the interface for ORR to take place. With that in mind, it is worth understanding the relationship between the surface area and the cell power density.

In order to generate a graph displaying the influence of surface area against power density, two formulae had to be calculated to work out how varying the frequency and height of peaks affected the surface area.

For the simplest case, the planar interface, the surface area is:

$$L^2 = 1.5\text{mm} \cdot 1.5\text{mm} = 2.25\text{mm}^2 = 0.0225\text{cm}^2 \tag{5.10}$$

where L is the length and width of the model area.

To calculate the surface area of the prismatic interface, we have to first calculate the surface area of a single prism, by using Equation 5.11,

$$\text{Surface Area} = (S_1 + S_2 + S_3) \cdot l \tag{5.11}$$

where the sum of S_1, S_2 and S_3 is the perimeter of the base, and l is the length of the prism.

Figure 5.8 shows a schematic representation of this equation.
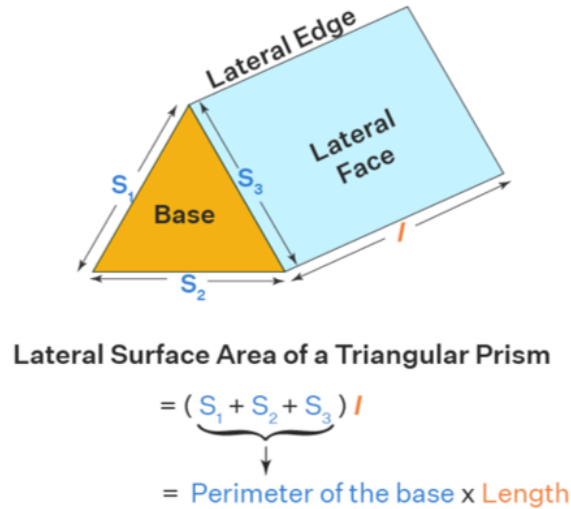
Figure 5.8: Schematic showing how the lateral surface area of a triangular prism can be calculated [28].

However, in order to be able to use this formula correctly, the terms for S_1, S_2, S_3 and l need to be replaced with the variables L, H and F.

$$l = L \tag{5.12}$$

Since we are not interested in the base surface area because in practice this will not be in contact with the catalyst layer in the membrane electrode assembly, so,

$$S_2 = 0 \tag{5.13}$$

$$S_1 = S_3 = \sqrt{\left(\frac{1}{2F}\right)^2 + H^2} \tag{5.14}$$

Therefore, equation 5.11 can be rewritten as,

$$A = \left(2\sqrt{\left(\frac{1}{2F}\right)^2 + H^2}\right) \cdot L \tag{5.15}$$

which can be rearranged and simplified to,

$$A = \frac{L}{F}\sqrt{1 + (2HF)^2} \tag{5.16}$$

This is suggested to be the surface area of one triangular prism. To calculate the total surface area of the interface, equation 5.16 must now be multiplied by the total number of prisms, dependent on the frequency of peaks.

$$\text{Total Prismatic Surface Area} = \left(\frac{L}{F}\sqrt{1 + (2HF)^2}\right) \cdot LF = L^2\sqrt{1 + (2HF)^2} \tag{5.17}$$

The 3D surface plots shown in Figure 5.9 display how increasing the frequency of peaks, and the height of the peaks increases the surface area of the interface, and how that corresponds to a correlating improvement in relative power density compared to the planar interface.
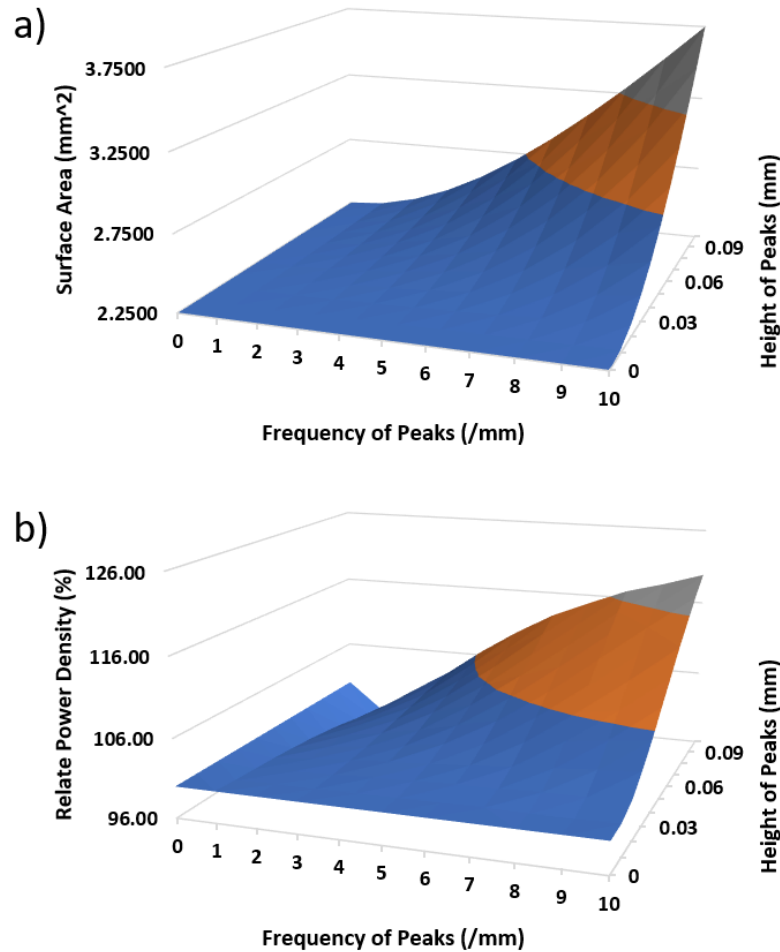
Figure 5.9: 3D Plots showing a) the impact of frequency and height of peaks has on the surface area of the Interface, and b) the impact of frequency and h of peaks on power density for the prismatic model relative to the planar model.

Figure 5.10 agrees with this theory. There is a positive trend between the surface area and the power density. However, the magnitude of this trend is dependent on the frequency of peaks. Over the fixed surface area offered by the unit cell of 1.5 x

1.5mm^2, increasing the frequency of peaks results in the largest power density. However, this power density appears to start to plateau.
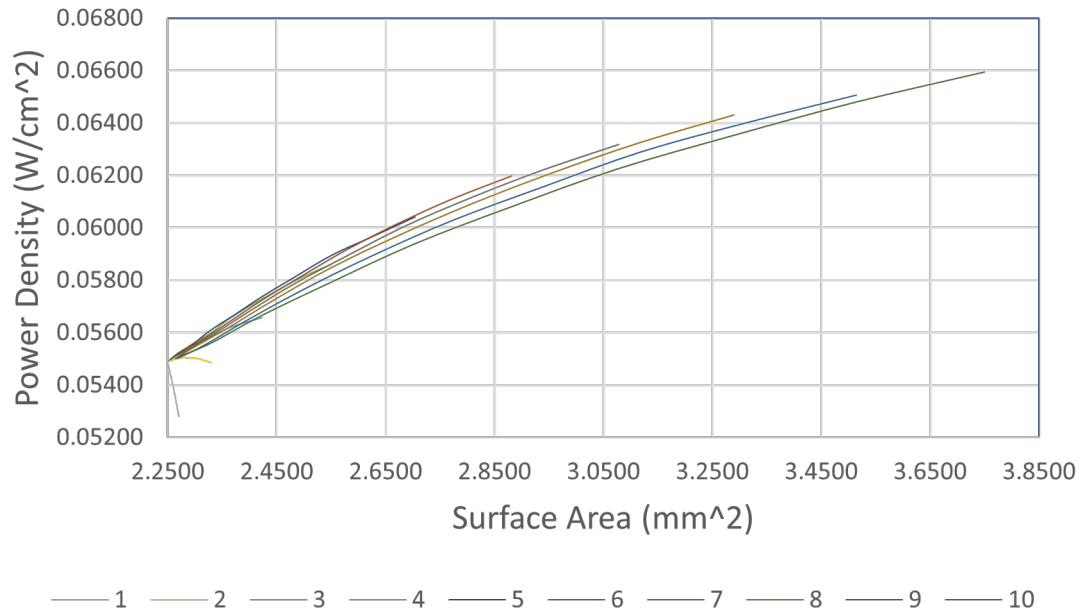
Figure 5.10: Graph showing how the surface area impacts power density, and how the frequency of peaks influences to what degree this impact is, for the prismatic model at peak heights of 0.1 mm.

This makes sense, given that when increasing the height of the peaks, the change for the increase in surface area will become less effective, until it is eventually insignificant, and thus plateaus. Although the lower frequency peaks (F>2) are seen to be still increasing in the power density, it can be seen that they are also beginning to plateau. However, as can be seen by the purple curve for the frequency of 10 peaks per mm, the curve is plateauing at high power densities, which is later shown quantitatively in Table 5.2. This argument suggests that to achieve the best power density for a fuel cell, a larger frequency is required with a larger height of the peaks. However, depending on the specific desire, it might be better to go with a lower frequency. As shown in Figure 5.10, although the larger frequency curves reach a greater surface

area, having a lower frequency means that for the same surface area of the interface, a greater comparative power density can be achieved. This could be summarized by saying that if having a fixed surface area was important, then,

Low Frequency + Large Height of peaks > High Frequency + Small Height of peaks

However, the feasible height of the peaks is restricted by the geometric parameters of the fuel cell. The above statement suggests that it is optimal for the height of the peak to be very large although this can possibly lead to problem in the integrity of the membrane, resulting in reduced performance, which the model can not account for.

It can be suggested from Figure 5.10 that at some point, increasing the frequency of peaks will no longer result in an increase in the power density output, as the results begin to plateau. Unfortunately, due to the complexity of the model at higher frequencies of peaks, a conclusive value of power density, for which this plateau occurs at, can't be accurately determined. However, an estimated plateau can be predicted by taking trendlines for each curve and extrapolating them. The trendlines for each curve obtained from Figure 5.10 are listed in Table 5.1.

The equations of power density trendlines provide us with some useful insight. The algebraic structure of a quadratic equation is $y = ax^b + c$, where 'y' is the power density and 'x' is the surface area. By finding the maximums of these equations, by differentiating them, the maximum power density can be estimated, and also the surface area required for each frequency of peaks to maximise the power density can be estimated, as listed in Table 5.2. From here, the surface area values can be en-

Table 5.1: Table showing the power density trendline equations of each curve from Figure 5.10.

Frequency of Peaks	Equation of Polynomial Trendlines
1	$-35.792x^2 + 157.220x - 170.11$
2	$-4.239x^2 + 19.383x - 19.71$
3	$-1.166x^2 + 5.879x - 4.89$
4	$-0.457x^2 + 2.745x - 1.42$
5	$-0.345x^2 + 2.252x - 0.31$
6	$-0.249x^2 + 1.780x - 0.31$
7	$-0.208x^2 + 1.553x - 0.01$
8	$-0.170x^2 + 1.366x + 0.27$
9	$-0.140x^2 + 1.166x + 0.52$
10	$-0.105x^2 + 0.956x + 0.82$

tered back into the quadratic trendlines to calculate the respective maximum power densities for these frequencies of peaks. In reality, it makes sense to suggest that the surface area of the interface can be increased by increasing the height or frequency of peaks. However, what this estimation suggests, is that there will be a plateau in improvement at this point.

Table 5.2: The differential equations of the quadratic trendlines from Table 5.1 and the estimated surface areas on the interfaces and resultant maximum respective power densities, provided the height of peaks is 0.1 mm.

Frequency of Peaks	$\frac{dy}{dx}$	Max Surface Area (mm^2)	Max Power Density (W/cm^2)
1	$-71.584x + 157.22$	2.196	2.541
2	$-8.478 + 19.383$	2.286	2.447
3	$-2.331x + 5.879$	2.522	2.526
4	$-0.914x + 2.745$	3.002	2.699
5	$-0.691x + 2.252$	3.260	2.792
6	$-0.498x + 1.780$	3.575	2.876
7	$-0.416x + 1.553$	3.731	2.889
8	$-0.341x + 1.366$	4.008	3.007
9	$-0.280x + 1.166$	4.165	2.949
10	$-0.210x + 0.956$	4.558	2.996

Table 5.2 shows what the maximum surface area and respective maximum power

densities that can be achieved for each frequency of peaks individually. However, a quadratic trendline can be generated for the maximum surface areas shown in Table 5.2, which can be differentiated and set to 0 to calculate the overall maximum power density, and the corresponding frequency required to achieve this. Values for $F = 1$ and 2 were ignored for this calculation, since their negative performance for the previously mentioned reasons skewed results inappropriately.
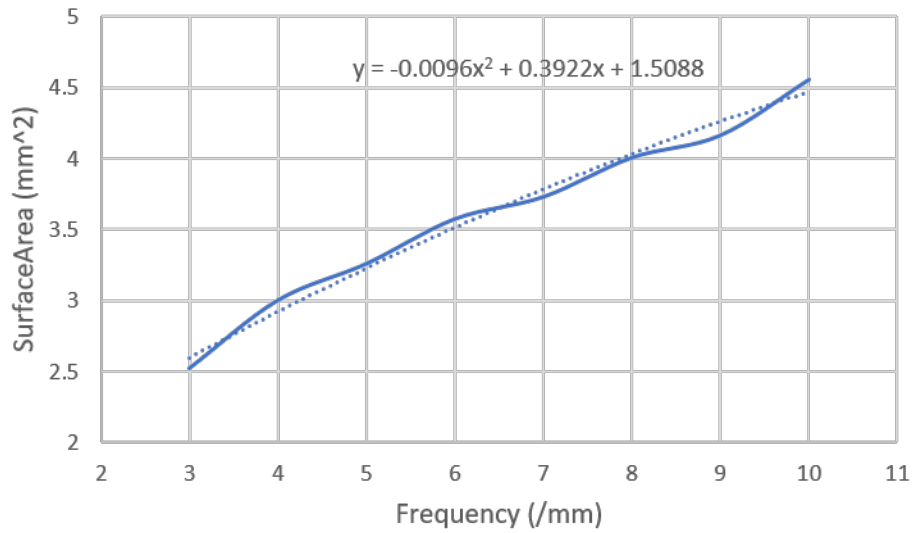
Figure 5.11: Trendline of the maximum power density results vs maximum surface area results from Table 5.2.

$$\text{Surface Area vs Power Density Trendline } y = -0.0096x^2 + 0.3922x + 1.5088 \quad (5.18)$$

$$\frac{dx}{dy} = -0.0192x + 0.3922 \quad (5.19)$$

$$\text{If } \frac{dx}{dy} = 0, \text{ then } x = 20.4271 \text{mm}^2$$

This means the maximum surface area that can be achieved according to equation 5.18 is 20.4 mm^2. Inserting this result into equation 5.18, gives a maximum power

density of 5.515 W/cm^2.

By rearranging equation 5.17, the frequency of peaks required to achieve these results can be calculated.

$$F = \frac{1}{2HL^2}\sqrt{A^2 - L^4} \qquad (5.20)$$

where F is the frequency of peaks, H is the height of peaks, L is the length of the geometry and A is the surface area of the interface.

This gives a value of F of 45.1 peaks per mm.

This could still be an issue if the frequency of peaks required results in a patterned membrane that is too fine to be fabricated. A patterned membrane with a frequency of peaks of 45.1 peaks per mm, at a height of 0.1mm, results in prisms of 100 μm in height and a base width of 22.2 μm. Atomically, this is much larger than the size of an atom, 0.1 nm. This means the angle of the tips of the peaks would be,

$$\theta = 2 \cdot \tan^{-1}\frac{11.1}{100} = 12.7° \qquad (5.21)$$

These are plausibly achievable dimensions for the peaks of a patterned membrane. However, due to limitations in COMSOL Multiphysics, running simulations using these parameters was unfeasible, due to the very long run times, and the possible convergence issues.

5.3.2   Polarisation Curve

The standard form of displaying how good a fuel cell is in terms of performance is through a polarisation curve. Figure 5.12 compares the polarisation curves and power density curves of the planar model and the prismatic model with a frequency of 10 peaks per mm and a peak height of 0.1 mm, equivalent to a relative height of the peaks of 66.7% of the total model.
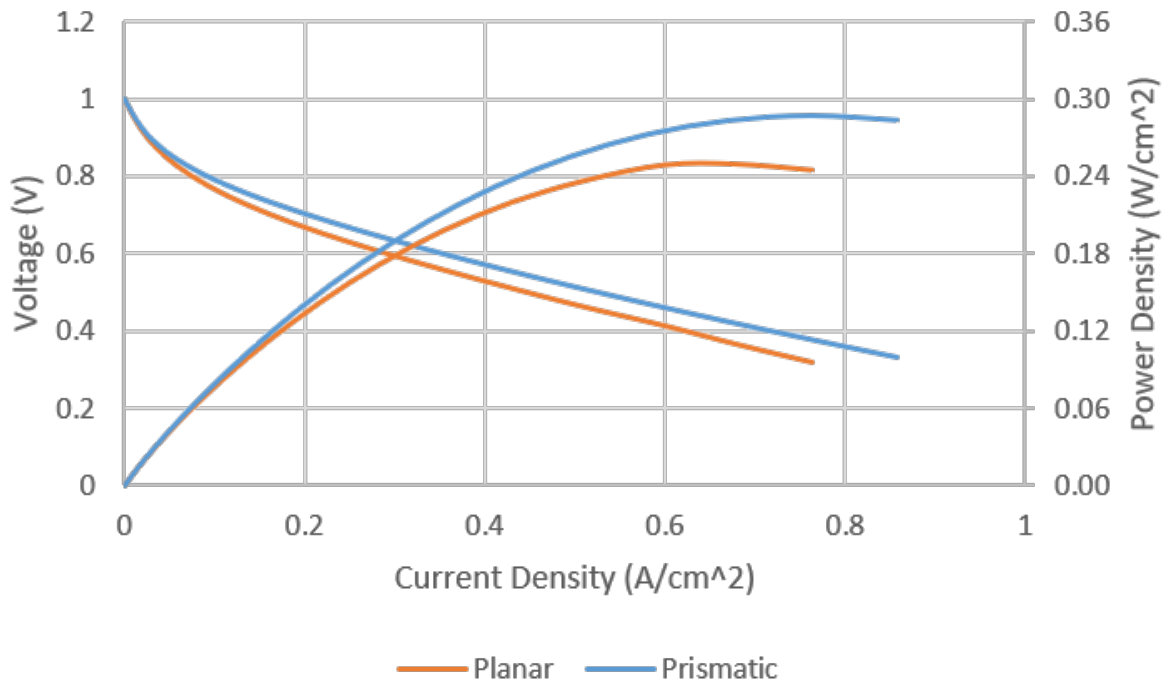
Figure 5.12: Polarisation curve and power density curve of the prismatic interface with 10 peaks per mm at a height of 0.1 mm (blue), compared with the respective curves of the planar interface (orange).

It is clear that there is a noticeable improvement in the performance as a result of the patterned interface. Depending on the desired voltage the fuel cell is to operate at, the improvement varies, but overall, there is an improvement in current density range. The power density, increases from 0.250 W/cm^2 to 0.287 W/cm^2, equating to a 14.8% improvement.

In industry, the voltage most commonly used is between 0.6 and 0.7 V. In this voltage range, the prismatic geometry can be approximated, by calculating averages across data points, showing a power density of 0.2047 W/cm^2 and 0.1384 W/cm^2 at 0.6 and 0.7 V respectively, which is a 19.09% and 22.91% respectively improvement in the power density output compared to those of the planar interface at the same voltages.

To find a more accurate value for the potential power density values that could be achieved with this prismatic model, compared to the planar model, the equations of the trendlines were fitted to the curves. To do this, the current densities of the planar and prismatic polarisation curves in the 0.6-0.7 V range were calculated from their trendlines, and then those values were put into the trendlines of their power density curves to determine the more accurate values.

For the planar interface:

$$V = -1.763J^6 + 5.2019J^5 - 6.1908J^4 + 3.7601^3 - 1.7476J^2 + .9073J + 0.0005 \quad (5.22)$$

Solving for V=0.6 and 0.7 gives a range of values for the current density of between 0.16 and 0.30 A/cm^2.

$$Pd = 77.251J^6 - 195.42J^5 + 193.27J^4 + 95.083^3 + 24.768J^2 - 4.0182J + 0.9933 \quad (5.23)$$

Solving for the current density, J, values of 0.16 and 0.3 A/cm^2 gives a range of power density values, for the planar model, of between 0.11 and 0.18 W/cm^2.

For the prismatic interface:

$$V = 39.739J^6 - 112.98J^5 + 125.31J^4 - 68.69J^3 + 19.651J^2 - 3.4616J + 0.9917 \quad (5.24)$$

Solving for V=0.6 and 0.7 gives a range of values for the current density of between 0.20 and 0.35 A/cm^2. That is equivalent to an improvement of between 20 and 31.25% in that voltage range. This is very comparable with the approximated data calculated above.

$$Pd = -1.7173J^6 + 4.8893J^5 - 5.4788J^4 + 3.1626J^3 - 1.5187J^2 + 0.914J + 0.0004 \quad (5.25)$$

Solving for the current density, J, values of 0.20 and 0.35 A/cm^2 gives a range of power density values for the Prismatic model, at a Frequency of Peaks of 10 peaks per mm and peak height of 0.1 mm, of between 0.14 and 0.21 W/cm^2, equivalent to an increase in the power density performance of 18.6-26.4%.

An explanation for the power performance improvement of the prismatic structure compared to its planar counterpart is believed to be two-fold. Firstly, the patterned morphology leads to an increase in the surface area of the interface. This allows for a larger active area and higher catalyst utilisation for the ORR to occur, and thus leads to an improved fuel cell performance. Secondly, as reported by Deshmukh et. al [14], the prismatic geometry offers clear flow channels for the water by-product of ORR to escape from the interface. This reduces the build up of water at the interface which can otherwise reduce the amount of available active surface area. However, given the simplicity of the model, such as a lack of a GDL, means this explanation is not applicable to the model.

5.4 Experimental PEMFC Single Cell Test

To evaluate the positive influence of the patterned interface obtained in numerical simulation, the experiment was also conducted to fuel cells by fabricating membrane electrode assemblies (MEAs) with the patterned membrane at the cathode side. The experiment was conducted under help from another PhD student (Mr Yang Li).

However, due to some confusion and a lack of time, insufficient data was collected to adequately compare the accuracy of the simulated results vs the experimental data.

5.4.1 MEA Fabrication

MEAs were fabricated and tested in single PEMFCs to evaluate the improvement results obtained with the numerical simulation. To make a patterned membrane, pieces of 36 cm^2 square Nafion 212 membrane and 16 cm^2 square stainless-steel mould with prism patterns were used. The mould was pressed onto the membrane at 140°C under a pressure of 3 MPa for 2 mins. To fabricate MEAs, the membrane side with the patterns was sprayed with catalyst ink and worked as cathode. The catalyst ink was prepared with probe sonication using commercial Pt/C catalysts (TKK, 46.2 wt%), isopropanol and 10% Nafion ionomer aqueous dispersion. The catalyst loadings at the cathode were 0.4, 0.2 and 0.1 mgcm^{-2} determined by the mass before and after the spraying. A 16 cm^2 commercial gas diffusion electrode (GDE) with a Pt/C catalyst loading of 0.2 mg$_{Pt}$cm^{-2} was used as the anode. The anode, membrane with the cathode and a Sigracet 39BC GDL at the cathode side were hot pressed at 135°C under 5 MPa for 2 mins to fabricate MEAs. For comparison, MEAs were also fabricated with a flat membrane without surface patterns. The MEA tests were carried out with a PaxiTech-Biologic FCT-50S PEMFC test stand. The cell temperature was 80°C with

fully humidified H$_2$/air at stoichiometry ratios of 1/1.5 without backpressure. The polarisation curves were recorded with a scan rate of 2 mVs^{-1} from 0.3 V to open circuit voltage (OCV).

5.4.2   Characterisation and MEA Test Results
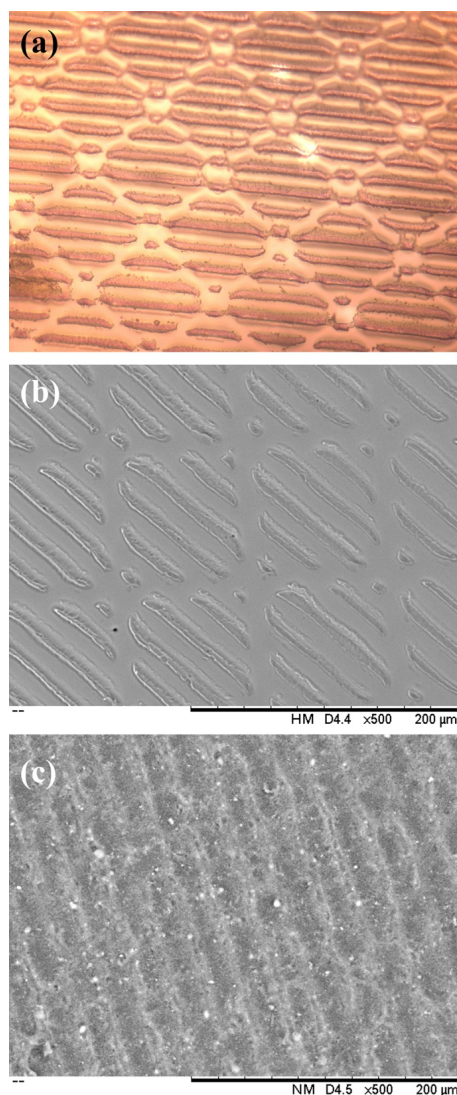
Figure 5.13: (a) Optical microscopy photo and (b) SEM image of a patterned Nafion 212 membrane (x20). (c) The patterned membrane with catalyst sprayed on the surface (Pt/C at a loading of 0.2 mg$_{Pt}$cm^{-2}).

The optical microscopy photo and SEM image of a patterned Nafion 212 membrane are shown in Figure 5.13a and 5.13b. Figure 5.13c displays the patterned membrane with catalysts sprayed on the surface (Pt/C at a loading of 0.2 $mg_{Pt}cm^{-2}$). The pattern peaks show a cycle width of about 30 μm, corresponding to a frequency of 33.33 peaks per mm. This patterned structure was successfully projected to the catalyst layer coated on the membrane surface (Figure 5.13c). This frequency is very close to the optimal frequency, 45.1, obtained by the numerical simulation in Equation 5.20.

Polarisation curves for the fuel cells made from the planar and patterned membrane with various catalyst loadings are shown in Figure 5.14a and 5.14b. At a high catalyst loading (i.e., 0.4 $mg_{Pt}cm^{-2}$), the catalyst layer is very thick (usually larger than 10 μm). The criteria for determining the power performance are the mass transfer characteristics within the catalyst layer, which is the same for both fuel cells. However, for patterned membrane, because of the prism surface after the catalyst coating, the interface contact between the catalyst layer and the electrolyte membrane is worse than the flat surface, leading to a more considerable ohmic loss, thus a relative lower fuel cell power performance. Nevertheless, with the decrease of the catalyst loading to a low value as $0.1mg_{Pt}cm^{-2}$, the catalyst layer is much thinner. The mass transfer through the catalyst layer is not a dominated issue any more. In this case, the advantage of the large interface area between the patterned membrane and cathode will become a significant contribution to the fuel cell performance; thus, a higher peak power density is recorded. A detailed comparison of the peak power density change with the catalyst loading is displayed in Figure 5.14c. This result is consistent with the results from the numerical simulation above, demonstrating the feasibility of using the numerical simulation and the positive effects from the using of the patterned cathode/electrolyte interface.
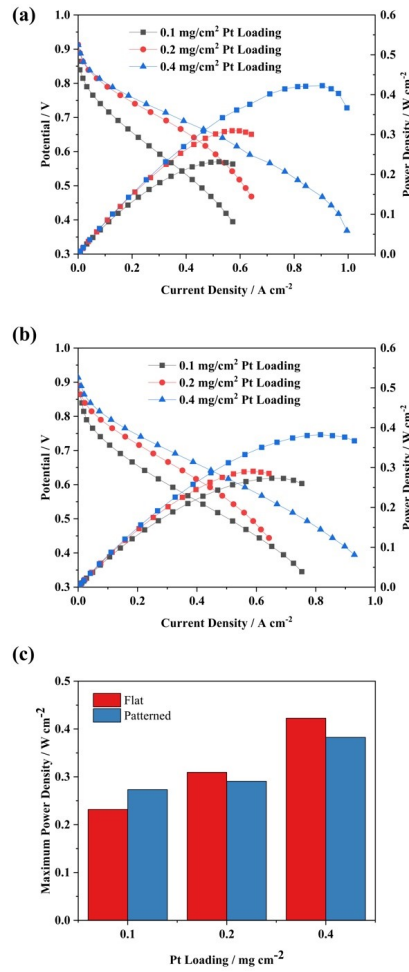
Figure 5.14: (a) Polarisation curves for the MEAs made from the planar and (b) patterned membrane with various catalyst loadings. (c) compares the normalized peak power density change trend for both membranes.

5.5   Conclusions

In this chapter, a push towards generating more complex geometries compared to the planar interfaces was carried out, starting with a prismatic morphology. This required first calculating the z-coordinate of the interface, relative to the frequency and height of the peaks.

Upon building the model with the newly patterned morphology, it became apparent that there was a resultant increase in volume of the membrane, and consequent decrease in volume of the catalyst layer, which would invalidate results when comparing against the planar model. As such, the required shift in the starting position of the interface was calculated.

Results showed a positive correlation between the frequency of peaks versus power density, as well as the relative height of peaks versus the power density, compared to the planar model. A possible cause of this is believed to be due to the increased active surface area, resulting in more active reaction sites available for ORR to be carried out. However, at low frequencies of peaks, performance is negatively impacted by patterning the interface, because a disruption to the previously perfect planar interface, which outweighs the benefits of the increased active surface area.

When comparing surface area against power density, there was a positive correlation, after an initial drop in performance at very low frequencies. However, the plot suggests after increasing the surface area to a very large region, the increase of the power density became plateaued. By extrapolating these curves, it was found that the required heights to reach the necessary surface areas to plateau were not realistically practical. However, if the height was fixed at 0.1 mm, or a relative height of 66.67%, it was found that the power density would plateau at a frequency of 45.1 peaks per mm, with a surface area of 20.4 mm^2.

Polarisation and power density curves of the prismatic interface were compared with the planar model, showing an improvement in performance of 17.0% in overall cur-

rent density, and 14.8% in maximum power density, whilst showing an improvement in current density of 19.09-22.91% across the practical operating voltage range of 0.6-0.7 V.

Nafion 212 membrane with a prismatic patterned surface was also fabricated into MEAs for the PEMFC single cell test to evaluate the numerical simulation results. The patterned interface with a frequency of 33.33 peaks per mm was compared with the planar interface with varying degrees of platinum loading at the cathode. The results demonstrated an improvement in the cell power performance due to an increase in the surface active area, in particular at the low catalyst loading, i.e., 0.1 $mg_{Pt}cm^{-2}$ where the active area had a dominated contribution.

However, at the high catalyst loading, the performance of the patterned membrane was inferior to the planar interface, due to ohmic losses associated with the poorer interface contact between the catalyst layer and the membrane. This is something that the current model can not account for as yet.

Today, the development of PEMFCs has moved to a stage for high power density operation with an ultralow catalyst loading below 0.1 $mg_{Pt}cm^{-2}$. Thereby, the use of a patterned membrane can play a significant role. However, as an early study here, the numerical simulation only included some basic parameters. This work is only a little evidence to suggest the potential function of the patterned membrane. The complexity of the functional patterned interface in real fuel cell operation conditions needs a much more detailed investigation, such as different patterns, random surface roughness, controlled porosity, oxygen and water mass transfer and catalyst/membrane contact at the interface, the influence of catalyst layer preparation technique, etc.

In the following chapters, we will conduct some further simulations based on the understanding from this chapter and the positive evaluation by experimental results.

Chapter 6

Other Geometry Interfaces

We have established that applying a patterned interface of prisms between the electrolyte and the cathode improved the power density of the fuel cell compared to the planar interface, with an overall positive correlation between peak size, peak frequency and the consequential power density.

However, although we know that having a high frequency of peaks and a high relative height is beneficial for the prismatic interface, there is no certainty that this is true for other geometries, and there is also an argument to be made to suggest that a prismatic morphology could be bettered by other pattern designs.

This chapter will study other geometries, including pyramidish, proper pyramid and waves geometries, which can be compared against one another, in an attempt to find which morphology proves to be the most beneficial when looking to optimise the maximum power density output of a fuel cell.

6.1 Pyramidish Geometry

One design that could be considered is an array of pyramids. The obvious character-istic of the previous discussed prismatic interface is that it is very one dimensional, as to say, there is a very significant difference in the morphology of the interface in the x-axis vs the y-axis. How would the power performance be impacted if the interface had a more symmetrical morphology, similar to pyramids rather than prisms?

Although this did not generate perfect pyramids, a patterned interface consisting of pyramidal peaks and troughs was generated by taking the formula used to build the prismatic interface in the x-axis, and adding the same formula to it, but in the y-axis, as shown in equation 6.1.

$$z = -(((\text{abs}(Fx \cdot x - \text{floor}(Fx \cdot x) - 0.5) - 0.25) \cdot 2 \cdot H)$$

$$+$$

$$((\text{abs}(Fy \cdot y - \text{floor}(Fy \cdot y) - 0.5) - 0.25) \cdot 2 \cdot H) \cdot 0.5 \tag{6.1}$$

where the parameters, Fx and Fy were used in place of F, for the frequency of peaks in the x and y directions. The first term of the formula is the original formula of the prismatic structure, whilst the second term is the addition to the equation that allows for the new geometry to be generated.
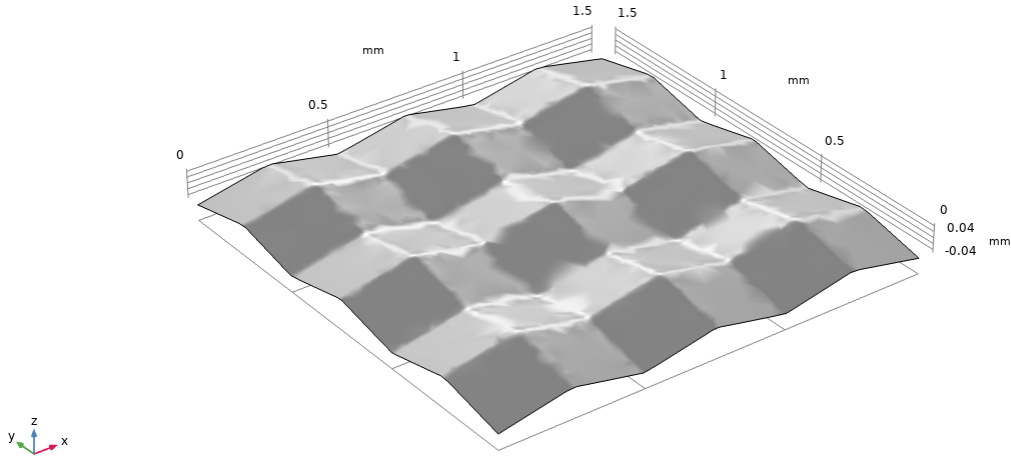
Figure 6.1: Pyramidish interface with a frequency of 2 peaks per mm, at a peak height of 0.1 mm.

With the new parameters in place, there are now three different variables that need to be controlled: the relative height of the peaks, the frequency of the peaks in the x-axis and the frequency of peaks in the y-axis. The height of the peaks in the x-axis and y-axis could be their own separate variables, but due to time restraints, they were kept the same as each other.

6.1.1 Calculating Surface Area and Volume

As with the prismatic geometry, changing the morphology of the interface by increasing the size and frequency of the pyramidal shape within the structure will change the surface area of the interface, as well as the volumes of the membrane and catalyst layer unless the z-coordinate of the interface is adjusted accordingly.

Calculating this change in surface area and volume is a lot more difficult to do compared to the prismatic interface, due to the complexity of the 3D geometry of the pyramids, as opposed to the 2D nature of the prisms, given they can be simplified to

an extruded zigzag.

For the Pyramidish geometry, firstly the shape will be defined in terms of the coordinates required to describe the shape. Secondly the equation describing a quarter of the surface will be determined and used to obtain the surface area and volume of the shape.

Pointwise Description

The shape has two-fold symmetry and is defined by the following nine points,

- $(0,0,0)$

- $\left(\frac{w_x}{2}, 0, \frac{H}{2}\right)$

- $\left(\frac{w_x}{2}, 0, H\right)$

- $\left(0, \frac{w_y}{2}, \frac{H}{2}\right)$

- $\left(\frac{w_x}{2}, \frac{w_y}{2}, H\right)$

- $\left(w_x, \frac{w_y}{2}, \frac{H}{2}\right)$

- $(0, w_y, 0)$

- $\left(\frac{w_x}{2}, w_y, \frac{H}{2}\right)$

- $(w_x, w_y, 0)$

where w_x and w_y are the width of the peak in the x and y axes respectively, and H is the height of the peak. These points connected to form four rectangles as seen in Figure 6.2.
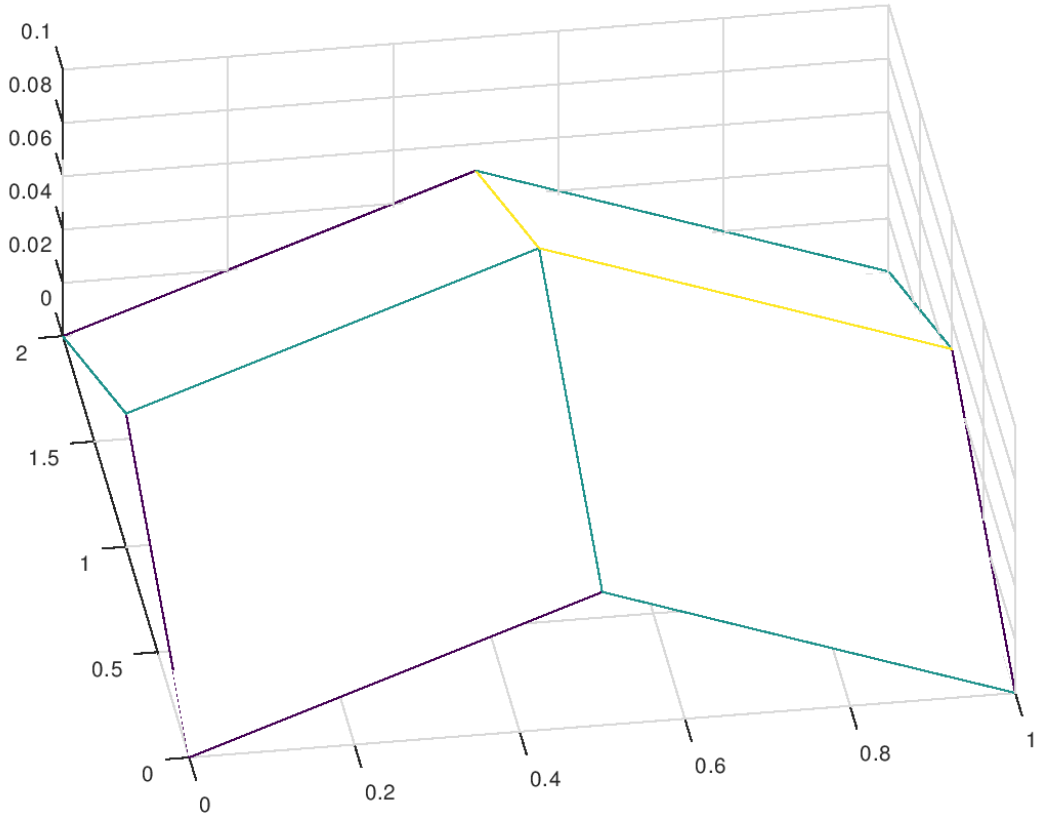
Figure 6.2: Mathematical representation of one peak, showing the nine points of the coordinate system. $w_x = 1$, $w_y = 2$ and $H = 0.1$.

In order to first calculate the surface area of the geometry, it is beneficial to prove that the interface shown in Figure 6.2 is a combination of four tilted rectangles.

The main criteria for a rectangle is that there are four edges which are all parallel and perpendicular to one another. It can certainly be seen that opposite edges are parallel to each other. Of the four coordinates, if the two mid-height coordinates are the same height as each other, then they must also produce a 90° angle between their two adjacent edges. Since the only term that controls the height of the coordinates is H, which is the same in both the x and y direction, this can be considered to be

true, and therefore the interface in Figure 6.2 can be considered as a combination of four tilted rectangles.

Due to the two-fold symmetry it is sufficient to consider one rectangle. Focussing on the pointwise the area is given by,

$$\text{Surface Area of 1 Rectangle} = \sqrt{\left(\frac{w_x}{2}\right)^2 + \left(\frac{H}{2}\right)^2} \cdot \sqrt{\left(\frac{w_y}{2}\right)^2 + \left(\frac{H}{2}\right)^2} \quad (6.2)$$

$$\text{Total Surface Area} = 4 \cdot \sqrt{\left(\frac{w_x}{2}\right)^2 + \left(\frac{H}{2}\right)^2} \cdot \sqrt{\left(\frac{w_y}{2}\right)^2 + \left(\frac{H}{2}\right)^2} = \sqrt{w_x{}^2 + H^2} \cdot \sqrt{w_y{}^2 + H^2} \quad (6.3)$$

where w_x and w_y are the width of the peaks in the x and y direction respectively, and H is the height of the peaks.

Equation for the Quarter Rectangle

The equation used for describing the quarter rectangle is,

$$z = \frac{Hx}{w_x} + \frac{Hy}{w_y} \quad (6.4)$$

with $x \in [0, \frac{w_x}{2}]$ and $y \in [0, \frac{w_y}{2}]$. The volume bounded by the plane at $z = 0$ is given by,

$$\text{Volume of 1 Rectangle} = \int_0^{\frac{w_y}{2}} \int_0^{\frac{w_x}{2}} z \, dx \, dy = \frac{Hw_xw_y}{8} \quad (6.5)$$

$$\text{Total Volume} = 4 \int_0^{\frac{w_y}{2}} \int_0^{\frac{w_x}{2}} z \, dx \, dy = \frac{Hw_xw_y}{2} \quad (6.6)$$

Maintaining a Constant Volume

The equations for the volumes of the original catalyst layer (V_{clo}) and membrane (V_{mo}) are,

$$V_{clo} = L_x L_y t_c \qquad (6.7)$$

$$V_{mo} = L_x L_y t_m \qquad (6.8)$$

where L_x and L_y are the lengths of the model in the x and y directions, and t_c and t_m are the thicknesses of the catalyst and membrane respectively.

However, with the inclusion of the new interface, the corresponding volumes of both the catalyst layer (V_{cl}) and membrane (V_m) change to,

$$V_{cl} = L_x L_y t_c - \frac{H w_x w_y}{2} \qquad (6.9)$$

$$V_m = L_x L_y t_m + \frac{H w_x w_y}{2} \qquad (6.10)$$

To maintain a constant volume, the starting z-coordinate needs to be adjusted away from the origin.

$$L_x L_y t_m = L_x L_y \big(t_m + z\big) + \frac{H w_x w_y}{2} \qquad (6.11)$$

$$z = -\frac{H w_x w_y}{2 L_x L_y} \qquad (6.12)$$

However, this is using w as a key term. To keep things consistent, it is better to substitute out w for F by using equation 6.13 ,

$$w = \frac{1}{F} \qquad (6.13)$$

Therefore, the starting coordinates for the interface must shift from (0,0,0) to

$(0,0,-\frac{H}{2L_x L_y F_x F_y})$

Having built the geometry for the pyramidal interface, when looking at the external boundary of the interface it may look as though the interface is lower than it should be, and thus resulting in an increased and decreased volume of the catalyst layer and membrane respectively. However, the average height of the interface is evenly distributed, since the height of the interface is higher internally.

Comparing Surface Area

As with the prismatic structure previously analysed, it is expected that the increased surface area of the interface will have a positive impact on the power performance of the fuel cell. However, it is not immediately obvious as to which of the two pattern designs will create a larger surface area compared to one another.

Since surface area proved to be an important parameter in comparing the power density output of the prismatic model, it is worth confirming that this relationship is true for other, and hopefully all, geometries.

We previously showed what the total surface area of one peak is in Equation 6.3. However, since $w = \frac{1}{F}$, this means,

$$A = \sqrt{\left(\frac{1}{F_x}\right)^2 + H^2} \cdot \sqrt{\left(\frac{1}{F_y}\right)^2 + H^2} \tag{6.14}$$

Since for the purposes of generating a 3D plot comparing frequency of peaks and height of peaks against either surface area or relative power density, we are only

considering models where $F_x = F_y$, this simplifies to,

$$A = \left(\frac{1}{F}\right)^2 + H^2 \tag{6.15}$$

In order to know the total surface area of the Pyramidish interface, the total number of peaks for each model has to be calculated. Table 6.1 shows a list of models with varying frequencies in both the x and y direction, and the corresponding total number of peaks seen.

As can be seen from Table 6.1, there is a formula for the number of peaks of,

$$n = \frac{9}{4} F_x F_y \tag{6.16}$$

However, as was just discussed, for the purposes of generating the 3D plots, this can be simplified to,

$$n = \frac{9}{4} F^2 \tag{6.17}$$

Therefore, in order to calculate the total surface area of the interface, we can multiply the surface area of one peak, by the number of peaks, n,

$$\text{Pyramidish Surface Area} = \left(\left(\frac{1}{F}\right)^2 + H^2\right) \cdot \frac{9}{4} F^2 = \frac{9}{4}\left(1 + (HF)^2\right) \tag{6.18}$$

The simplification in the formula of assuming that the frequency of peaks in the x-axis, and the frequency of peaks in the y-axis, are the same had to be done in order to generate the 3D plots, shown in Figure 6.3, as there was only room for frequency of peaks along one of the three available axes.

Table 6.1: All the possible combinations of frequencies of peaks in the x and y direction, up to 5, and the resultant number of peaks that would be present in the model for the pyramidish geometry.

Fx	Fy	Whole	Half	Quarter	n
1	1	1	2	1	2.25
1	2	3	3	0	4.5
1	3	4	5	1	6.75
1	4	6	6	0	9
1	5	7	8	1	11.25
2	1	3	3	0	4.5
2	2	9	0	0	9
2	3	12	3	0	13.5
2	4	18	0	0	22.5
3	1	4	5	1	6.75
3	2	12	3	0	13.5
3	3	16	8	1	20.25
3	4	24	6	0	27
3	5	28	11	1	33.75
4	1	6	6	0	9
4	2	18	0	0	18
4	3	24	6	0	27
4	4	36	0	0	36
4	5	42	6	0	45
5	1	7	8	1	11.25
5	2	21	3	0	22.5
5	3	28	11	1	33.75
5	4	42	6	0	45
5	5	49	14	1	56.25

Similarly, to the 3D surface plots produced for the prismatic structure, Figure 6.3 shows how the resultant increase in surface area is due to increasing the frequency and height of peaks in the patterned morphology.
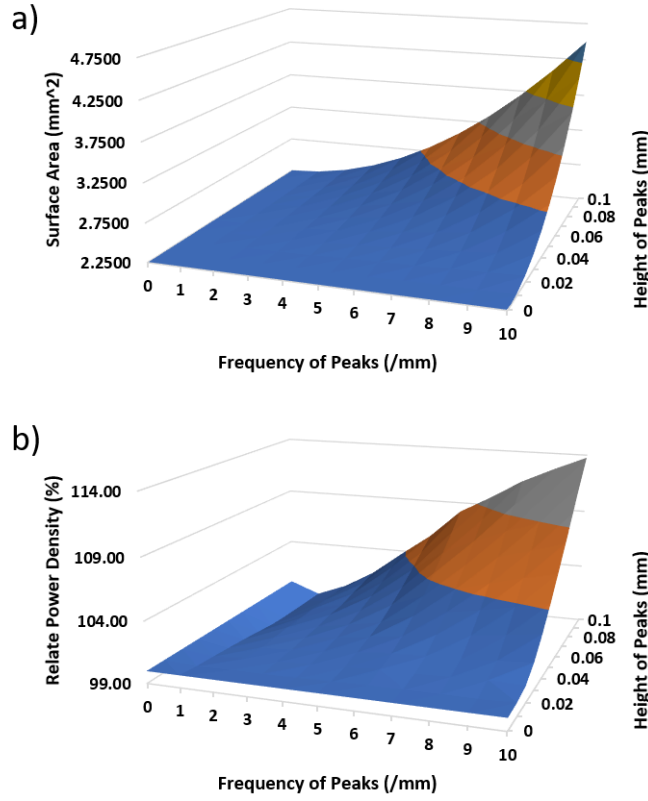
Figure 6.3: 3D Plots showing a) the impact of frequency and height of peaks on the surface area of the interface and b) the resultant power density performance relative to the planar model.

6.1.2   Data Analysis

Figure 6.4 shows how the power density of the modelled fuel cell is influenced by varying the frequency of the peaks, in both the x and y-axis, and the height of the peaks, and then how the power density compares to the planar interface.

Since there is now the y-axis that frequency can be varied in, as well as the x-axis, and given the symmetry of the model, the data curves for varying the frequency in either axis are identical to each other within a minimal percentage, so only the change of the y-axis is shown.
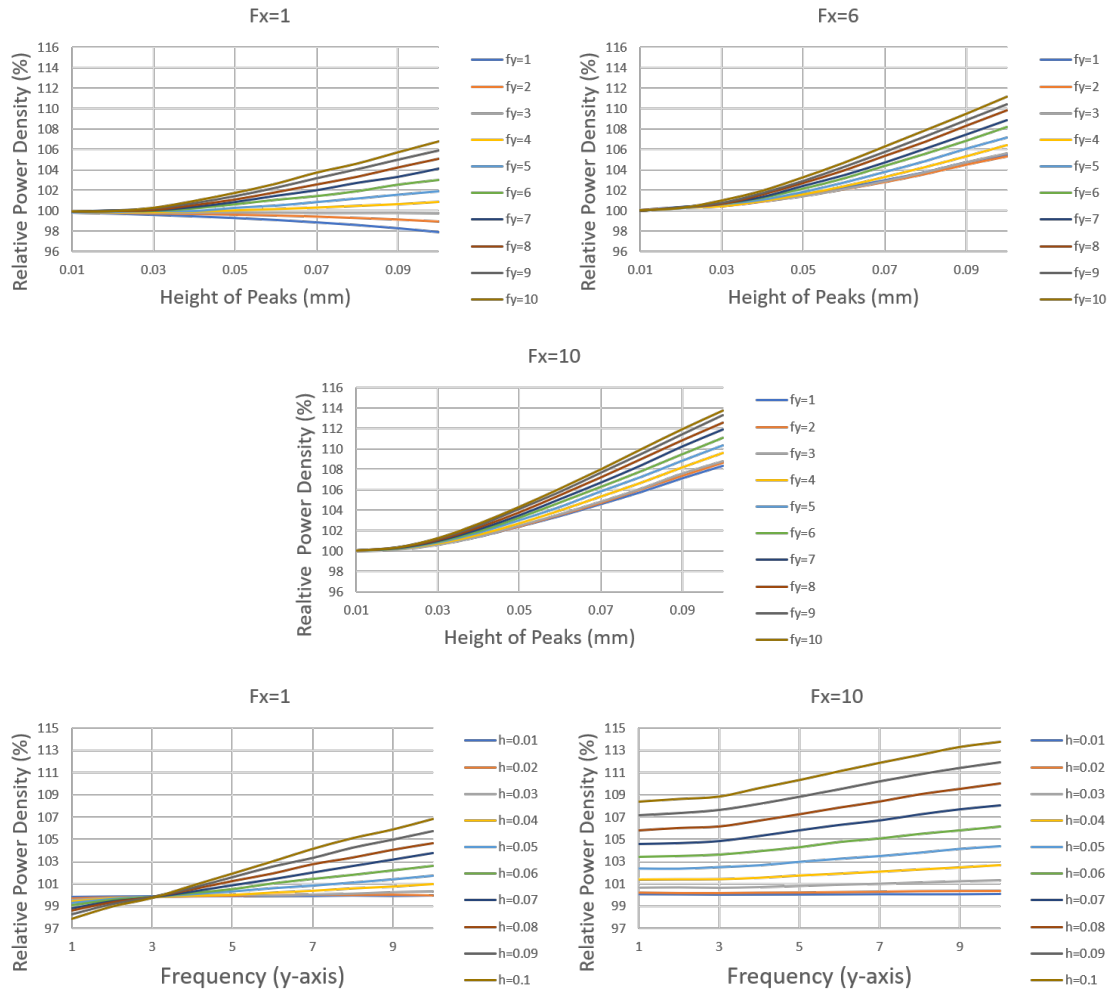
Figure 6.4: 3D Plots showing the impact of frequency and height of peaks on the surface area of the interface of the pyramidish geometry.

For clarity, since there are two different frequencies to be discussed, when referring to a graph, the constant frequency will be the primary frequency, whilst the frequency that is being varied will be regarded as the secondary frequency.

If making the argument that there is a generally positive trend between increasing the surface area and a resultant increase in power density, we would expect to see lower power density results at low peak heights and low frequencies. This argument

holds true when comparing the influence of height of peaks on power density, with the data in Figure 6.4 offering a near universal positive correlation between peak height and power density performance for frequencies above 1 or 2 peaks per millimetre, where the disruption to the interface is more detrimental than beneficial, resulting in a negative correlation between height of peaks and power density at low frequencies.

The relationship between frequency and power density offers a different way of looking at the same data and comes to the same conclusion. It can be seen there is negative correlation between frequency and power performance when both the primary and secondary frequency is very low. However, as the secondary frequency is increased, the correlation becomes positive. When the primary frequency is larger, all trends show a positive correlation between the secondary frequency and relative power density.

Another possible reason for the reduced performance seen in the lower primary frequency curves could be to do with a change in the type of flow occurring. We have already addressed that increasing the frequency and the height of the peaks will increase the surface area and thus improve the power performance. However, shifting away from the planar interface has a chance of changing the fluid flow from laminar to turbulent [199]. At the secondary frequency ranges shown where the power performance is decreasing as the frequency is increased, it could be the case that the increased surface area is over shadowed by poorer flow mechanics, until a certain frequency when the increased surface area is more dominant in determining the power density performance of the fuel cell.

Calculating Flow Type

There are three types of flow, laminar, critical and turbulent. The Reynolds number is used to establish what type of flow is occurring.

Turbulent flow means the fluid flow is continuously undergoing changes in both the magnitude and direction. For a system to have this present, a large Reynolds number of greater than 4000 is expected.

Critical flow occurs when the flow velocity is equal to the wave velocity generated by a disturbance or obstruction. This type of flow is present when the Reynolds number is between 2000 and 4000.

Fluid particles following smooth paths in layers, with little or no mixing, is characterised as laminar flow. This is often the case when the Reynolds number is less than 2000.

The Reynolds number for the planar system can be calculated using Equation 6.19,

$$Re = \frac{uL}{v} = \frac{\rho uL}{\mu} = \frac{6.67 \cdot 10^{-10}}{3 \cdot 10^{-5}} = 2.22 \cdot 10^{-5} \tag{6.19}$$

where:

ρ = density of fluid = 1 kg/m^3

μ = dynamic viscosity of liquid = 3x10^{-5} Pa/s

ν = kinetic viscosity of fluid = $2.056\text{x}10^5\text{m}^2/\text{s}$

u = flow speed = $-p \cdot perm/\mu = 200\text{Pa}\cdot1\text{x}10^{-13}\text{m}^2/3\text{x}10^{-5}\text{Pas} = 6.67\text{x}10^{-7}\text{m}^2/\text{s}$

L = characteristic linear dimension = 1000 μm (For when F=1)

with a Reynolds number of $2.22\text{x}10^{-5}$, it is clear that there is only laminar flow present.

Since the only variable that can be influenced by the patterning of the interface is L, which can only be changed in the order of a few millimetres, this is not substantial enough to increase the Reynolds number to change the fluid flow from laminar to critical or turbulent flow.

The polarisation curve for the Pyramidish model is used to compare it versus the previously analysed planar and prismatic models. Due to the increased complexity of the model design, the limit in the number of peaks that could be achieved in the structure before encountering meshing complications meant only a maximum frequency of peaks of 10 peaks per mm could be assessed. As such, when comparing against the planar and prismatic models, the frequency of peaks in the prismatic model was also reduced to 10 peaks per mm.

By comparison, using the polarisation curves of the three geometries currently analysed, it appears that similarly to the prismatic geometry, the pyramidish interface is slightly better than the planar interface within the whole current density range. However, it appears by looking at the curves, the prismatic design is superior to the

pyramidish morphology. This is backed up quantitatively as well.
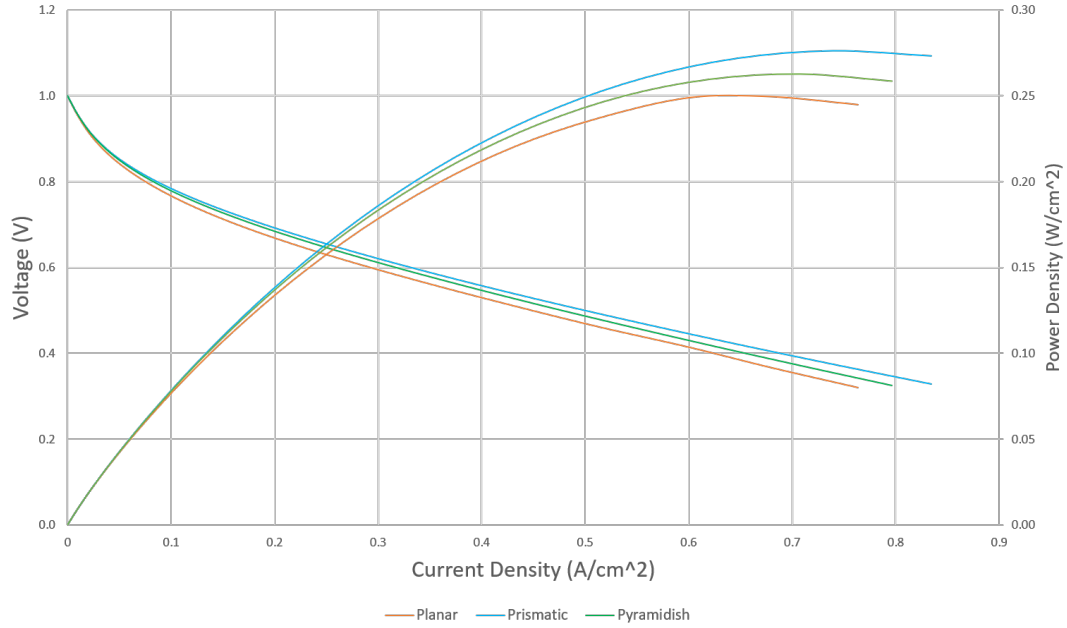
Figure 6.5: A comparison of the polarisation and power density curves of the planar, prismatic and pyramidish interfaces at a frequency of 10 peaks per mm and height of peaks of 0.1 mm.

Whilst the Prismatic structure records current densities of $0.3522 \, \text{A/cm}^2$ and 0.2037A/cm^2 at 0.6 and 0.7V respectively, equivalent to a 19.91% and 24.05% improvement in the current density compared to the results of the planar interface the Pyramidish structure yields current densities of $0.3352 \, \text{A/cm}^2$ and $0.1905 \, \text{A/cm}^2$ at 0.6 and 0.7V respectively. Similarly, the average power density of the Pyramidish interface is slightly inferior to the Prismatic geometry, but an improvement on the planar structure, at $0.152 \, \text{W/cm}^2$, compared to the $0.162 \, \text{W/cm}^2$ and $0.135 \, \text{W/cm}^2$ of the Prismatic and Planar interfaces respectively. This is also seen when observing the maximum power densities, with the $0.293 \, \text{W/cm}^2$ of the Prismatic model still performing the best, compared to $0.273 \, \text{W/cm}^2$ and $0.250 \, \text{W/cm}^2$ for the Pyramidish and Planar models respectively.

This is a surprising result, since the initial belief was the main reason behind the improvement in performance was due to the increase in active surface area of the ORR interface resulting from the interface being patterned. However, this would imply the Pyramidish geometry should outperform the Prismatic geometry given it's larger surface area, as shown in table 6.2. Therefore, there must be another mechanism taking place. It has been shown experimentally that linear patterns can improve fuel cell performance by providing preferential flow channels for water by-product, from the Oxygen Reduction, to leave the system, rather than staying on the surface of the interface and reducing the available surface area for the reaction to occur. However, as previously stated, this can not be considered given the simplicity of the model. Therefore, there must be another unknown mechanism causing these unexpected results. Further modifications to the model to make it more realistic compared to experimental rigs may help to explain this.

Table 6.2: Table quantitatively comparing how the surface area is impacted by the frequency of peaks, at a height of peaks of 0.1 mm, depending on the patterning design.

Frequency of Peaks (/mm)	Prismatic (mm^2)	Pyramidish (mm^2)
0	2.25	2.25
1	2.29	2.27
2	2.33	2.34
3	2.42	2.45
4	2.55	2.61
5	2.70	2.81
6	2.88	3.06
7	3.08	3.35
8	3.29	3.69
9	3.51	4.07
10	3.75	4.50
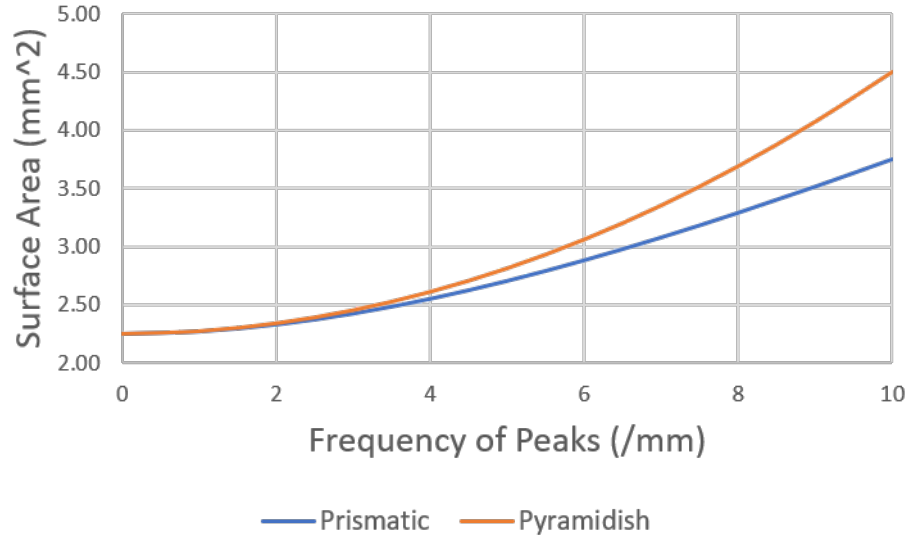
Figure 6.6: The difference in surface area of the prismatic and pyramidish geometries as frequency is increased, for a constant height of peaks of 0.1 mm.

6.2 Proper Pyramid Geometry

It has been show that having an 'almost' pyramidal structure (Pyramidish) can have a positive, but not the best, impact on the fuel cell power performance. Here, the proper pyramids, consisting of a plain base with pyramid peaks, are investigated to compare to the pyramidal structure consisting of troughs as well as peaks. Figure 6.7 shows a comparison between these two structures.
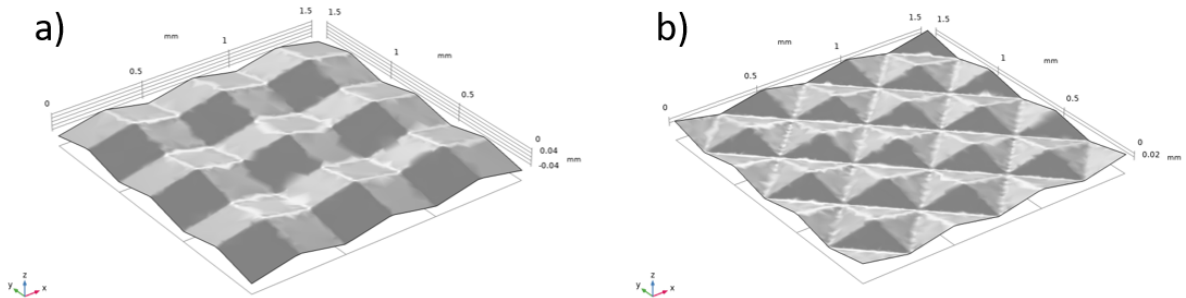
Figure 6.7: Interfaces of a) the pyramidish and b) proper pyramid structures, with a frequency of 2 peaks per mm and peak height of 0.1 mm.

In order to generate the proper pyramid geometry, the equation of the parametric surface is adjusted very slightly from the original,

$$z = -(((\text{abs}(Fx \cdot x - \text{floor}(Fx \cdot x) - 0.5) - 0.25) \cdot 2 \cdot H)$$

$$+$$

$$((\text{abs}(Fy \cdot y - \text{floor}(Fy \cdot y) - 0.5) - 0.25) \cdot 2 \cdot H) \cdot 0.5$$

to,

$$z = (\text{abs}(((\text{abs}(Fx \cdot x - \text{floor}(Fx \cdot x) - 0.5) - 0.25) \cdot 2 \cdot H)$$

$$+$$

$$((\text{abs}(Fy \cdot y - \text{floor}(Fy \cdot y) - 0.5) - 0.25) \cdot 2 \cdot H) \cdot 0.5) \qquad (6.20)$$

As can be seen, the two parametric equations are extremely similar. The only difference between them is taking the Pyramidish formula, and applying an absolute modulus function to it. This converts any negative troughs into positive peaks, creating an array of pyramids.

6.2.1   Calculating Volume and Surface Area

Maintaining a Constant Volume

As with all the previous models, the starting z-component of the parametric surface has to be calculated in order to maintain a constant volume of the membrane and catalyst layer. In the case of this structure, the discrete pyramid structures make this much simpler to calculate than with some of the previous models.

The equation for the volume of an individual pyramid, is,

$$V = \frac{lwH}{3} \tag{6.21}$$

where V is volume, l and w are the length and width of the pyramid bases, and h is the height of the pyramids.

In order to work out the volume of each pyramid in this model, we must find the relationship between l and w, with Fx and Fy.
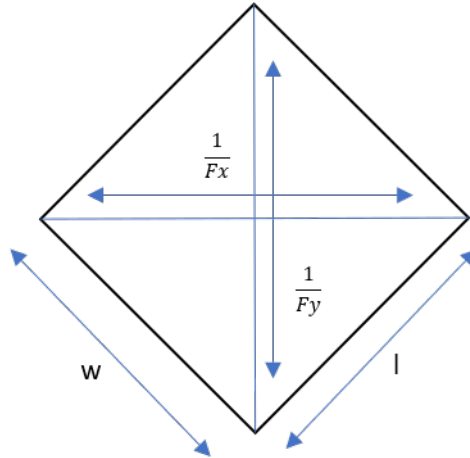
Figure 6.8: 2D view from above of the pyramid geometry.

Using trigonometry, and Pythagoras' theorem, we can determine a formula for l and w with respects to L and F.

$$l^2 + w^2 = \frac{1}{F_x^2} = \frac{1}{F_y^2} \tag{6.22}$$

For cases where Fx=Fy, this simplifies to,

$$2(l^2) = \frac{1}{F^2} \tag{6.23}$$

because l and w are the same.

Thus,

$$l = \sqrt{\frac{1}{2(F)^2}} \tag{6.24}$$

and,

$$V = \frac{H}{6F^2} \tag{6.25}$$

This is the volume of one pyramid. However, the total change in volumes of the membrane and catalyst layer are also dependent on the total number of pyramids.

By analysing the number of pyramids present at the interface for frequency sets of Fx=1-5 and Fy=1-5, a table of data could be generated, as shown in Table 6.3.

Table 6.3: The total number of pyramids presented within a $2.25mm^2$ area dependent on the frequency of peaks in both the x and y direction.

Fx	Fy	Whole	Half	Quarter	n
1	1	2	4	2	4.5
1	2	5	7	2	9
1	3	8	10	2	13.5
1	4	11	13	2	18
1	5	14	16	2	22.5
2	1	5	7	2	9
2	2	13	8	4	18
2	3	20	13	2	27
2	4	28	14	4	36
2	5	35	19	2	45
3	1	8	10	2	13.5
3	2	20	13	2	27
3	3	32	16	2	40.5
3	4	44	19	2	54
3	5	56	22	2	67.5
4	1	11	13	2	18
4	2	28	14	4	36
4	3	44	19	2	54
4	4	61	20	4	72
4	5	77	25	2	90
5	1	14	16	2	22.5
5	2	35	19	2	45
5	3	56	22	2	67.5
5	4	77	25	2	90
5	5	98	28	2	112.5

From this table, we can formulate an equation for the number of pyramids present, dependent on Fx and Fy,

$$n = \frac{9}{2}F_x F_y \tag{6.26}$$

where n is the total number of pyramids.

Since we are currently assuming Fx=Fy, this simplifies to,

$$n = \frac{9}{2}F^2 \tag{6.27}$$

Therefore, the total volume (V_T) given by the total number of pyramids can be expressed as,

$$V_T = \frac{H}{6F^2} \cdot \frac{9}{2}F^2 = \frac{3}{4}H \tag{6.28}$$

This means that the total volume given by the total number of pyramids is actually independent of the frequencies.

Using the formula for V_T, we can now calculate the required displacement of the parametric surface in the z-axis, in order to maintain constant volumes for the membrane and catalyst layer.

$$V_{clo} = L_x L_y t_c \tag{6.29}$$

$$V_{mo} = L_x L_y t_m \tag{6.30}$$

$$V_{cl} = L_x L_y t_c - \frac{3}{4}H \tag{6.31}$$

$$V_m = L_x L_y t_m + \frac{3}{4}H \tag{6.32}$$

To maintain a constant volume, the starting z-coordinate needs to be adjusted away from the origin.

$$L_x L_y t_m = L_x L_y (t_m + z) + \frac{3}{4} H \tag{6.33}$$

$$z = -\frac{3H}{4 L_x L_y} \tag{6.34}$$

The starting coordinates for the interface must shift from $(0,0,0)$ to $(0,0,-\frac{3H}{4 L_x L_y})$

Comparing Surface Area

Similarly to the previously discussed Prismatic and Pyramidish geometries, it is worth determining whether there is a similar correlation between surface area and power density, since this appears so far to be the primary cause for the observed improvement.

Calculating the surface area of the Proper Pyramid geometry is a lot easier. This is because the formula of the parametric surface that defines the surface area of the interface is actually the complete modulus of the formula used for the Pyramidish geometry. Therefore, the interfaces for the Pyramidish and the Proper Pyramid geometries have exactly the same surface areas. This means the equation for the surface area of the Proper Pyramid models is also,

$$\text{Proper Pyramidal Surface Area} = \frac{9}{4} \left(1 + (HF)^2 \right) \tag{6.35}$$
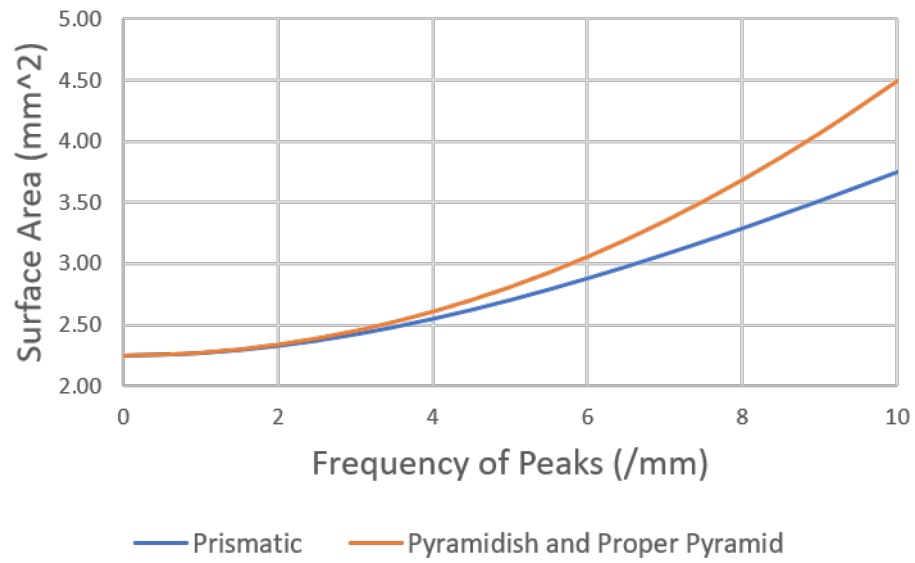
Figure 6.9: Surface area comparison between the prismatic, pyramidish and proper pyramid geometries for varying Frequencies up to 10 peaks per mm, at a peak height of 0.1 mm.

6.2.2 Data Analysis

Figure 6.10 shows what influence that changing the frequency and height of peaks has on the relative power density of the models compared to the planar model. As has been seen in all the previous models, there is a strong positive correlation between both frequency and height of peaks with resultant power performance.
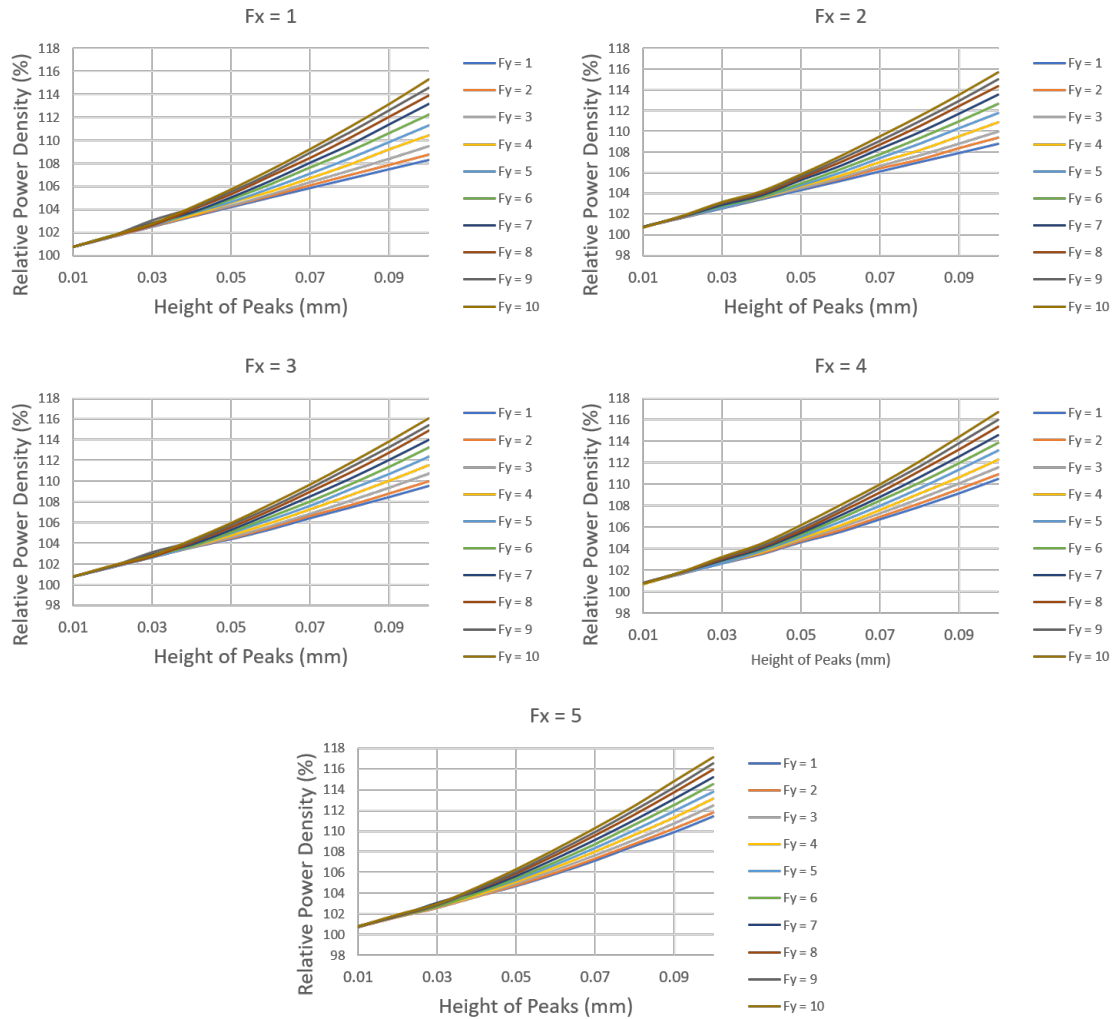
Figure 6.10: Graphs showing what influence that changing the frequency and height of peaks has on the relative power density, for the proper pyramid interface models.

Unfortunately, due to the increased complexity of the model at higher values of Fx, Fy and h, namely due to sharpness of the structure at certain points, and the resultant meshing errors, data collection for models of only up to Fx=5, Fy=5 and h=0.1 mm could be achieved.

One aspect of this pyramid structure that can be investigated was not as simple as that with the previous models. Rather than looking at the frequency of pyramids, we can see how a range of the total number of pyramids can impact relative power density.
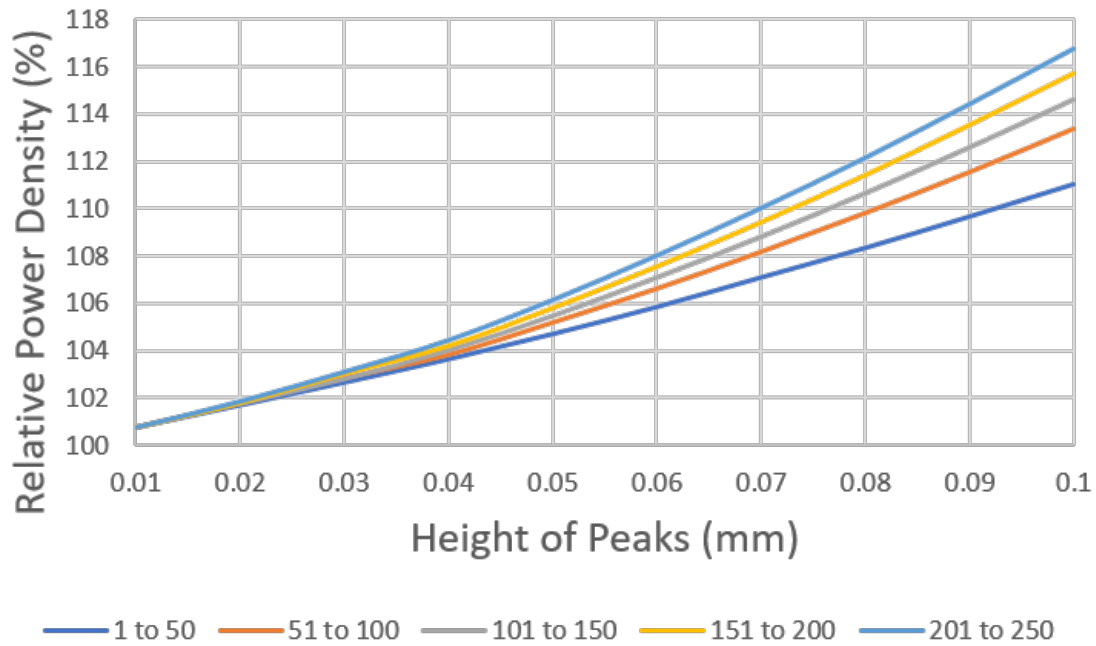
Figure 6.11: Graph showing the influence of the range of the total number of peaks on the relative power density output of the proper pyramid model compared to the planar model.

Not too surprisingly, there is a similarly positive trend between the number of pyramids and the relative power density.

Based on the understanding of the influence of increasing the frequency and height of peaks on the improvement of power performance, and considering the increase in the active surface area of the interface, here the effect is studied for the structural coordination of the pyramids on the power performance.
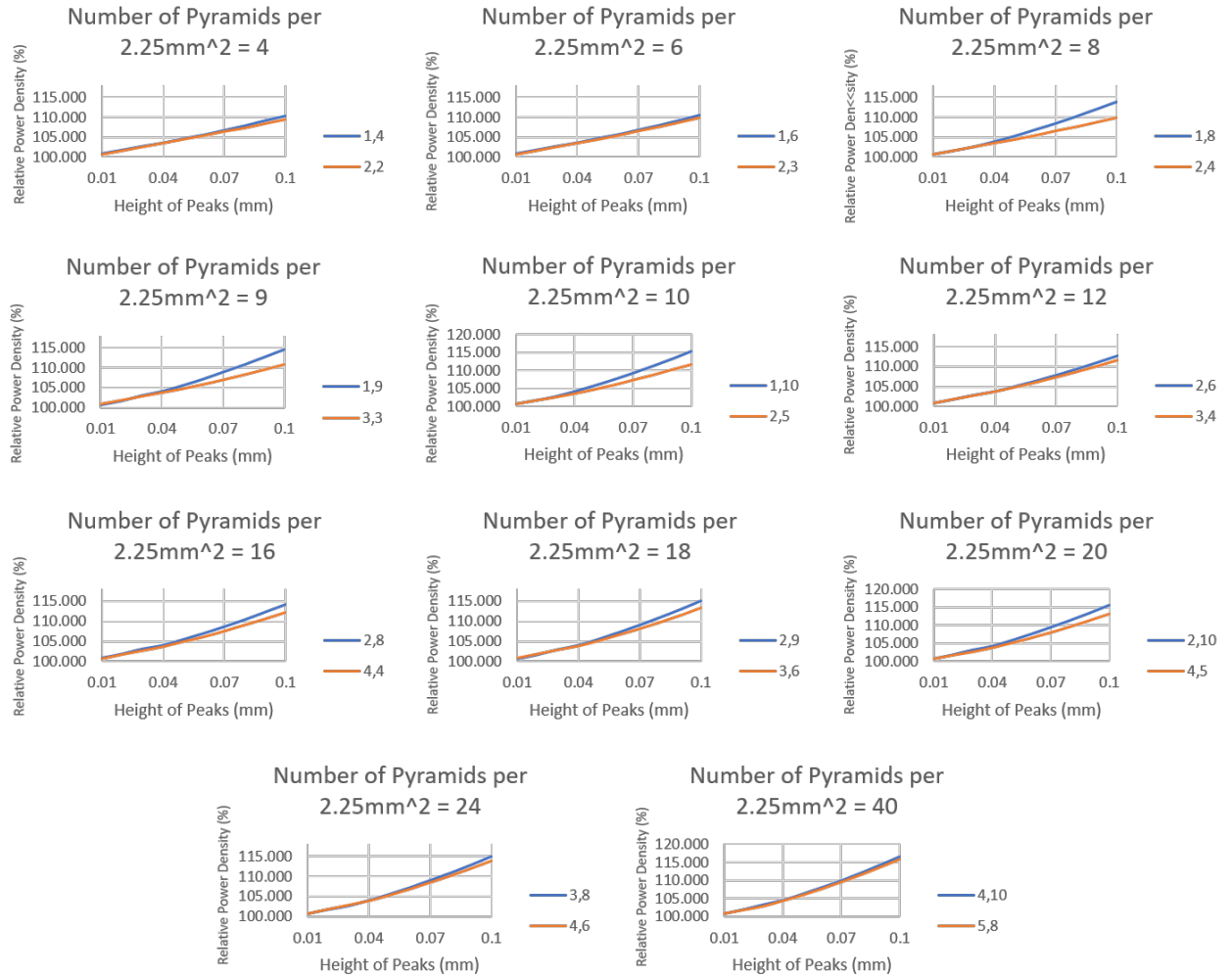
Figure 6.12: Graphs showing how pyramid distribution has an impact on power density output for the proper pyramid model. The numbers in the legends correspond to the arrangement of pyramids in the model. For example, '2,5' means a frequency of peaks in the x direction of 2 and a frequency of peaks in the y direction of 5.

Figure 6.12 shows there is a noticeable discrepancy in results based on the coordination of pyramids. If active surface area were to be the sole factor in improvement of

power density, then there should not be any difference in results depending on coordination. However, in all cases, there is a clear improvement in performance when the pyramids are coordinated in longer and narrower groups, i.e., 2 by 10, which showed a relative power density improvement of 15.68% rather than shorter and more compact groups, i.e., 4 by 5, which only showed an improvement in power density, relative to the planar model, of 13.11%. A possible explanation for this could be the same reasoning for why the prismatic interfaces have so far outperformed the other structures, given the longer and narrower grouped coordinated pyramids would have a structure more similar to the prismatic structure. However, as previously stated, the simplicity of the model makes it hard to understand the mechanism causing this.
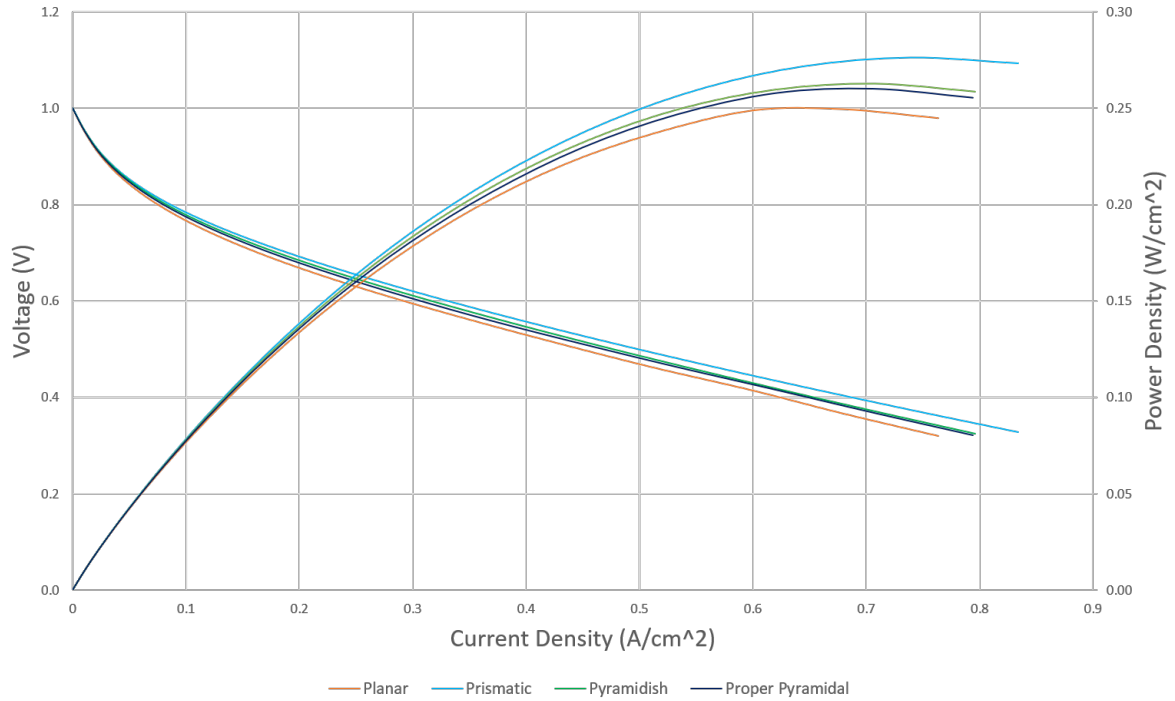
Figure 6.13: Collection of polarisation and power density curves comparing the performance of the planar, prismatic, pyramidish and proper pyramid interfaces with a frequency of peaks of 6 peaks per mm, at a height of 0.1 mm.

It is not too surprising that, given the Proper Pyramidal and the Pyramidish geometries have identical surface area profiles, they have very similar polarisation curves. As discussed in section 6.1, there is potentially an unknown second mechanism in play, which is the most likely reason why the two polarisation curves are not identical. The orientation of the pyramids used for creating the polarisation curve shown in Figure 6.13 was a 6 by 6 structure. Given the results and analysis from Figure 6.12, it would be expected that using an arrangements of pyramids of 12 by 3 would result in a superior polarisation curve.

Given the prismatic interface is still the best of the current geometries in terms of power performance, despite having the smallest surface area profile of the three patterned geometries, it would suggest that the second unknown mechanism has a larger influence on power performance than surface area does.

6.3 Waves

So far, the two observed pattern morphologies, prismatic and pyramidish, have both focused on the use of sharp, defined edges which form prisms and pyramids respectively. It may be seen that the extremities of these edges were the possible reason leading to errors in the models at these points.

As such, an alternative to patterned morphologies are then generated from an origin of such structures to be explored. Rather than working from prisms or pyramids, the morphology is created based on sine waves to understand its influence on the power density performance.

By applying the below equation to the catalyst-membrane interface,

$$z = (sin(2\pi F_x x)) + (sin(2\pi F_y y)) \cdot \frac{H}{2} \tag{6.36}$$

A basic sine wave is built in both the x and y-directions, and the structures such as is shown in 6.14.
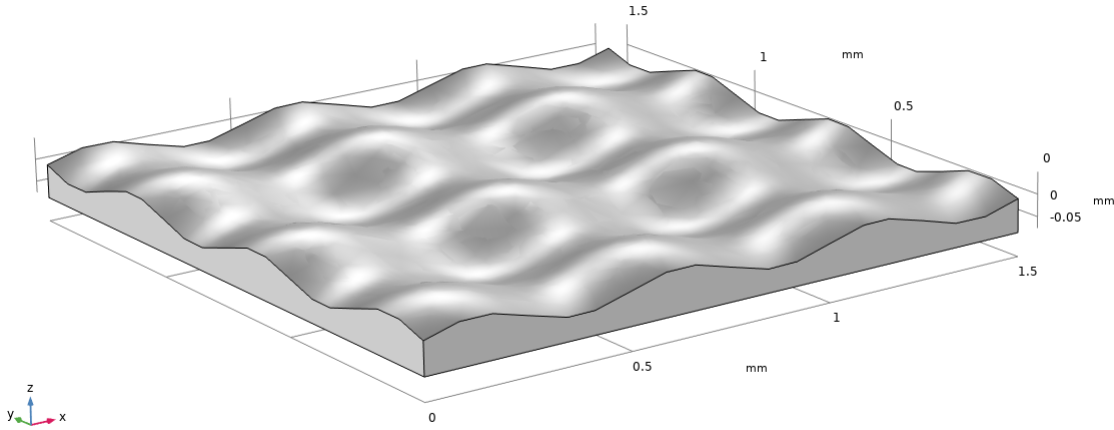
Figure 6.14: Image of the waves model with frequency of peaks in the x and y-direction of 2 peaks per mm, and an amplitude of 0.05 mm.

Similar to the previously discussed pyramidish structure, since there are parameters in both the x and y directions, there are three variables in play. However, with this Waves geometry, we are not dealing with peaks, but rather sine waves. As such, the variables are the frequency of waves in the x-axis and y-axis, and rather than height of peaks, we are monitoring the amplitude of the sine waves.

As with previous models, it is important to keep a constant volume of the membrane and catalyst layer. Whereas in previous models, this could be done by calculating

how the height and frequency of the peaks impacted these volumes, and thus, calculating how much to adjust the z-coordinate of the parametric surface that is used to build the interface, but it is much more difficult to do this for a geometry built from sine waves. This is because whereas the previous interfaces were generated by equations that created straight line curves, such as the zigzag structure of a prismatic morphology, the curved nature of trigonometric curves makes this very difficult. Even more so in three dimensions. The amplitude of the sine waves is not an issue, since any increase in volume by the size of the peaks is cancelled out by the equal decrease in volume due to the size of the troughs. However, this is an issue when dealing with the frequency, since this can lead to the total volume above and below the neutral line (z=0) not being equal. However, there is a way around this. Since the geometry of the model is bound to a region that is 1.5 mm by 1.5 mm, this means as long as the frequency of peaks is a multiple of two, this will lead to all sine waves being fully completed at the extremes of the model, resulting in a conservation of the volumes.

A schematic in Figure 6.15 is included to demonstrate this.
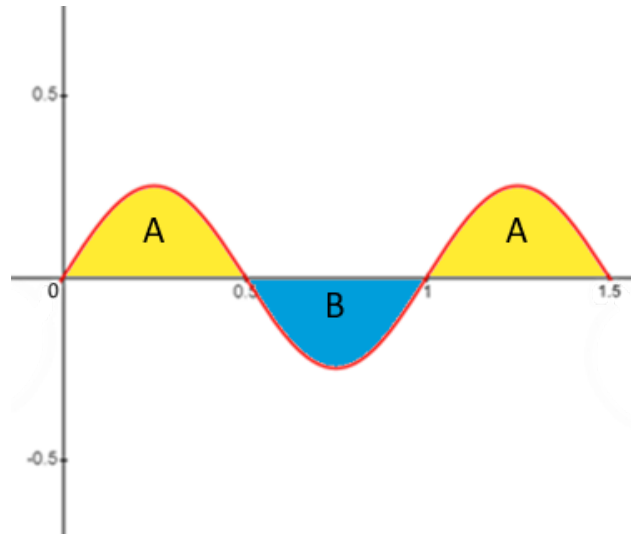
Figure 6.15: Sine wave showing the area of $A \neq B$ when $F = 2n + 1$.

For sine waves where F=2n+1, where n is an integer, the total area (and volumes when in three dimensions) of area 'A' $\neq$ the total area of area 'B'
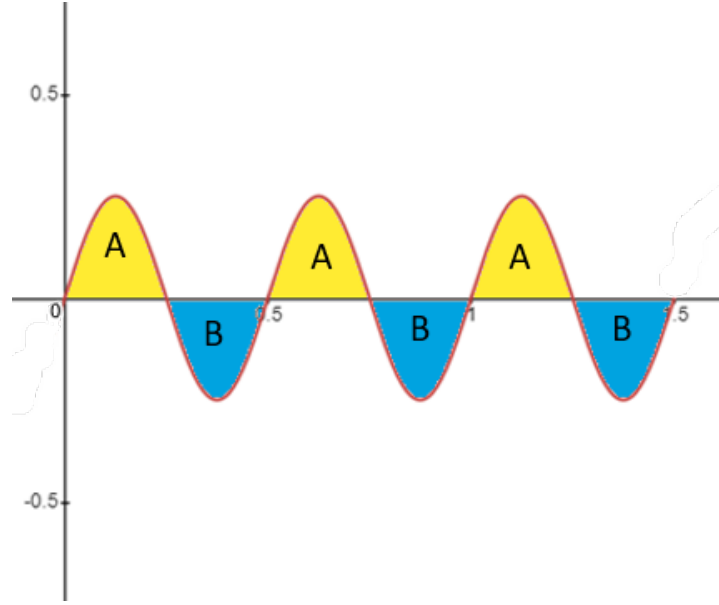
Figure 6.16: Sine wave showing the area of $A = B$ when $F = 2n$.

For sine waves where F=2n, where n is an integer, the total area (and volumes when in three dimensions) of area 'A' = the total area of area 'B'.

Therefore, as long as the models that are studied only include geometries consisting of frequencies of multiples of two, i.e., F=2,4,6,8,10, then, in order to maintain a constant volume for the membrane and catalyst layer, the starting height of the z-component of the interface can be set to 0.

As with the Pyramidish model, Figure 6.17 shows a uniformity between the power density results, irrespective of whether we focus on the frequency of peaks in the x-axis or in the y-axis.
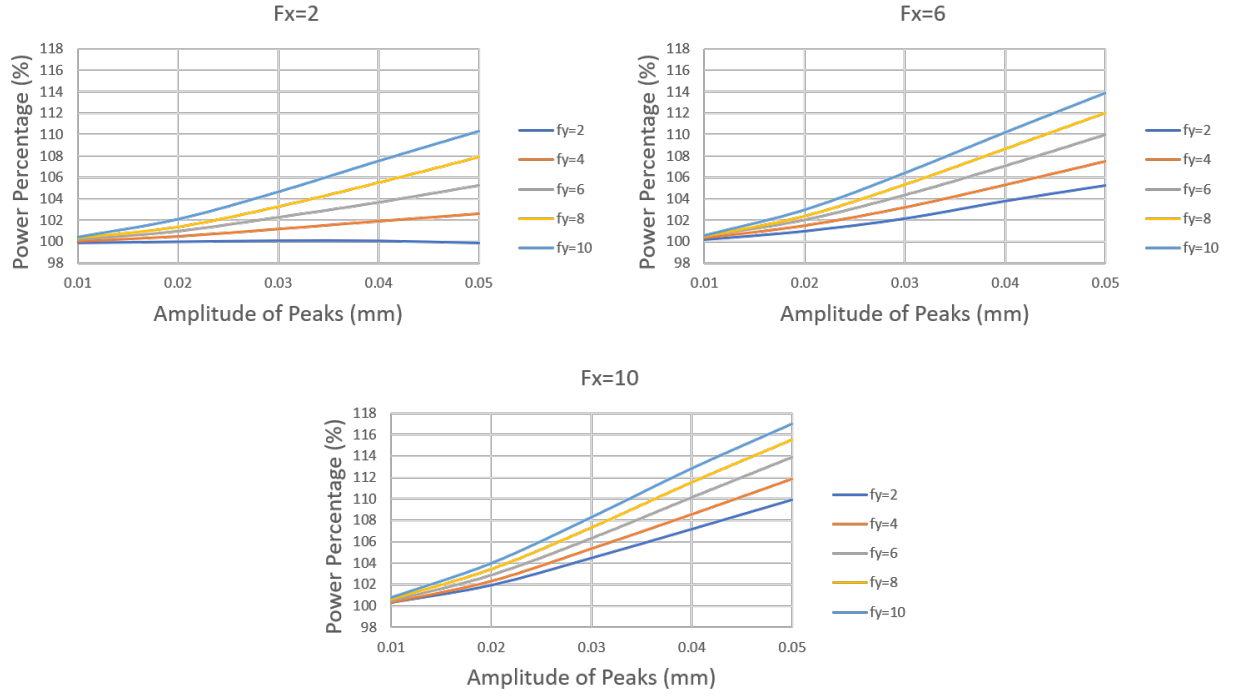
Figure 6.17: The influence of the frequency and amplitude of waves on the relative power density output, for the waves geometry, compared to the planar model.

Similarly to the previous models, the reasoning for the improved performance is believed to be due to the increased active surface area due to the patterned morphology.

Calculating how the surface area is influenced by the changes in the height and frequency of peaks is much more difficult than that with previous models, but can be described using the equations below.

$$z(x,y) = \frac{H}{2}\bigg(sin\big(2\pi F_x x\big) + sin\big(2\pi F_y y\big)\bigg) \tag{6.37}$$

$$A = \int\int \sqrt{1 + \left(\frac{dz}{dx}\right)^2 + \left(\frac{dz}{dy}\right)^2}\, dxdy \tag{6.38}$$

$$A = \int_{0}^{L_y} \int_{0}^{L_x} \sqrt{1 + \left(H\pi F_x cos\left(2\pi F_x x\right)\right)^2 + \left(H\pi F_y cos\left(2\pi F_y y\right)\right)^2} dxdy \qquad (6.39)$$

This double integral equation is too difficult to be solved manually. However, surface areas of individual sets of parameters can be calculated using a Matlab script.

This allows us to generate a 3D Surface Area, similar to those in previous chapters, with a corresponding 3D plot showing the influence of the amplitude and frequency of peaks on power density relative to the original planar model.
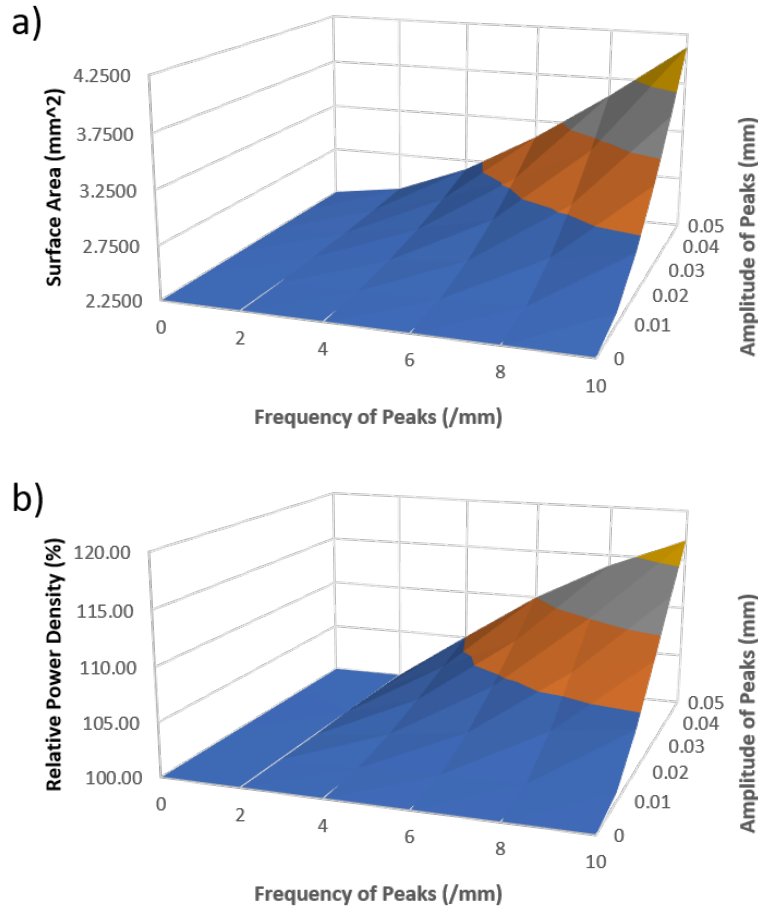
Figure 6.18: 3D Plots showing a) how the amplitude and frequency of peaks influences the total surface area of the interface, and b) how that also impacts the power density output relative to the planar model.

Figure 6.18 shows a very similar profile to the results seen for the prismatic model in Figure 5.9, with a clear positive correlation between the surface area and the power density output, with the impact of increasing the surface area on the power density becoming less significant at higher surface areas, suggesting a similar plateauing situation to what has been discussed.
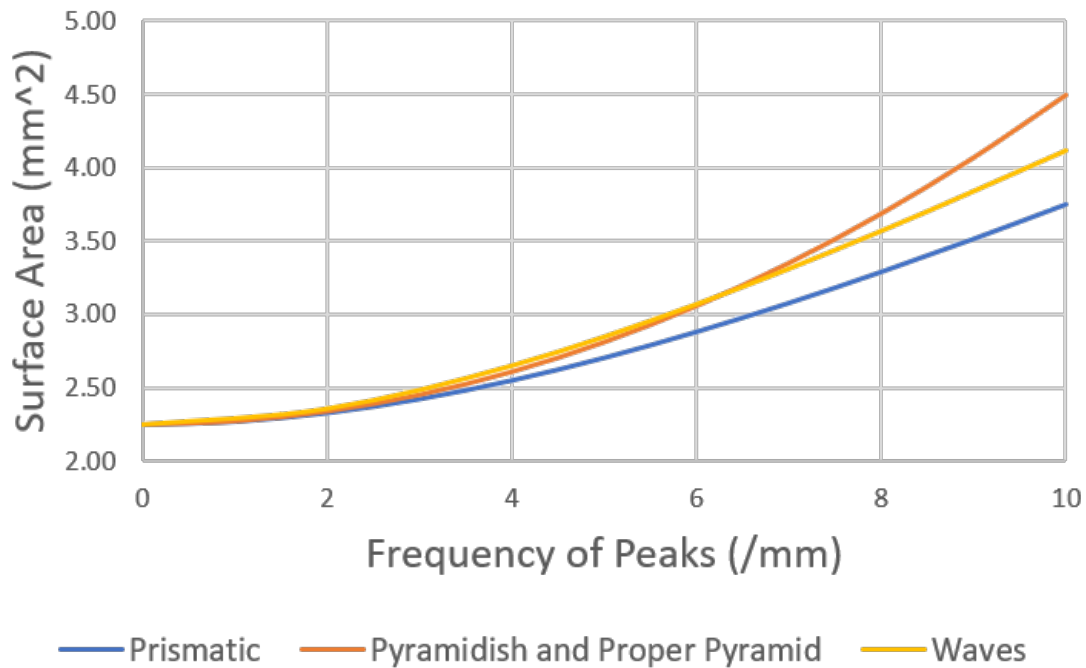
Figure 6.19: Surface area comparison between the prismatic, pyramidish, proper pyramid and waves geometries for varying frequencies up to 10 peaks per mm, at a peak height of 0.1 mm.

Figure 6.19 shows that the waves morphology fits between the prismatic, and the two pyramid-style geometries, in terms of surface area profiles. Again, it is worth noting that although the surface area of the waves morphology provides a larger total surface area for the same equivalent parameters for height and frequency of peaks, the power density output is still greater for the prismatic interface, as shown in Figure 6.20. As previously discussed, the superior performance observed by the prismatic geometry

is likely to be due to the prismatic structure benefiting an unknown mechanism more significantly than is seen for the other geometries. The waves geometry outperforms the pyramidish and proper pyramidal geometries. It is believed that the performance is better for the waves morphology because the unknown second mechanism is more impactful for the wave geometry compared to the pyramid styled geometries.
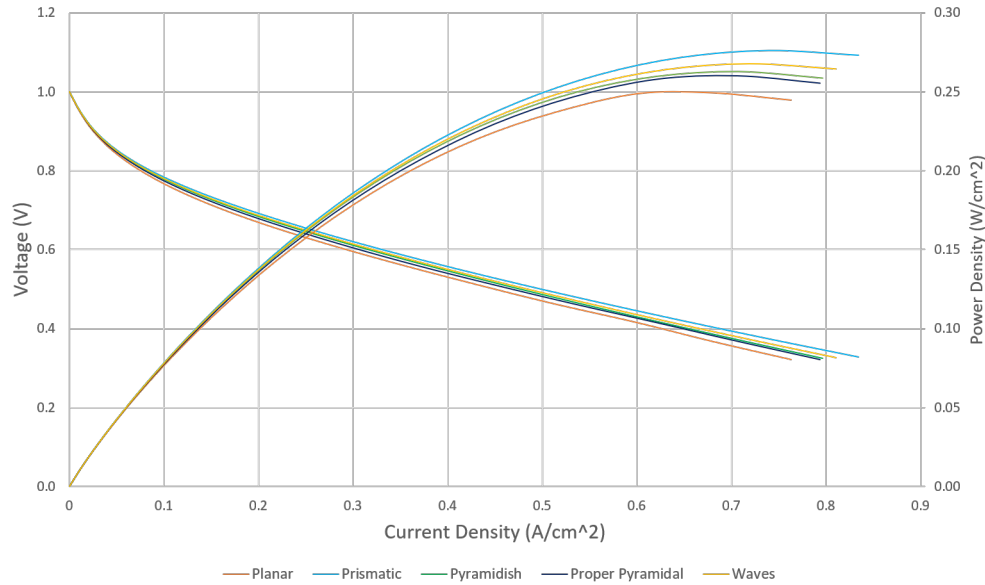
Figure 6.20: Polarisation curves and power density curves of the planar, prismatic, pyramidish, proper pyramidal and waves geometries, each with a frequency of peaks of six peaks per mm, at a peak height of 0.1 mm.

6.3.1 Phase Shift

Although not much additional information can be observed from this geometry, other than the already discussed benefits of increasing the surface area, and how this improves the power density of the fuel cell, there is one possible route of study that can be taken that could be interesting. So far, the results collected for the new waves geometry have all been from standard sine waves. However, how would the output results vary, if a phase shift is applied to the sine waves, as shown in Figure 6.21,

where the red curve is a function of $y = sin\theta$, whilst the black curve is the original $y = sin\theta$ curve, with a phase shift of 60°. Whilst this will not result in any changes to the respective volumes of the membrane or catalyst layers, and the total surface area will also remain the same, there could be a change in the output power density due to the change in the interface morphology with respect to the region of oxygen inlet/water outlet of the model.
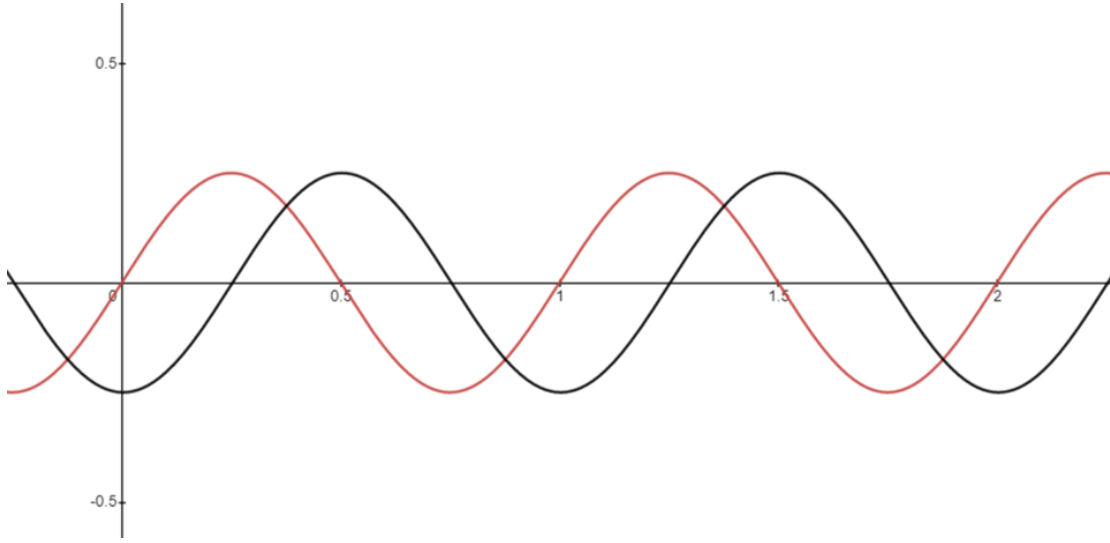
Figure 6.21: x-y Chart showing the difference in surface morphology between a geometry governed by sineθ and the same geometry with a 60° Phase Shift applied.

To allow for the application of a phase shift to the sine waves presented within the morphology, the z-coordinate of the parametric surface had to be updated from,

$$z = (sin(2\pi F_x x) + sin(2\pi F_y y)) * \frac{H}{2} \tag{6.40}$$

to,

$$z = (sin(2\pi F_x(x+(PS \cdot \frac{\pi}{180})) + sin(2\pi F_y(y+(PS \cdot \frac{\pi}{180}))) * \frac{H}{2} \tag{6.41}$$

where PS is the phase shift in degrees.

Phase Shift analysis are carried out for frequencies of 2,4,6 and 8, with amplitudes of 0.01, 0.03 and 0.05mm. The results are shown in Figure 6.22.
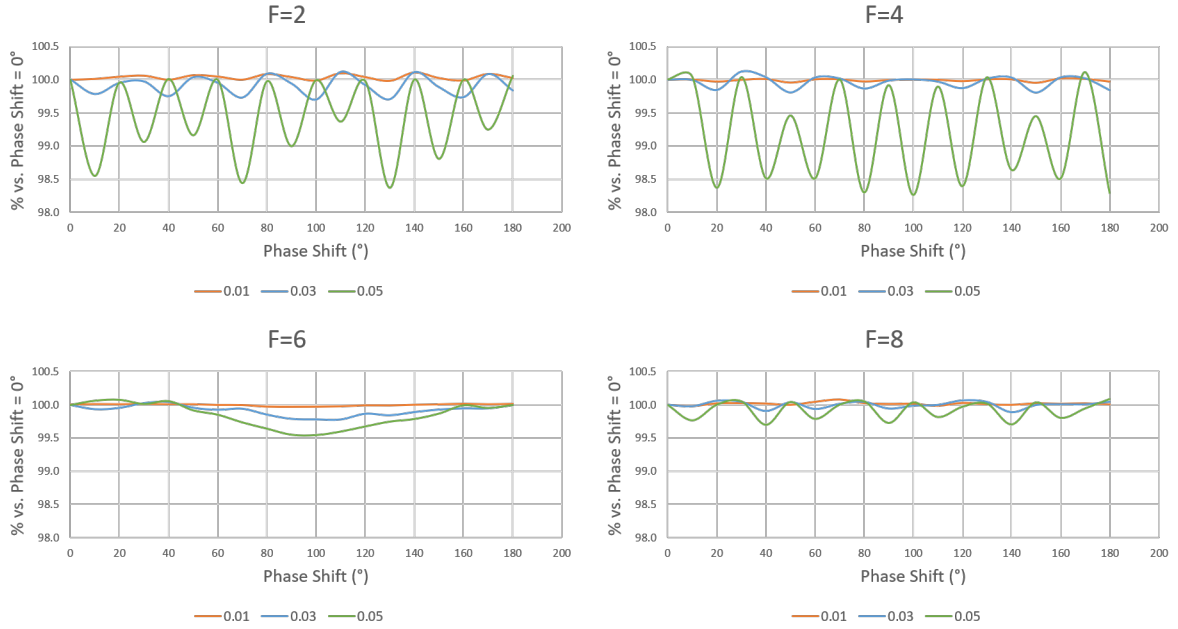
Figure 6.22: Graphs showing the influence of phase shift on power density depending on frequency and height of peaks, for the waves geometry.

Before running the experiment, it was expected that applying a phase shift had no impact on the total surface area of the interface, thus there would be little to no resultant change in the power density. However, there is a clear fluctuation in output. Noticeably, the results can be grouped together dependent on whether the phase shift can be defined as,

either,

$$\text{Phase Shift} = 20° + n$$

or,

$$\text{Phase Shift} = (20° + n) + 10° \tag{6.42}$$

where n is a positive integer.

This noticeable variation in results is more apparent at larger amplitudes and small frequencies. Both of these observations are logical, given the variations are expected to be more significant at larger amplitudes, where the total surface area is larger, and the distance between the peaks and troughs is more noticeable. The variance in results being more noticeable at lower frequencies is because when there are fewer peaks, any shift in the structure of the sine waves in comparison to the position of the oxygen inlet will be more apparent. The shift in the structure is a lot less significant when there is a larger frequency, where any phase shift has a lesser impact on the resultant morphology of the interface.

This can be seen for the 0.05 mm curves. Although not completely flattened out, the fluctuating variation in the power density output due to a shift in phase is significantly less at higher frequencies.

One aspect of Figure 6.22 that has not been mentioned is the difference in varying performance with phase shift specifically for when the frequency is two peaks per mm. Whereas the high frequencies demonstrate an alternation in performance, as stated in Equation 6.3.1, at this frequency, there are four variations in performance. The reasoning for this would be due to the impact of having such few peaks present in the structure. At a frequency of two peaks per mm, a 2.25 mm^2 geometry would only have the equivalent of nine peaks, compared to 144 peaks when the frequency of

peaks is 8 peaks per mm. This means that for F=2, not only will any phase shift have a bigger difference on performance than for at higher frequencies, but there could be more variations in the geometry relative to the oxygen inlet/water outlet, resulting in more performance variations depending on the scale of the phase shift.

Therefore, depending on the frequency of peaks used, whether inclusion of a phase shift is worth looking into or not is determined. At low frequencies, there appears to be a fluctuation in performance dependent on the frequency of peaks. At higher frequencies, there does not appear to be any significant change. However, the power density output is larger at higher frequencies, regardless of whether there is a phase shift or not, meaning there is very little benefit in applying a phase shift to experiment geometries moving forward.

6.4   Conclusions

In chapter 5, a progression in the model was made as the complexity of the cathode/electrolyte interface was patterned with a Prismatic morphology, resulting in an improvement in power performance. In this chapter, developments were made to see how the power performance was impacted by patterning with three other geometries including: Pyramidish, Proper Pyramid and Waves geometries. As opposed to the prismatic interface, which can be considered as an extrusion of a 2D geometry, these three structures all shared 3D geometric properties, making them more complex.

Generating the pyramidish interface required using the equation for the prismatic interface, and applying it in both the x and y directions. It had been hoped that this would result in an array of pyramids, however, although there was a resultant

array of peaks, not all the valleys were at the same height, which complicated the surface area and volume calculations. When comparing the relative power density output compared to the planar model, the 3D plots are very similar in appearance to the prismatic structure, with an initial drop in performance at very low frequencies, followed by a noticeable improvement, which appears to be plateauing as surface area increases. However, although the surface area of the pyramidish geometry is larger than the prismatic geometry, providing they both have the same peak frequency and height, the prismatic structure still shows better performance. This can be seen both in the 3D plots, and the polarisation and power density curves, where quantitative results show current densities of 0.3353 A/cm^2 and 0.1905 A/cm^2 at 0.6 and 0.7 V respectively for the Pyramidish interface, compared to 0.3522 A/cm^2 and 0.2037 A/cm^2 for the prismatic interface. This is also seen in the maximum power density figures, of 0.152 W/cm^2 and 0.162 W/cm^2 for the pyramidish and prismatic structures respectively. It is believed therefore that there is an additional mechanism in play that is causing this superior performance in the prismatic interface. One strongly supported argument is that the nature of the prismatic interface is that it provides preferential flow channels for the produced water to escape from the surface of the interface, resulting in a larger active surface area to be retained than in the pyramidish structure. However, given the simplicity of the model, this can not be considered, suggesting there must be a second unknown mechanism which is responsible for the results observed.

The third geometry observed was the proper pyramid interface. This structure is very similar to the pyramidish structure and both have exactly the same surface area profile, given the equation for the proper pyramid interface is the absolute modulus of the pyramidish interface equation. It was expected that the performance of the

pyramidish and proper pyramid interfaces would be extremely similar. Besides being a little lower in terms of power performance, which is believed to be due to the unknown mechanism, this was true. There is an, as expected, improvement in performance as the number of pyramids in the model is increased, since this correlates with an increase in the frequency of peaks, and resultant increase in surface area. Similarly to other geometries, the rate of increase in the performance, as the number of pyramids is increased, decreases as the increase in power density with respect to surface area begins to plateau. More interestingly is the relationship between performance, and the orientation of the pyramids. The result also showed a universal improvement in power density when the pyramids were orientated with long rows of pyramids, rather than blocks of pyramids. A numerical example of this is a 15.68% improvement in relative power density compared to the planar model, for a pyramid arrangement of 2 by 10, compared to an arrangement of 4 by 5 pyramids which only saw an improvement of 13.11%. This is believed to be again related to the improvements seen in the prismatic geometry due to the unknown second mechanism, since the former arrangement offers longer flow channels similar to the prismatic geometries.

The final unique interface observed was the waves geometry, which differs from the previous interfaces because it is governed by sine waves, rather than a mathematically calculated formula. The benefit of a geometry that revolves around trigonometric waves, is that, as long as there is a whole number of completed waves in the interface, the volume above and below the $z = 0$ interface will be equal. However, calculating the surface area of a trigonometric interface is very complicated, and the 3D plots showed a very similar profile to the other models. However, although the surface area is slightly lower than the calculated surface area of the pyramidish and proper pyramid geometries, the performance was slightly better for the waves interface. A

belief for this is that whereas the waves structure is very rounded, due to the nature of trigonometric waves, the pyramidish and proper pyramid structures consist of sharp edges, where the water flow may be disrupted. An analysis of the impact of applying a phase shift to the waves interface was also assessed. It was found that applying a phase shift caused a change in performance, that fluctuated back and forth depending on whether the Phase Shift $= 20° \cdot n$ or Phase Shift $= (20° \cdot n) + 10°$. This change in performance was more impactful at lower frequencies, where the shift in the interface with respect to the oxygen inlet/water outlet was more noticeable. Additionally, at very low frequencies, there were more than just the two performance ranges. This is due to there being fewer peaks, so there are more phase shift ranges that result in unique interface morphologies relative to the reactant oxygen gas inlet/water outlet.
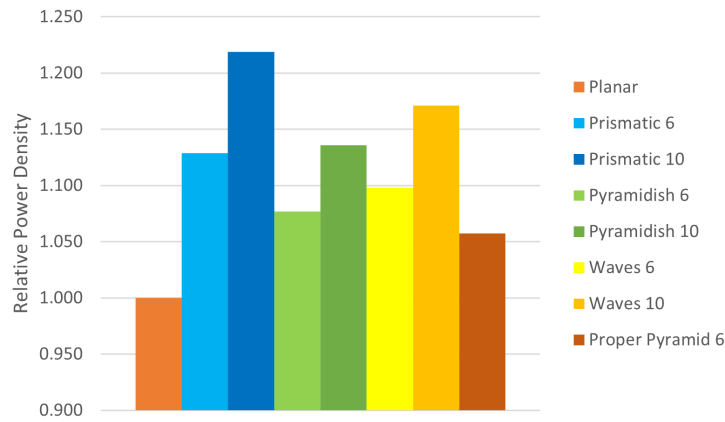
Figure 6.23: Bar chart comparing the best power density outputs of all the studies geometries with a peak height of 0.1 mm, compared to the planar interface.

Figures 6.23 and 6.24 show a side-by-side comparison for the maximum power density values recorded from their respectively polarisation curves for the different interfaces. The prismatic geometry appears to show the best performance, despite having the lowest surface area out of the patterned interfaces. This was initially believed to

be due to the benefits of the flow channels for water to leave the system, which the other geometries don't benefit so strongly from, although the lack of a GDL makes it difficult to make this claim. Therefore, moving forward, it would be suggested that applying a pattern to the cathode catalyst layer-electrolyte interface with a prismatic geometry would be recommended.
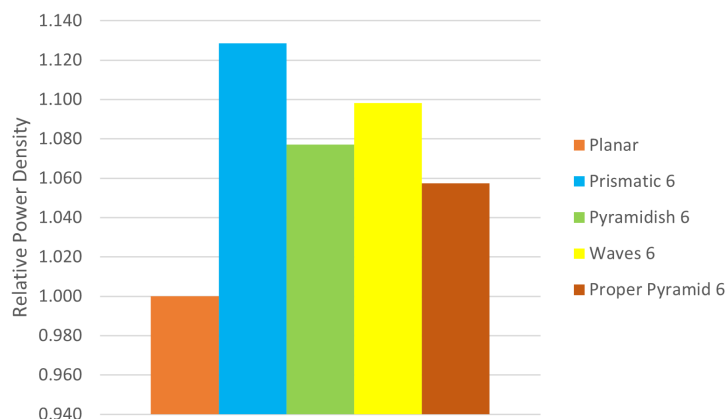
Figure 6.24: Bar chart comparing the best power density outputs of the Studies geometries, specifically with a frequency of six peaks per mm and peak height of 0.1 mm, compared to the planar interface.

Figure 6.25 shows a graph comparing the performance of the different patterned interfaces with one another. The results compliment the conclusions of Figure 6.24, showing the geometry hierarchy, in terms of performance, having prismatic at the top, followed by waves, pyramidish, proper pyramid and lastly the planar geometry.

Fabrication of the patterned membranes would likely result in some defects in the membrane, which would lead to poorer results than have been simulated, but given there was a 22% improvement seen in the prismatic interface with a frequency of peaks of 10 peaks per mm at a height of 0.1 mm, as shown in Figure 6.23, there is a good amount of 'wiggle room' where there could still be a positive gain in power performance.
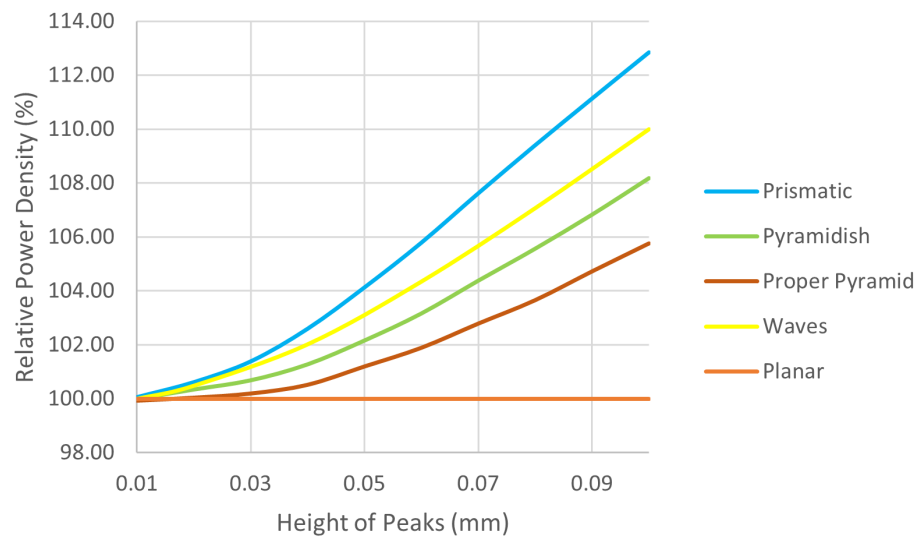
Figure 6.25: Graph comparing the performance of the different patterned interfaces with one another, as the height of the peaks is increased from 0.01 mm to 0.1 mm, at a constant frequency of 6 peaks per mm.

Chapter 7

Applying Roughness to the Interface

Whilst the current results from the patterned interface designs show promise of improved power performance, these models are unrealistic given that the interfaces consist of perfect planes between the membrane and catalyst layer. It is well understood that in reality, these interfaces would have some degree of roughness associated to them. Therefore, to make these models more in line with real life MEAs, applying roughness to the interfaces is investigated in this chapter, and an assessment is carried out to understand how this impacts the simulated results.

7.1   Characterising Roughness

Before applying a roughness to the morphology of the interface, it is important to characterize surface roughness.

An approach for characterizing roughness is through spatial frequency content, which builds roughness in a surface by using a constructive method of synthesizing surface data by using sums of trigonometric functions similar to a Fourier series expansion,

where a certain frequency of oscillation through space is represented by each term of the series. This method is used in this model.

7.1.1 Spatial Frequencies

Frequencies of oscillations over time are expressed by,

$$cos(2\pi f t)$$

However, in space, this function changes to,

$$cos(2\pi \nu x)$$

Where the time variable, 't', is replaced by the spatial variable, 'x', and the time frequency, 'f', is replaced by the spatial frequency, 'ν'.

For simplicity, spatial frequencies are often represented by a wave number, 'k', where

$$k = 2\pi\nu = \frac{2\pi}{\lambda} \tag{7.1}$$

where λ is the wavelength.

Since the interface is two-dimensional in space, there will be multiple spatial frequencies, such as:

$$cos\left(2\pi(\nu_x x + \nu_y y)\right) = cos(\mathbf{k} \cdot \mathbf{x}) \tag{7.2}$$

Where the wave vector $\mathbf{k} = (k_x, k_y) = (2\pi\nu_x, 2\pi\nu_y)$ and $\mathbf{x} = (\mathbf{x,y})$

7.1.2   Elementary Waves

A rough surface can be seen as being composed of elementary waves of the following form:

$$cos(\mathbf{k} \cdot \mathbf{x} + \varphi)$$

where φ is a phase angle.

For a completely random surface, the value of φ can be anything in the interval of, for example,

$$0 \leq \varphi \leq \pi \ or \ -\frac{\pi}{2} \leq \varphi \leq \frac{\pi}{2}$$

φ can be picked from a uniform random distribution in an interval of length π, so that can then allow the expression $cos(\varphi)$ to range between -1 and 1.

By only allowing a discrete set of spatial frequencies, ν_x and ν_y, we get an efficient representation that can be used for simulations, where

$$\nu_x = m \tag{7.3}$$

$$\nu_y = n \tag{7.4}$$

where m and n are integers.

In this way, we can build a surface composed of elementary waves in the following form,

$$cos(k_{mn} \cdot x + \varphi) = cos(2\pi(mx + ny) + \varphi), k_{mn} = 2\pi(m, n) \tag{7.5}$$

A high-frequency cut-off can be determined by allowing the spatial frequencies, m and n, to take values up to maximum integers, M and N, such that:

$$\nu_{xmax} = M \qquad (7.6) \qquad\qquad \nu_{ymax} = N \qquad (7.7)$$

Similarly, the negative cut-off would be:

$$\nu_{xmin} = -M \qquad (7.8) \qquad\qquad \nu_{ymin} = -N \qquad (7.9)$$

With regards to wavelength, having a spatial frequency cut-off at $\nu_{xmax} = M$ in the x direction means that $\lambda_{xmin} = \frac{1}{M}$ can be used to represent the shortest wavelength. Similarly for the y direction, the shortest wavelength is $\lambda_{ymin} = \frac{1}{N}$.

Each elementary wave has an associated amplitude, so the current formula is updated to:

$$A_{mn}cos(\mathbf{k} \cdot \mathbf{x} + \varphi) \qquad (7.10)$$

And the summation of all the wave components can be expressed as:

$$\sum_{m,n} A_{mn}cos(\mathbf{k} \cdot \mathbf{x} + \varphi) \qquad (7.11)$$

The simplest approach for choosing the amplitude would be to choose the coefficients A_{mn} from a uniform or Gaussian distribution. However, in nature, due to processes such as erosion and wearing, it is more likely that slow oscillations have a larger amplitude than fast ones, meaning this approach is not ideal since it will not generate particularly natural-looking surfaces. This corresponds to amplitudes tapering off

according to:

$$A_{mn} = a(m,n) \sim h(m,n) = \frac{1}{|m^2 + n^2|^\beta} = \frac{1}{(m^2 + n^2)^{\frac{\beta}{2}}} \qquad (7.12)$$

Where β is the spatial exponent which indicates how quickly higher frequencies are attenuated.

$$a(m,n) = g(m,n)h(m,n) \qquad (7.13)$$

A function 'u' with a uniform random distribution between $-\pi/2$ and $\pi/2$ is used to sample the phase angles φ,

$$\varphi(m,n) = u(m,n) \qquad (7.14)$$

A double sum is used to represent the rough surface,

$$\sum_{m=-M}^{M} \sum_{n=-N}^{N} a(m,n)cos(2\pi(mx + ny) + \varphi(m,n)) \qquad (7.15)$$

where x and y are spatial coordinates; m and n are spatial frequencies; a(m,n) are amplitudes; and φ(m,n) are phase angles.

To modify the model for this inclusion of the roughness to the interface, Gaussian and uniform randomness variables were included to the parameters, and the addition of the formula below was added to the equation defining the parametric surface interface:

$$z = 0.005 \cdot sum(sum(if(m! = 0)||(n! = 0), ((m^2 + n^2)^{-\frac{b}{2}} \cdot g1(m,n)$$

$$\cdot cos(2\pi(m \cdot s1 + n \cdot s2) + u1(m,n)), 0), m, -N, N), n, -N, N) \qquad (7.16)$$

where m and n are spatial frequencies, b is the spectral exponent, g1 is the function name used to define the Gaussian randomness applied to the geometry, s1 and s2 are the coordinates of the interface in the x and y axis respectively, varying between 0 and 1.5, u1 is the function name used to define the uniform randomness applied to the geometry and N is spatial frequency resolution.

7.2   Visual Comparisons

Roughness was applied to all five of the previously studied morphologies. Those being the planar interface, as well as the prismatic, pyramidish, proper pyramidal and waves geometries.
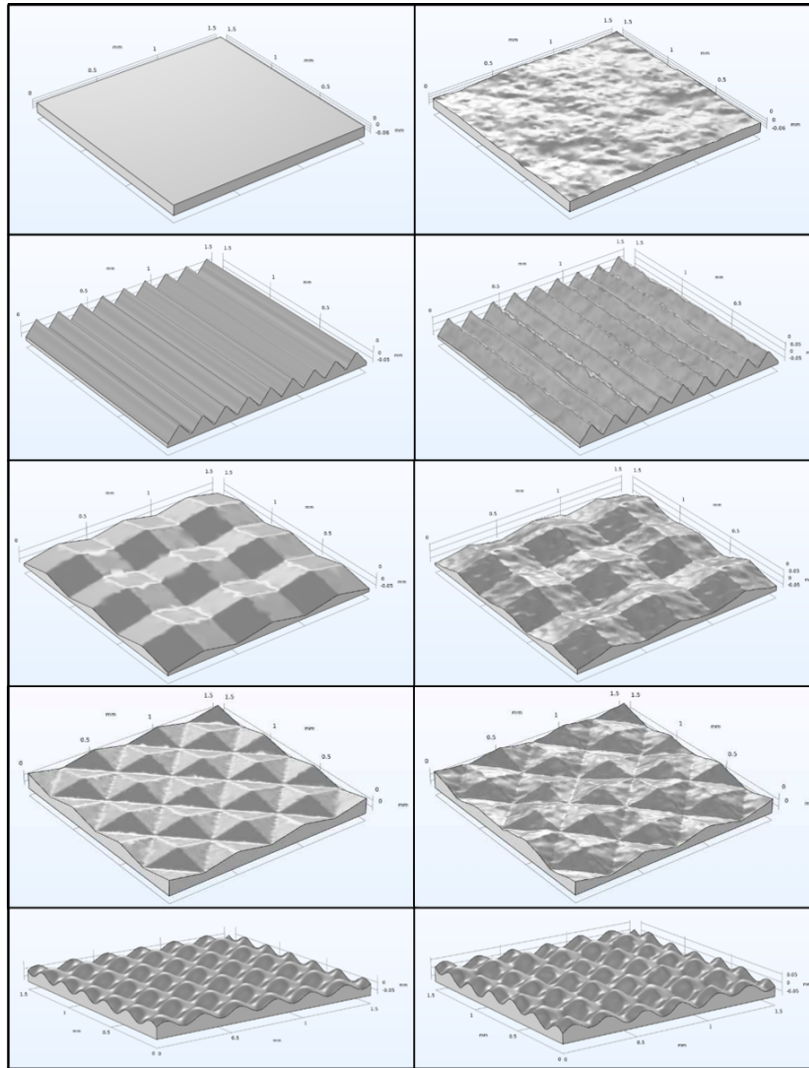
Figure 7.1: Comparative images of the planar, prismatic, pyramidish, proper pyramidal and waves models with (right column) and without (left column) the applied roughness.
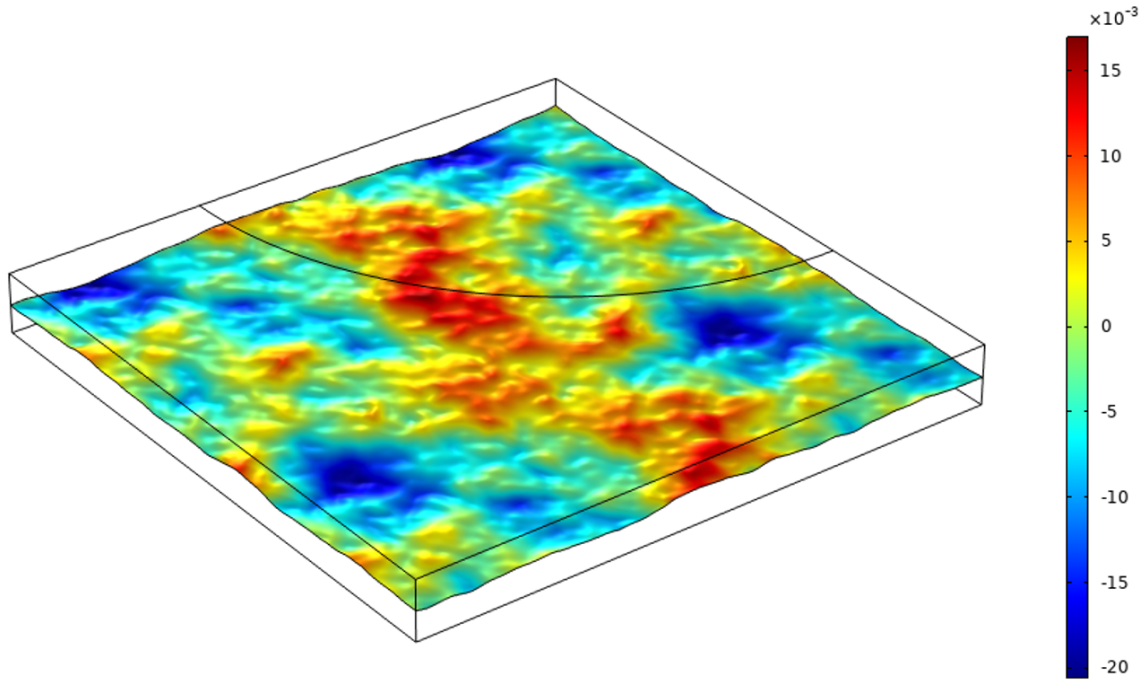
Figure 7.2: Colour plot of the planar model with applied roughness, showing the variance in height.

7.3   Data Analysis

Recording data from models which have roughness applied to the surface, requires a lot more time than with smooth models. This is because when generating the roughness for the interface, a seed 's' must be used, where 's' is a positive integer. Depending on the value of 's' used, will generate a different roughness interface, which will result in a different fuel cell performance, as shown in Figure 7.3. Therefore, in order to produce an accurate representation of the impact of the applying roughness to the interfaces, multiple models have to be run for each set of parameters (height and frequency of peaks), but with only the seed value changing.
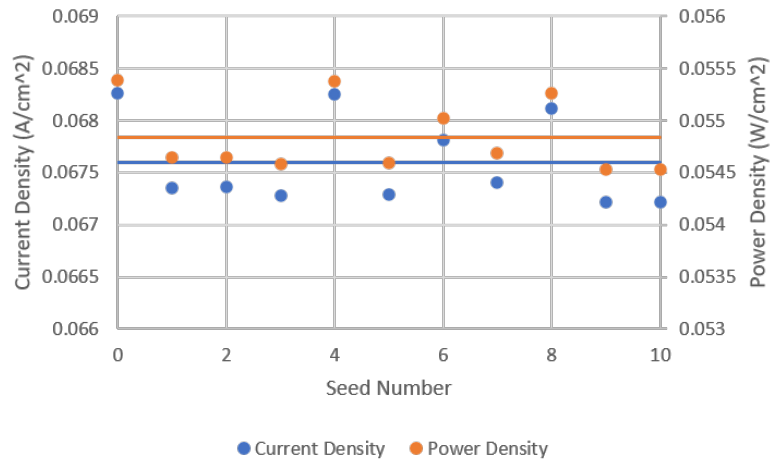
Figure 7.3: The difference in the current density and power density results with different seed numbers.

The impact of the application of roughness on the model is shown in Figure 7.4, where the polarisation curve and power density curves of the models with and without roughness are compared.
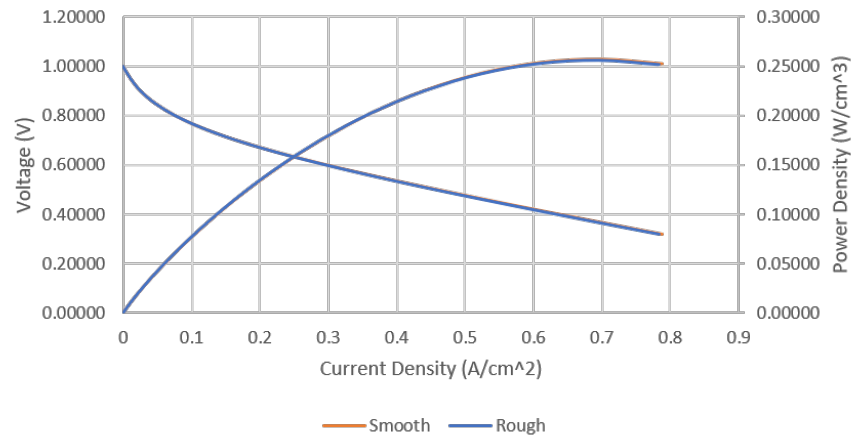
Figure 7.4: Polarisation and power density curves of the planar model with and without roughness.

As can be seen from the Figure 7.4, there is very little difference between the planar models with and without roughness. It was expected that the inclusion of the roughness would generate a surface with a slightly larger surface area, and therefore a

small improvement in performance. However, there is a slight deterioration of 0.33%
in the power density due to the inclusion of roughness to the planar interface, and
a small drop in the maximum power density from 0.257 W/cm^2 to 0.256 W/cm^2.
This is believed to be due to the roughness impacting on the 'perfect' ORR interface,
reducing the rate of the reaction. It is suspected that this negative impact on the
power performance is more significant than the benefit gained from the increased ac-
tive surface area, resulting in an overall net reduction in power performance.

To further evaluate these observations, a comparison of all patterned models inves-
tigated before with and without roughness are conducted. Figure 7.5 shows the
polarisation curve and power density curve of the prismatic model with a peak height
of 0.1 mm at a frequency of six peaks per millimetre.
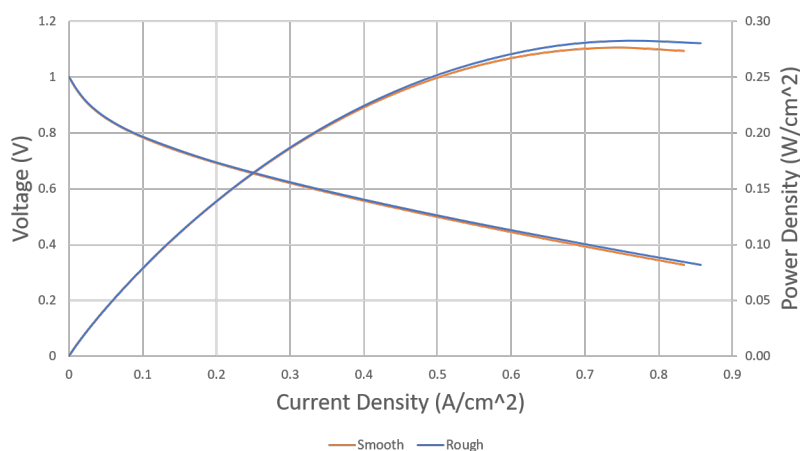
Figure 7.5: Polarisation curves and power density curves of the prismatic model,
with a frequency of 6 peaks per mm at a peak height of 0.1 mm, with and without
roughness.

The results are different from what was observed with the planar model. The pris-
matic model applied with roughness showing an average improvement in the power
density of 2.23%, ranging from 1.58-3.54% across the cathode polarisation range of 0

to -0.7 V, and a 2.35% increase in the maximum power density, from 0.276 W/cm^2 up to 0.283 W/cm^2. In the standard operating voltage conditions, this change in the power density is roughly an increase of 1.61%, from 0.1778 W/cm^2 to 0.1807 W/cm^2. The believed reason for this improvement compared to the reduced performance seen in the planar models is because although there is still the believed increase in active surface area due to the applied roughness, the reductive factor observed in the planar model due to the roughness impacting the 'perfect' nature of the interface, is not as strongly observed in the prismatic model. This is because the 'perfect' nature of the model has already been compromised by the inclusion of the patterning of the interface. Therefore, although there may still be an element of a reduction in performance due to the roughness impacting the 'perfect' nature of the smooth interface, this negative factor is now significantly smaller, and therefore outweighed by the benefits of the increased active surface area.

To confirm that this is the case, a second comparison was with the proper pyramidal model. to back up this hypothesis.
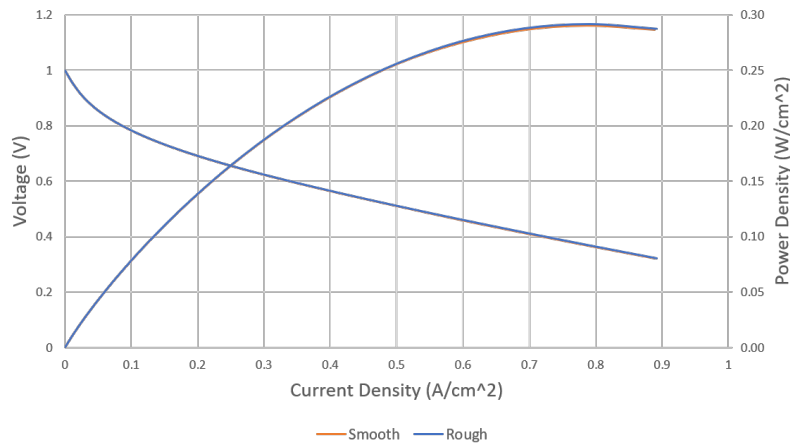
Figure 7.6: Polarisation and power density curves of the proper pyramidal structure with and without roughness, with patterning parameters of F=6 and H=0.1 mm.

According to our previous hypothesis, given that the proper pyramidal structure is more complicated than the prismatic structure, it would be expected that the performance of the interface with roughness applied, compared to the smooth version, would have an even more noticeable increase.

This is not the case. There is an overall average improvement in power density of 0.11%, ranging from -0.17 to 0.45% across the cathode polarisation range of 0 V to -0.7 V. There was also a very small increase in the maximum power density, going from approximately 0.2906 W/cm^2, up to 0.2915 W/cm^2, equivalent to only 0.3% improvement. In the standard operating voltage conditions, this change in the power density is roughly an increase of 0.08%, increasing from 0.1650 W/cm^2 to 0.1651 W/cm^2.

Table 7.1: Quantitative data showing the relative impact of roughness on performance with three different interfaces, as a percentage.

	Planar	Prismatic	Proper Pyramidal
Maximum Power Density	-0.33	3.54	0.03
Power Density within Operating Voltage (0.6-0.7V)	-0.5	1.61	0.08
Current Density within Operating Voltage (0.6-0.7V)	-0.31	1.62	0.08

Although the previous hypothesis does not stand true anymore, there is another argument for this observation. As the geometry of the interface becomes more complex, the difference in the improvement in performance can be expected to become less and less, as is seen when comparing the Prismatic and Proper Pyramidal data. However, there is not a massive difference observed for the rough and smooth Planar comparison because of the previously mentioned negative influence of disrupting the 'perfect' interface. The negative impact is so significant that it actually overshadows the pos-

itive aspect of the increased surface area. This follows the observations seen for the reduction in performance seen by the patterned morphologies at low frequencies.

7.3.1   Parameters of Roughness

There are three main parameters that are used to define the roughness of a surface.

- Ra - The Average Roughness of a Surface

- Rq - The Root-Mean-Square Roughness of a Surface

- Rz - The Difference between the tallest peak and the deepest valley of a Surface

As an example for these three parameters, they were calculated for the planar model.

For calculating Ra, the average roughness of the surface, as depicted in Figure 7.7, Equation 7.17 is used,

$$\text{Ra} = \frac{1}{L} \int_0^L |f(x) - g(x)| dx \tag{7.17}$$

where L is the length of the surface, $f(x)$ is the function of the roughness, and $g(x)$ is the function of the surface prior to the applied roughness.

However, this is only the equation for finding the Ra value of a 1D surface. For a 2D surface, a second integral is required, as shown in equation 7.18,

$$Ra = \frac{1}{A} \int_0^{L_x} \int_0^{L_y} |f(x,y) - g(x,y)| dx dy \tag{7.18}$$

where A is the surface area of the interface before applying the roughness, L_x and L_y are the lengths of the surface in the x and y directions respectively, f(x,y) is the function of the roughness, and g(x,y) is the function of the surface prior to the applied
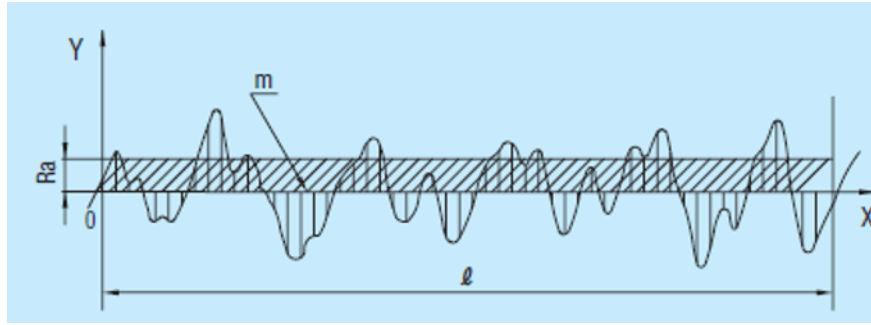
roughness.

Figure 7.7: 1D Illustration of a surface, showing how Ra correlates to the roughness of a surface [29].

Therefore, to calculate the average roughness of the planar model, the f(x,y) and g(x,y) functions have been placed into equation 7.18.

$$Ra = \frac{1}{2.25} \int_0^{1.5} \int_0^{1.5} |f(x,y) - 0| dxdy \qquad (7.19)$$

This has been greatly simplified because the g(x,y) function of the planar model is z=0. The value of Ra will be different for each individual seed used for the model, so an average should be taken for all of the individual results.

Table 7.2: Table showing the individual average roughness values, for seed 0-10, of the planar, and the average of those values, which is the Ra parameter for the planar model

Seed	Ra (mm^2)
0	0.0054
1	0.0113
2	0.0063
3	0.0058
4	0.0088
5	0.0097
6	0.0064
7	0.0056
8	0.0050
9	0.0058
10	0.0083
Average	0.0071

Therefore, this gives an Ra value for the surface roughness of the planar interface of 0.0071.

Calculating the root mean square of a surface roughness, Rq, can be done by taking the square of each of the $\left(f(x, y) - g(x, y) \right)$ terms, solving a double integral within the length boundaries of the model, and dividing by the area of the model.

$$Rq = \sqrt{ \frac{1}{A} \int_0^{L_x} \int_0^{L_y} \left(f(x, y) - g(x, y) \right)^2 dx dy } \tag{7.20}$$

If all calculations are done correctly, the Ra and Rq values should be exactly the same.

Table 7.3: Table showing the individual root mean square average roughness values, for seed 0-10, of the planar model, and the average of those values, which is the Rq parameter for the planar model.

Seed	Rq (mm^2)
0	0.0054
1	0.0113
2	0.0063
3	0.0058
4	0.0088
5	0.0097
6	0.0064
7	0.0056
8	0.0050
9	0.0058
10	0.0083
Average	0.0071

Therefore, this gives a Rq value for the surface roughness of the planar interface of 0.0071, which is indeed the same as the Ra value. This is very close to the expected value of 0.005, which was the multiplication factor applied at the beginning of Equation 7.16 which defined the topography of the parametric surface.

The Rz values of the roughness of the surface can be calculated by subtracting the height of the lowest valley from the height of the highest peak. Table 7.4 shows all the peak and valley heights of the roughened surfaces for seeds 0-10.

Table 7.4: Table showing all the peak and valley heights of the roughened surfaces of the planar model, to four decimal places, for seeds 0-10, and their resultant Rz values.

Seed	Highest Peak (mm)	Lowest Valley (mm)	Rz (mm)
0	0.0168	-0.0206	0.0374
1	0.0318	-0.0279	0.0597
2	0.0175	-0.0225	0.0400
3	0.0193	-0.0181	0.0373
4	0.320	-0.0248	0.0568
5	0.0288	-0.0221	0.0509
6	0.2474	-0.0258	0.0505
7	0.2358	-0.0166	0.0401
8	0.0218	-0.0177	0.0395
9	0.0181	-0.0151	0.0332
10	0.0233	-0.0243	0.0457
Average			0.0449

The final Rz value for the planar interface can be taken from the average of all the recorded Rz values for each seed number, giving the planar model an Rz value of 0.0449.

One interesting way to analyse the significance of Ra, Rq and Rz is to see if there is any correlation between these surface roughness parameters, and the power density.

As can be seen in Figure 7.8, there is no correlation between average surface roughness and cell power density. Similarly, Figure 7.9 shows there is no correlation between Rz and cell power density. However, roughness can have an impact on power performance depending on how the applied roughness changes the total volume of the catalyst layer.

Figure 7.10 shows there is a strong positive correlation between the changed volume of the catalyst layer, caused by the applied roughness, and cell power density.
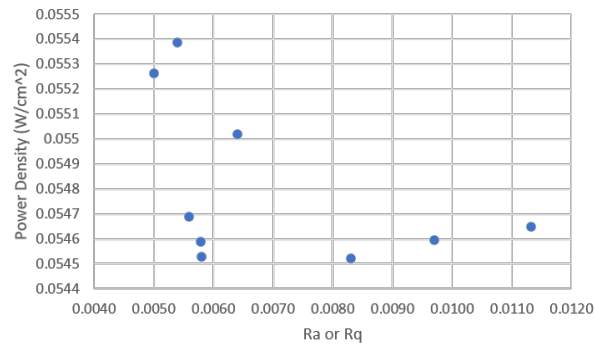
Figure 7.8: Chart showing there is no correlation between average surface roughness of the planar model and the cell power density.
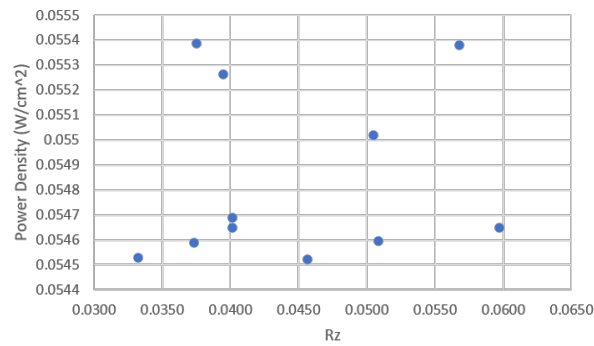
Figure 7.9: Chart showing there is no correlation between Rz of the planar model and the cell power density.
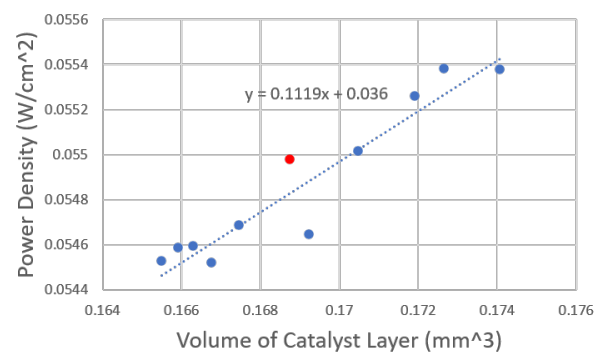
Figure 7.10: Chart showing the relationship between catalyst layer volume and power density, resulting from the application of roughness to the planar model.

For a reference, the point in red is the catalyst layer volume and power density of the planar model without roughness. This makes sense, given a larger amount of catalyst would result in a faster ORR, resulting in improved cell performance. However, since the total volume of the catalyst layer and membrane are fixed at a combined 0.375 mm^2, there is every argument to be made that the improvement in performance is actually due to the reduction in the volume of the membrane. This would also make sense, as a thinner membrane would allow for faster diffusion of hydride ions through the membrane, increasing the ORR and improving the cell performance.

7.4 Conclusions

In this chapter, the influence of the interface roughness was studied to three geometries: planar, prismatic and proper pyramid geometries. The results show that as the complexity of the geometry is increased, the resultant impact of the application of roughness on the resulting fuel cell performance becomes less impactful. There is a negative impact from the application of the roughness to the planar interface. This is in keeping with the observations for the interfaces patterned with low frequencies, since the disruption to the 'perfect' planar interface is the cause for the reduction in performance. The introduction of the surface roughness demonstrates positive impacts on the power density of the prismatic and Proper Pyramidal geometries. While nearly the same power performance was obtained for the Proper Pyramidal geometry with and without roughness, the prismatic geometry exhibits an increase of 3.54% in the maximum power density, showing the complexity by using the more real-life interface.

Surface roughness parameters were also calculated for the planar geometry. Although calculating the average surface roughness to be 0.0071 and Rz to be 0.0447, it was shown there was no correlation between them and cell power density. However, there was a strong positive correlation between the volume of the catalyst layer, changed due to the application of roughness, and the cell power performance. This is likely a combination of an increased volume of catalyst layer meaning there is more catalyst, and therefore the ORR will be faster, and also that the membrane would be thinner, meaning hydride ions can cross the electrolyte membrane faster, also resulting in a larger ORR, resulting in a better cell performance. Due to the time limit, the waves geometry and a further analysis of the roughness details could be conducted in future.

Chapter 8

Conclusions and Outlook

This thesis focused on the numerical simulation of the cathode-electrolyte patterned interface to understand the influence mechanisms of increasing the effective surface area at the interface on the improvement of the power density output of the PEMFC. The CFD software was used to facilitate simulating the models by using LiveLink between Matlab and COMSOL Multiphysics, and time was saved over building rigs for running practical experimentations, allowing for multiple models to be run consecutively.

8.1   Conclusions

For numerical simulation, a default model was built for the planar geometry based on the half-cell model of the PEMFC available in the COMSOL Multiphysics library. The two main focal points were used for building the electrochemistry of the model: the 'Secondary Current Distribution' used to model the electronic and ionic current balances, and the 'Transport of Concentrated Species', which was used to model the species mass transport in the cathode by using Maxwell-Stefan equations. A fine

user-defined mesh was built to ensure a more accurate assessment of the power performance within the fuel cell, specifically, the polarisation and power density curves of the model. This gave a power performance baseline for all kinds of patterned interfaces to be compared against.

The model was then advanced to build the prismatic patterned interface, with which parameters of the peak frequency and height were used to vary the geometry of the interface to evaluate their influence on the fuel cell power performance. The application of the patterned interface offered an increase in the active surface area of the interface, but it led to a reduction in the power performance at low peak frequencies. This was ascribed to the disruption caused to the perfect interface of the planar model. However, at higher frequencies, this negative effect was overshadowed by the improvement due to the increased surface area thus a higher power performance was obtained. For the model prismatically patterned with a frequency of 10 peaks per mm at a height of peaks of 0.1 mm, the maximum power density is increased by 14.8% compared to the planar interface. At the PEMFC standard operation voltage 0.6 V, an increased power density of 22.91% was achieved.

The relationship between the surface area and the power density was then investigated. The results showed the power density increased with the surface area within the low surface area range, but became plateaued at a certain surface area. This was then employed to estimate the optimal frequency and height of peaks to maximise the potential power density. An optimal surface area was achieved at 20.4 mm^2, using a peak frequency of of 45.1 peaks per mm at a peak height of 0.1 mm, generating a power density of 5.515 W/cm^2. It was shown that the physical dimensions of these peaks were practically achievable, requiring a base width of 22.2 μm and a tip angle of 12.7°.

To evaluate the simulation results, experiments were conducted to fabricate prismatic patterned membrane. Nafion 212 with a peak width of about 33.3 μm was fabricated using the hot embossing process. At a low catalyst loading of 0.1 $mg_{Pt}cm^{-2}$, the enlarged active surface area of prismatic interface showed about 17% improvement in the maximum power density, confirming the positive effects predicted by the numerical simulation.

Based on the understanding obtained with the prismatic morphology, other interface morphologies were then built, including 'Pyramidish', 'Proper Pyramid' and 'Waves' geometries. Similar to the prismatic interface, each of the three new geometries showed negative results at low frequencies, and positive effects due to the inclusion of the patterned interface at higher peak frequencies and height. As expected, given the pyramidish and proper pyramid geometries shared identical surface area profiles, they recorded similar results. Despite the prismatic geometry having the lowest surface area profile among the four patterned interfaces, it showed the best power performance. Although further research is still needed to confirm the mechanism beyond, it is believed to be related to improved water management by the preferential flow channels provided by the prismatic morphology, although this is difficult to claim until a GDL is included within the model. Similarly, the waves geometry showed slightly superior performance compared to the pyramidish and proper pyramid geoemtries, despite having a smaller surface area. At the frequency of 6 peaks per mm and the peak height of 0.1mm, the maximum power density improvement are for Prismatic of +13%, Waves of +11.4%, Pyramidish of +9.2% and Proper Pyramid of +8% compared to the planar morphology.

The impact of the arrangement of pyramids for the proper pyramid geometry was also studied. The results showed an improved performance was obtained when pyramids were arranged in longer channels rather than in blocks of pyramids. For example, 20 pyramids orientated in a 2 by 10 formation reached up to 15.68% improvement compared to the planar model, as opposed to 13.11% when orientated in a 4 by 5 formation. Given the trigonometric nature of the Waves geometry, an investigation was also conducted to understand the impact of phase shift. It was shown that applying a phase shift had more of an impact on the power performance at lower frequencies, amplified by increasing the amplitude of the wave peaks. The reasoning for this is that at lower frequencies, the phase shift shows a larger impact on the alignment of the interface with respect to transport of the reactant and water, resulting in a more noticeable change in the power performance. At higher frequencies, the impact of the phase shift is less noticeable, as the apparent change in the interface morphology is much less.

Finally, the surface roughness was applied to the interfaces with planar, prismatic and proper pyramid geometries, making the models more in line with practical fuel cells. For the planar and the proper pyramid geometry model, applying surface roughness resulted in very little influence to the fuel cell power performance, with -0.5% and 0.08% change in the maximum power density, respectively. The prismatic interface exhibited only a little improvement in the maximum power density of 1.61%. A belief for why there is less change in the power performance for the Planar and Proper Pyramid interface is that as the morphology of the interface becomes more complex, the impact by increasing the surface area is less effective on the surface morphology, thus, having a lesser impact on power performance results. This implies that the models with more complex geometries, such as the Proper Pyramid, is more

applicable when comparing with practical data. Surface roughness parameters were also calculated for the planar model, showing an average Rz value of 0.0449 and an average surface roughness of 0.0071. This value of average surface roughness is very close to the expected outcome of 0.005, which was the multiplication factor applied to the equation used to generate the rough topography of the parametric surface. It was shown that these values had no correlation with the power density. However, the changes in the volume of the catalyst layer as a result of the applied roughness exhibited a positive correlation with the fuel cell power density. This is likely due to a combination of both increasing the volume of the catalyst layer and reducing the thickness of the membrane.

8.2   Perspectives

This PhD work demonstrated the promising effects of using the patterned interface between the cathode and electrolyte membrane on the PEMFC power performance, combining both the numerical simulation and experimental techniques. However, due to the time limit, the influence of the Covid-19 pandemic and the resource available because of the frequent breakdown of the computer server, some work has not been able to be conducted. Based on the current understanding, a few perspective points are listed below:

- The experimental work has been conducted to evaluate the prismatic interface. This is also required for various morphologies with different peak frequencies and heights to check the simulation results obtained, thus experimental results can be used to polish the model to allow for accurate prediction of future work. Given the dimensions calculated for the height and frequency of peaks chosen for the simulated models, this can be reproduced experimentally. However,

the model does not account for damage to the membrane interface during the patterning process, which would consequently lead to yielding poorer results.

- The improvement in the water management by using the patterned interface is also explored in this work, as that in the literature. However, there still lacks direct evidence for this conclusion. Synchrotron operando characterization could be combined with the single cell test to evaluate this improvement in the water management in the membrane electrode assemblies with the patterned interface.

- The current half-cell model used in this work led to some inaccurate simulation at the low frequency, in particular how to involve the contact effect between the catalyst layer and the patterned membrane considering the large agglomerate size of the commercial Pt/C catalyst used today, as also mentioned in Chapter 5.

- The current half-cell model was restricted by only consisting of a membrane and a cathode-catalyst layer. Expanding the model to include a GDL could improve the validity of the model, as it would better simulate the impact patterning the morphology of the interface has on water management.

- The simulation of this work was carried out with a high spec PC in our Centre, but to do simulation closer to the real life-context operation, a large simulation volume is required, e.g. from the current 1.5 mm * 1.5 mm to centimetre or decimetre scale. In this case, the University supercomputer, such as BlueBEAR could be employed to extend the current work to better understand the influence mechanism.

References

[1] Global direct primary energy consumption. `https://ourworldindata.org/grapher/global-primary-energy?country=~OWID_WRL`.

[2] Wikimedia Commons. File:solid oxide fuel cell protonic.svg — wikimedia commons, the free media repository. `https://commons.wikimedia.org/w/index.php?title=File:Solid_oxide_fuel_cell_protonic.svg&oldid=518795896`, 2020. [Online; accessed 14-March-2022].

[3] Wenchao Sheng, MyatNoeZin Myint, Jingguang G Chen, and Yushan Yan. Correlating the hydrogen evolution reaction activity in alkaline electrolytes with the hydrogen binding energy on monometallic surfaces. Energy & Environmental Science, 6(5):1509–1512, 2013.

[4] Francesco Valle. Electrocatalyst degradation in high temperature PEM fuel cells. PhD thesis, 04 2015.

[5] Vuppala, Chedir, Jiang, Chen, Muhammad Aziz, and A.P. Sasmito. Optimization of membrane electrode assembly of pem fuel cell by response surface method. Molecules, 24:3097, 08 2019.

[6] Matthew Bont, Carol Barry, and Stephen Johnston. A review of liquid silicone rubber injection molding: Process variables and process modeling. Polymer Engineering & Science, 61(2):331–347, 2021.

[7] Zhilian Zhou, Raymond N Dominey, Jason P Rolland, Benjamin W Maynor, Ashish A Pandya, and Joseph M DeSimone. Molded, high surface area polymer electrolyte membranes from cured liquid precursors. Journal of the American Chemical Society, 128(39):12963–12972, 2006.

[8] Silicone compression molding.

[9] Y. Lisunova and J. Brugger. Combination of thermal scanning probe lithography and ion etching to fabricate 3d silicon nanopatterns with extremely smooth surface. Microelectronic Engineering, 193:23–27, 2018.

[10] Jin Woo Bae, Yong-Hun Cho, Yung-Eun Sung, Kyusoon Shin, and Jae Young Jho. Performance enhancement of polymer electrolyte membrane fuel cell by employing line-patterned nafion membrane. Journal of Industrial and Engineering Chemistry, 18(3):876–879, 2012.

[11] Yong He, Jian-Zhong Fu, and Zi-Chen Chen. Research on optimization of the hot embossing process. Journal of Micromechanics and Microengineering, 17(12):2420–2425, oct 2007.

[12] M. Hakan Yildirim, J. te Braake, H. Can Aran, D.F. Stamatialis, and M. Wessling. Micro-patterned nafion membranes for direct methanol fuel cell applications. Journal of Membrane Science, 349(1):231–236, 2010.

[13] Plasma etching for semiconductor.

[14] Ashvini B. Deshmukh, Vinayak S. Kale, Vishal M. Dhavale, K. Sreekumar, K. Vijayamohanan, and Manjusha V. Shelke. Direct transfer of micro-molded electrodes for enhanced mass transport and water management in pemfc. Electrochemistry Communications, 12(11):1638–1641, 2010.

[15] Changwook Seol, Segeun Jang, Jinwon Lee, Le Vu Nam, Tuyet Anh Pham, Seunghoe Koo, Kyeongtae Kim, Jue-Hyuk Jang, Sang Moon Kim, and Sung Jong Yoo. High-performance fuel cells with a plasma-etched polymer electrolyte membrane with microhole arrays. ACS Sustainable Chemistry & Engineering, 9(17):5884–5894, 2021.

[16] Alongkorn Pimpin and Werayut Srituravanich. Review on micro- and nano-lithography techniques and their applications. Engineering Journal, 16:37–56, 01 2012.

[17] A Omosebi and RS Besser. Electron beam assisted patterning and dry etching of nafion membranes. Journal of The Electrochemical Society, 158(10):D603, 2011.

[18] Mengbo Ji and Zidong Wei. A review of water management in polymer electrolyte membrane fuel cells. Energies, 2(4):1057–1106, 2009.

[19] David C Grahame. Differential capacity of mercury in aqueous sodium fluoride solutions. i. effect of concentration at 25. Journal of the American Chemical Society, 76(19):4819–4823, 1954.

[20] Savanna Alderman. Chapter 25 electron transfer in heterogeneous systems processes. https://slidetodoc.com/chapter-25-electron-transfer-in-heterogeneous-systems-processes/, 2015.

[21] 8. fundamentals of charged surfaces - [ppt powerpoint].

[22] Ekaterina Gongadze, Ursula Van Rienen, and Aleš Iglič. Generalized stern models of the electric double layer considering the spatial variation of permittvity and finite size of ions in saturation regime. Cellular & molecular biology letters, 16(4):576–594, 2011.

[23] Sarah Horswell. Dynamic electrochemistry and the electrode | electrolyte interface, 2018.

[24] JO'M Bockris, MAV Devanathan, and K Müller. On the structure of charged interfaces. In Electrochemistry, pages 832–863. Elsevier, 1965.

[25] F. Standaert, K. Hemmes, and N. Woudstra. Analytical fuel cell modeling; non-isothermal fuel cells. Journal of Power Sources, 70(2):181–199, 1998.

[26] Thomas E Springer, TA Zawodzinski, and Shimshon Gottesfeld. Polymer electrolyte fuel cell model. Journal of the electrochemical society, 138(8):2334, 1991.

[27] https://cn.comsol.com/model/download/633571/models.bfc.fuel_cell_cathode.pdf.

[28] Surface area of triangular prism - formula, examples, definition.

[29] Rosler. A guide to understanding surface roughness measurement types, Aug 2017.

[30] Aashish Priye. Could anyone help me identify the limitations of comsol over dedicated ... https://www.researchgate.net/post/Could_anyone_help_me_identify_the_limitations_of_comsol_over_dedicated_CFD_solvers_such_as_fluent_starccm, Sep 2014.

[31] Xiaolong Wang, Hui Yue, Guangliang Liu, and Zhao Zhao. The application of comsol multiphysics in direct current method forward modeling. Procedia Earth and Planetary Science, 3:266–272, 2011.

[32] Chad Jackson. Comsol: A different multi-physics approach. https://www.lifecycleinsights.com/comsol/, Jul 2019.

[33] Filippo Marchelli and Renzo Di Felice. A comparison of ansys fluent and mfix in performing cfd-dem simulations of a spouted bed. Fluids, 6(11):382, 2021.

[34] Scott Sichmeller, Juan Carlos Molina Castejon, and Tony Dang. Autodesk inventor reviews ratings 2023, 2020.

[35] Mark Williams. Simscale reviews ratings 2023, Jul 2022.

[36]

[37] Phyllis M Deane and Phyllis M Deane. The first industrial revolution. 1979.

[38] Joel Mokyr and Robert H Strotz. The second industrial revolution, 1870-1914, volume 21945. Citeseer, 1998.

[39] David MacKay. David mackay frs: : Contents. `https://www.withouthotair.com/`.

[40] Rebecca Lindsey. Climate change: Atmospheric carbon dioxide. `https://www.climate.gov/news-features/understanding-climate/climate-change-atmospheric-carbon-dioxide`, Jun 2022.

[41] Rahmstorf Stefan. The global co2 rise: The facts, exxon and the favorite denial tricks, Feb 2018.

[42] Center for Climate and Energy Solutions. Global emissions, Jan 2020.

[43] Shafiqur Rehman, Luai M. Al-Hadhrami, and Md. Mahbub Alam. Pumped hydro energy storage system: A technological review. Renewable and Sustainable Energy Reviews, 44:586–598, 2015.

[44] Mustafa E. Amiryar and Keith R. Pullen. A review of flywheel energy storage system technologies and their applications. Applied Sciences, 7(3), 2017.

[45] Chao Zhang, Yi-Li Wei, Peng-Fei Cao, and Meng-Chang Lin. Energy storage system: Current studies on batteries and power condition system. Renewable and Sustainable Energy Reviews, 82:3091–3106, 2018.

[46] Pieter Tielens and Dirk Van Hertem. Grid inertia and frequency control in power systems with high penetration of renewables. In Young Researchers Symposium in Electrical Power Engineering, Date: 2012/04/16-2012/04/17, Location: Delft, The Netherlands, 2012.

[47] Jean-Paul Rodrigue. The geography of transport systems. Routledge, 2020.

[48] Brandon Miller. 11 big advantages and disadvantages of hydrogen fuel cells. `https://greengarageblog.org/11-big-advantages-and-disadvantages-of-hydrogen-fuel-cells`, Nov 2020.

[49] Meed. Realising the hydrogen economy. `https://www.power-technology.com/comment/standing-at-the-precipice-of-the-hydrogen-economy/#:~:text=The%20'hydrogen%20economy'%20refers%20to,carbon%20and%20carbon%20dioxide%20emissions.`, Oct 2019.

[50] Richard P Gangloff and Brian P Somerday. Gaseous hydrogen embrittlement of materials in energy technologies: the problem, its characterisation and effects on particular alloy classes. 2012.

[51] E.ON Energy UK. What is combined heat and power (chp)? `https://www.youtube.com/watch?v=YShdos4wKKY`, 2017.

[52] SA Sherif, N Zeytinoglu, and TN Veziroğlu. Liquid hydrogen: Potential, problems, and a proposed research program. International journal of hydrogen energy, 22(7):683–688, 1997.

[53] R Prabhukhot Prachi, M Wagh Mahesh, and C Gangal Aneesh. A review on solid state hydrogen storage material. Adv. Energy Power, 4(11), 2016.

[54] Billur Sakintuna, Farida Lamari-Darkrim, and Michael Hirscher. Metal hydride materials for solid hydrogen storage: a review. International journal of hydrogen energy, 32(9):1121–1140, 2007.

[55] Ellen Ivers-Tiffée, André Weber, and Dirk Herbstritt. Materials and technologies for sofc-components. Journal of the European Ceramic Society, 21(10):1805–1811, 2001.

[56] Fuel cell technology Elcogen. How sofc can change the world? `https://www.youtube.com/watch?v=YShdos4wKKY`.

[57] Arnab Choudhury, H. Chandra, and A. Arora. Application of solid oxide fuel cell technology for power generation—a review. Renewable and Sustainable Energy Reviews, 20:430–442, 2013.

[58] Keith Scott and Lei Xing. Chapter 3 - direct methanol fuel cells. In Kai Sundmacher, editor, Fuel Cell Engineering, volume 41 of Advances in Chemical Engineering, pages 145–196. Academic Press, 2012.

[59] A. S. Aricò, S. Srinivasan, and V. Antonucci. Dmfcs: From fundamental aspects to technology development. Fuel Cells, 1(2):133–161, 2001.

[60] Andrew L Dicks. Molten carbonate fuel cells. Current Opinion in Solid State and Materials Science, 8(5):379–383, 2004.

[61] Ermete Antolini. The stability of molten carbonate fuel cell electrodes: A review of recent improvements. Applied energy, 88(12):4274–4293, 2011.

[62] Tushar K. Maiti, Sumit Parvate, Jitendra Singh, Prakhar Dixit, E. Bhuvanesh, Vennapusa J. Reddy, and Sujay Chattopadhyay. Polymers for electrolyte membrane fuel cells. In M.S.J. Hashmi, editor, Encyclopedia of Materials: Plastics and Polymers, pages 361–369. Elsevier, Oxford, 2022.

[63] G.F. McLean, T. Niet, S. Prince-Richard, and N. Djilali. An assessment of alkaline fuel cell technology. International Journal of Hydrogen Energy, 27(5):507–526, 2002.

[64] A. Kundu and J.H. Jang. Applications – portable | portable devices: Fuel cells. In Jürgen Garche, editor, Encyclopedia of Electrochemical Power Sources, pages 39–45. Elsevier, Amsterdam, 2009.

[65] Viral Mehta and Joyce Smith Cooper. Review and analysis of pem fuel cell design and manufacturing. Journal of power sources, 114(1):32–53, 2003.

[66] Carlotta Francia, Vijaykumar S. Ijeri, Stefania Specchia, and Paolo Spinelli. Estimation of hydrogen crossover through nafion® membranes in pemfcs. Journal of Power Sources, 196(4):1833–1839, 2011.

[67] Reza Omrani. Chapter 5 - gas diffusion layer for proton exchange membrane fuel cells. In Gurbinder Kaur, editor, PEM Fuel Cells, pages 91–122. Elsevier, 2022.

[68] MJ Lázaro, L Calvillo, V Celorrio, JI Pardo, S Perathoner, and R Moliner. Study and application of carbon black vulcan xc-72r in polymeric electrolyte fuel cells. Carbon black: production, properties and uses, 41, 2011.

[69] Ahmet Kusoglu and Adam Z Weber. New insights into perfluorinated sulfonic-acid ionomers. Chemical reviews, 117(3):987–1104, 2017.

[70] Adriano C Fernandes and Edson Antonio Ticianelli. A performance and degradation study of nafion 212 membrane for proton exchange membrane fuel cells. Journal of Power Sources, 193(2):547–554, 2009.

[71] Fuqiang Liu, Baolian Yi, Danmin Xing, Jingrong Yu, and Huamin Zhang. Nafion/ptfe composite membranes for fuel cell applications. Journal of Membrane Science, 212(1-2):213–223, 2003.

[72] Hazem Tawfik, Yue Hung, and Devinder Mahajan. Bipolar plate durability and challenges. In Polymer Electrolyte Fuel Cell Degradation, pages 249–291. Academic Press, 2012.

[73] Bipolar plates: Carbon or metal for pem fuel cells, 2019.

[74] Platinum-group metal reserves worldwide by country 2020, 2021.

[75] Platinum price live chart, 2022.

[76] Vahid Hasannaeimi and Sundeep Mukherjee. Noble-metal based metallic glasses as highly catalytic materials for hydrogen oxidation reaction in fuel cells. Scientific Reports, 9(1):1–8, 2019.

[77] Vijay Ramani, H Russell Kunz, and James M Fenton. The chalkboard: The polymer electrolyte fuel cell. The Electrochemical Society Interface, 13(3):17, 2004.

[78] A-S Feiner and AJ McEvoy. The nernst equation. Journal of chemical education, 71(6):493, 1994.

[79] Jens Kehlet Nørskov, Jan Rossmeisl, Ashildur Logadottir, LRKJ Lindqvist, John R Kitchin, Thomas Bligaard, and Hannes Jonsson. Origin of the over-potential for oxygen reduction at a fuel-cell cathode. The Journal of Physical Chemistry B, 108(46):17886–17892, 2004.

[80] Frano Barbir. PEM fuel cells: theory and practice. Academic press, 2012.

[81] KR Cooper and M Smith. Electrical test methods for on-line fuel cell ohmic resistance measurement. Journal of Power Sources, 160(2):1088–1095, 2006.

[82] Sebastian Ott, Andreas Bauer, Fengmin Du, Tuan Anh Dao, Malte Klingenhof, Alin Orfanidi, and Peter Strasser. Impact of carbon support meso-porosity on mass transport and performance of pemfc cathode catalyst layers. ChemCatChem, 13(22):4759–4769, 2021.

[83] J St-Pierre, B Wetton, G-S Kim, and K Promislow. Limiting current operation of proton exchange membrane fuel cells. Journal of the Electrochemical Society, 154(2):B186, 2006.

[84] Sheng Sui, Xiaoying Wang, Xintong Zhou, Yuehong Su, Saffa Riffat, and Chang-jun Liu. A comprehensive review of pt electrocatalysts for the oxygen reduction reaction: Nanostructure, activity, mechanism and carbon support in pem fuel cells. Journal of Materials Chemistry A, 5(5):1808–1825, 2017.

[85] R Singh, PC Sui, KH Wong, E Kjeang, S Knights, and N Djilali. Modeling the effect of chemical membrane degradation on pemfc performance. Journal of The Electrochemical Society, 165(6):F3328, 2018.

[86] Donggun Ko, Ho Jae Kwak, and Moo Hwan Kim. The effects of water accumu-lation at the interface between gas diffusion layer and gas supplying channel on the water distribution in polymer electrolyte membrane fuel cells. International Journal of Hydrogen Energy, 44(45):24947–24953, 2019.

[87] Fengjuan Zhu, Liuxuan Luo, Aiming Wu, Chao Wang, Xiaojing Cheng, Shuiyun Shen, Changchun Ke, Hong Yang, and Junliang Zhang. Improving the high-current-density performance of pemfc through much enhanced utilization of platinum electrocatalysts on carbon. ACS Applied Materials & Interfaces, 12(23):26076–26083, 2020.

[88] Yukwon Jeon, Dong Jun Kim, Jong Kwan Koh, Yunseong Ji, Jong Hak Kim, and Yong-Gun Shul. Interface-designed membranes with shape-controlled patterns for high-performance polymer electrolyte membrane fuel cells. Scientific reports, 5(1):1–11, 2015.

[89] E.H. Majlan, D. Rohendi, W.R.W. Daud, T. Husaini, and M.A. Haque. Electrode for proton exchange membrane fuel cells: A review. Renewable and Sustainable Energy Reviews, 89:117–134, 2018.

[90] Dong Jin Ham, Young Kwon Kim, Seung Hyun Han, and Jae Sung Lee. Pt/wc as an anode catalyst for pemfc: Activity and co tolerance. Catalysis Today, 132(1):117–122, 2008. 11th Korea-Japan Symposium on Catalysis, 21-23 May 2007, Seoul, Korea.

[91] K. C. Neyerlin, Wenbin Gu, Jacob Jorne, Alfred Clark, and Hubert A. Gasteiger. Cathode catalyst utilization for the ORR in a PEMFC. Journal of The Electrochemical Society, 154(2):B279, 2007.

[92] Frano Barbir. Chapter 8 - fuel cell diagnostics. In Frano Barbir, editor, PEM Fuel Cells, pages 249–270. Academic Press, Burlington, 2005.

[93] Christophe Gerling, Matthias Hanauer, Ulrich Berner, and K. Andreas Friedrich. PEM single cells under differential conditions: Full factorial parameterization of the ORR and HOR kinetics and loss analysis. Journal of The Electrochemical Society, 169(1):014503, jan 2022.

[94] Joseph R Murdoch. What is the rate-limiting step of a multistep reaction? Journal of Chemical Education, 58(1):32, 1981.

[95] Süleyman kaytakoğlu and Levent Akyalçın. Optimization of parametric performance of a pemfc. International Journal of Hydrogen Energy - INT J HYDROGEN ENERG, 32:4418–4423, 12 2007.

[96] Samaneh Shahgaldi and Jean Hamelin. Improved carbon nanostructures as a novel catalyst support in the cathode side of pemfc: a critical review. Carbon, 94:705–728, 2015.

[97] Yanan Chen, Qing Zhong, Guangfu Li, Tian Tian, Jinting Tan, and Mu Pan. Electrochemical study of temperature and nafion effects on interface property for oxygen reduction reaction. Ionics, 24(12):3905–3914, 2018.

[98] Jennifer Peron, Ana Mani, Xinsheng Zhao, Dave Edwards, Makoto Adachi, Tatyana Soboleva, Zhiqing Shi, Zhong Xie, Titichai Navessin, and Steven Holdcroft. Properties of nafion® nr-211 membranes for pemfcs. Journal of Membrane Science, 356(1):44–51, 2010.

[99]   what nafion™ membrane thickness is right for an electrolyzer / hydrogen generation?

[100]   Homayoon Kanani, Mehrzad Shams, Mohammadreza Hasheminasab, and Ali Bozorgnezhad. Model development and optimization of operating conditions to maximize pemfc performance by response surface methodology. Energy Conversion and Management, 93:9–22, 2015.

[101]   Hansan Liu, Chaojie Song, Yuanhua Tang, Jianlu Zhang, and Jiujun Zhang. High-surface-area cotmpp/c synthesized by ultrasonic spray pyrolysis for pem fuel cell electrocatalysts. Electrochimica Acta, 52(13):4532–4538, 2007.

[102]   Jong Kwan Koh, Yukwon Jeon, Yong Il Cho, Jong Hak Kim, and Yong-Gun Shul. A facile preparation method of surface patterned polymer electrolyte membranes for fuel cell applications. Journal of Materials Chemistry A, 2(23):8652–8659, 2014.

[103]   Keyur Shah, W.C Shin, and R.S Besser. Novel microfabrication approaches for directly patterning pem fuel cell membranes. Journal of Power Sources, 123(2):172–181, 2003.

[104]   Ayokunle Omosebi and Ronald S. Besser. Electron beam patterned nafion membranes for dmfc applications. Journal of Power Sources, 228:151–158, 2013.

[105]   S. Cuynet, A. Caillard, J. Bigarré, and P. Buvat. Impact of the patterned membrane morphology on pemfc performances of ultra-low platinum loaded meas. International Journal of Hydrogen Energy, 42(12):7974–7985, 2017.

[106]   Advantages of silcione molds.

[107]   Matthew Bont, Carol Barry, and Stephen Johnston. A review of liquid silicone rubber injection molding: Process variables and process modeling. Polymer Engineering & Science, 61(2):331–347, 2021.

[108]   Dmc price charts.

[109]   Monthly price of rubber at the singapore commodity exchange from january 2020 to may 2022.

[110]   Robert A Tatara. 17.1 basics of processing by compression molding. Applied Plastics Engineering Handbook: Processing and Materials, page 289, 2011.

[111]   Joseph E Shaw, Paul N Stavrinou, and Thomas D Anthopoulos. On-demand patterning of nanostructured pentacene transistors by scanning thermal lithography. Advanced Materials, 25(4):552–558, 2013.

[112] Baptiste Gault, Michael P Moody, Julie M Cairney, and Simon P Ringer. Atom probe microscopy, volume 160. Springer Science & Business Media, 2012.

[113] Samuel Tobias Howell, Anya Grushina, Felix Holzner, and Juergen Brugger. Thermal scanning probe lithography—a review. Microsystems & nanoengineering, 6(1):1–24, 2020.

[114] Masato Aizawa, Hisaaki Gyoten, Abdu Salah, and Xinbing Liu. Pillar structured membranes for suppressing cathodic concentration overvoltage in pemfcs at elevated temperature/low relative humidity. Journal of The Electrochemical Society, 157:B1844–B1851, 12 2010.

[115] M Heckele, W Bacher, and KD Müller. Hot embossing-the molding technique for plastic microstructures. Microsystem technologies, 4(3):122–124, 1998.

[116] Linfa Peng, Yujun Deng, Peiyun Yi, and Xinmin Lai. Micro hot embossing of thermoplastic polymers: a review. Journal of Micromechanics and Microengineering, 24(1):013001, 2013.

[117] David J Guckenberger, Theodorus E De Groot, Alwin MD Wan, David J Beebe, and Edmond WK Young. Micromilling: a method for ultra-rapid prototyping of plastic microfluidic devices. Lab on a Chip, 15(11):2364–2378, 2015.

[118] Cornelius T Moynihan, Allan J Easteal, James Wilder, and Joseph Tucker. Dependence of the glass transition temperature on heating and cooling rate. The journal of physical chemistry, 78(26):2673–2677, 1974.

[119] Swarup S Deshmukh and Arjyajyoti Goswami. Hot embossing of polymers–a review. Materials Today: Proceedings, 26:405–414, 2020.

[120] Avinash P. Nayak, M. Saif Islam, and V. J. Logeeswaran. Wet Etching, pages 2829–2830. Springer Netherlands, Dordrecht, 2012.

[121] Shinichi Tachi, Kazunori Tsujimoto, Shin Arai, and Tokuo Kure. Low-temperature dry etching. Journal of Vacuum Science & Technology A: Vacuum, Surfaces, and Films, 9(3):796–803, 1991.

[122] Ayokunle Omosebi and R. Besser. Electron beam assisted patterning and dry etching of nafion membranes. Journal of The Electrochemical Society, 158:D603–D610, 09 2011.

[123] Jakub Mališ, Martin Paidar, Tomas Bystron, Libuše Brožová, Alexander Zhigunov, and Karel Bouzek. Changes in nafion® 117 internal structure and related properties during exposure to elevated temperature and pressure in an aqueous environment. Electrochimica Acta, 262:264–275, 2018.

[124] Jakub Mališ, Petr Mazúr, Martin Paidar, Tomas Bystron, and Karel Bouzek. Nafion 117 stability under conditions of pem water electrolysis at elevated temperature and pressure. International Journal of Hydrogen Energy, 41(4):2177–2188, 2016.

[125] Burin Yodwong, Damien Guilbert, Matheepot Phattanasak, Wattana Kaewmanee, Melika Hinaje, and Gianpaolo Vitale. Faraday's efficiency modeling of a proton exchange membrane electrolyzer based on experimental data. Energies, 13(18), 2020.

[126] RFW Pease. Electron beam lithography. Contemporary Physics, 22(3):265–290, 1981.

[127] Yifang Chen. Nanofabrication by electron beam lithography and its applications: A review. Microelectronic Engineering, 135:57–72, 2015.

[128] Christophe Vieu, F Carcenac, A Pepin, Y Chen, M Mejias, A Lebib, L Manin-Ferlazzo, L Couraud, and H Launois. Electron beam lithography: resolution limits and applications. Applied surface science, 164(1-4):111–117, 2000.

[129] FJ Hohn. Electron beam lithography: its applications. Journal of Vacuum Science & Technology B: Microelectronics Processing and Phenomena, 7(6):1405–1411, 1989.

[130] Ayokunle Omosebi and Ronald S. Besser. Fabrication and performance evaluation of an in-membrane micro-fuel cell. Journal of Power Sources, 242:672–676, 2013.

[131] Zhiyong Xiao, Chunhua Feng, Philip C.H. Chan, and I-Ming Hsing. Monolithically integrated planar microfuel cell arrays. Sensors and Actuators B: Chemical, 132(2):576–586, 2008. Transducers '07/Eurosensors XXI.

[132] Rudolf Ladenstein and Garabed Antranikian. Proteins from hyperthermophiles: Stability and enzymatic catalysis close to the boiling point of water, pages 37–85. Springer Berlin Heidelberg, Berlin, Heidelberg, 1998.

[133] Mengbo Ji and Zidong Wei. A review of water management in polymer electrolyte membrane fuel cells. Energies, 2(4):1057–1106, 2009.

[134] Dilip Natarajan and Trung Van Nguyen. Current distribution in pem fuel cells. part 1: Oxygen and fuel flow rate effects. AIChE Journal, 51(9):2587–2598, 2005.

[135] Ugur Pasaogullari, Chao-Yang Wang, and Ken S Chen. Two-phase transport in polymer electrolyte fuel cells with bilayer cathode gas diffusion media. Journal of the Electrochemical Society, 152(8):A1574, 2005.

[136] Klaus Tüber, David Pócza, and Christopher Hebling. Visualization of water buildup in the cathode of a transparent pem fuel cell. Journal of Power Sources, 124(2):403–414, 2003.

[137] Alex Hakenjos, Harald Muenter, Ursula Wittstadt, and Christopher Hebling. A pem fuel cell for combined measurement of current and temperature distribution, and flow field flooding. Journal of Power Sources, 131(1-2):213–216, 2004.

[138] Trung Van Nguyen and Mack W Knobbe. A liquid water management strategy for pem fuel cell stacks. Journal of Power Sources, 114(1):70–79, 2003.

[139] MW Knobbe, W He, PY Chong, and TV Nguyen. Active gas management for pem fuel cell stacks. Journal of power sources, 138(1-2):94–100, 2004.

[140] H.H. Voss, D.P. Wilkinson, P.G. Pickup, M.C. Johnson, and V. Basura. Anode water removal: A water management and diagnostic technique for solid polymer fuel cells. Electrochimica Acta, 40(3):321–328, 1995. Polymer electrolyte fuel cells.

[141] Hui Li, Yanghua Tang, Zhenwei Wang, Zheng Shi, Shaohong Wu, Datong Song, Jianlu Zhang, Khalid Fatih, Jiujun Zhang, Haijiang Wang, et al. A review of water flooding issues in the proton exchange membrane fuel cell. Journal of Power Sources, 178(1):103–117, 2008.

[142] Felix N Büchi and Supramaniam Srinivasan. Operating proton exchange membrane fuel cells without external humidification of the reactant gases: Fundamental aspects. Journal of the Electrochemical Society, 144(8):2767, 1997.

[143] Richard Hanke-Rauschenbach, M Mangold, and Kai Sundmacher. Bistable current-voltage characteristics of pem fuel cells operated with reduced feed stream humidification. Journal of the Electrochemical Society, 155(2):B97, 2007.

[144] Duksu Hyun and Junbom Kim. Study of external humidification method in proton exchange membrane fuel cell. Journal of Power Sources, 126(1-2):98–103, 2004.

[145] David L Wood III, S Yi Jung, and Trung V Nguyen. Effect of direct liquid water injection and interdigitated flow field on the performance of proton exchange membrane fuel cells. Electrochimica Acta, 43(24):3795–3809, 1998.

[146] Seung Hun Jung, Seok Lae Kim, Min Soo Kim, Yongsun Park, and Tae Won Lim. Experimental study of gas humidification with injectors for automotive pem fuel cell systems. Journal of power sources, 170(2):324–333, 2007.

[147] Xuan Liu, Hang Guo, and Chongfang Ma. Water flooding and two-phase flow in cathode channels of proton exchange membrane fuel cells. Journal of Power Sources, 156(2):267–280, 2006.

[148] Trung V Nguyen. A gas distributor design for proton-exchange-membrane fuel cells. Journal of the Electrochemical Society, 143(5):L103, 1996.

[149] WR Merida, G McLean, and N Djilali. Non-planar architecture for proton exchange membrane fuel cells. Journal of power sources, 102(1-2):178–185, 2001.

[150] Toshihiko Kanezaki, Xianguo Li, and JJ Baschuk. Cross-leakage flow between adjacent flow channels in pem fuel cells. Journal of Power sources, 162(1):415–425, 2006.

[151] Jaewan Park and Xianguo Li. An experimental and numerical investigation on the cross flow through gas diffusion layer in a pem fuel cell with a serpentine flow channel. Journal of Power Sources, 163(2):853–863, 2007.

[152] Tatsumi Kitahara, Hironori Nakajima, and Kyohei Mori. Hydrophilic and hydrophobic double microporous layer coated gas diffusion layer for enhancing performance of polymer electrolyte fuel cells under no-humidification at the cathode. Journal of Power Sources, 199:29–36, 2012.

[153] Regis P Dowd, Cynthia S Day, and Trung Van Nguyen. Engineering the ionic polymer phase surface properties of a pem fuel cell catalyst layer. Journal of The Electrochemical Society, 164(2):F138, 2016.

[154] Abdulnaser Sayma. Computational fluid dynamics. Bookboon, 2009.

[155] Louis Melville Milne-Thomson. Theoretical aerodynamics.

[156] Lewis Fry Richardson. Weather Prediction by numerical process: Richardson, Lewis F (ry); With a new introd. by Sydney Chapman. Dover Publ., 1965.

[157] R. K. Raman, Yogesh Dewang, and Jitendra Raghuwanshi. A review on applications of computational fluid dynamics. 2018.

[158] Lawrence C Davis. Origin of the punnett square. The American Biology Teacher, 55(4):209–212, 1993.

[159] H von Helmholtz. Studien über electrische grenzschichten. Annalen der Physik, 243(7):337–382, 1879.

[160] E Gongadze, S Petersen, U Beck, and U Van Rienen. Classical models of the interface between an electrode and an electrolyte. In COMSOL conference, pages 14–16, 2009.

[161] JF McClendon. On the thickness of the helmholtz double layer. Science, 66(1704):200–200, 1927.

[162] GH Bolt. Analysis of the validity of the gouy-chapman theory of the electric double layer. Journal of Colloid Science, 10(2):206–218, 1955.

[163] GM Torrie and JP Valleau. Electrical double layers. 4. limitations of the gouy-chapman theory. The Journal of Physical Chemistry, 86(16):3251–3257, 1982.

[164] Kevin Spurr. How to calculate capacitors in series and parallel. https://kitronik.co.uk/blogs/resources/how-to-calculate-capacitors-in-series-and-parallel, Jan 2014.

[165] David C Grahame. The electrical double layer and the theory of electrocapillarity. Chemical reviews, 41(3):441–501, 1947.

[166] Masashi Nakamura, Narumasa Sato, Nagahiro Hoshi, and Osami Sakata. Outer helmholtz plane of the electrical double layer formed at the solid electrode–liquid interface. ChemPhysChem, 12(8):1430–1434, 2011.

[167] Max Volmer Kinetik der Phasenbildung and Volmer-Adlershof Aktuell. Max volmer.

[168] Edmund JF Dickinson and Andrew J Wain. The butler-volmer equation in electrochemical theory: Origins, value, and practical application. Journal of Electroanalytical Chemistry, 872:114145, 2020.

[169] Allen J Bard, Larry R Faulkner, et al. Fundamentals and applications. electrochem. Methods, 2(482):580–632, 2001.

[170] Franciscus Rudolphus Antonius Maria Standaert. Analytical fuel cell modelling and exergy analysis of fuel cells. 2000.

[171] Serge I. Gorelsky. Ab initio and Semiempirical Methods. John Wiley Sons, Ltd, 2011.

[172] T. E. Springer, T. A. Zawodzinski, and S. Gottesfeld. Polymer electrolyte fuel cell model. Journal of The Electrochemical Society, 138(8):2334–2342, aug 1991.

[173] J. C. Amphlett, R. M. Baumert, R. F. Mann, B. A. Peppley, P. R. Roberge, and T. J. Harris. Performance modeling of the ballard mark IV solid polymer electrolyte fuel cell: I . mechanistic model development. Journal of The Electrochemical Society, 142(1):1–8, jan 1995.

[174] L. Pisani, G. Murgia, M. Valentini, and B. D'Aguanno. A new semi-empirical approach to performance curves of polymer electrolyte fuel cells. Journal of Power Sources, 108(1):192–203, 2002.

[175] Dawn M. Bernardi and Mark W. Verbrugge. Mathematical model of a gas diffusion electrode bonded to a polymer electrolyte. Aiche Journal, 37:1151–1163, 1991.

[176] Dawn M. Bernardi and Mark W. Verbrugge. A mathematical model of the solid-polymer-electrolyte fuel cell. Journal of The Electrochemical Society, 139(9):2477–2491, sep 1992.

[177] Vladimir Gurau, Hongtan Liu, and Sadik Kakaç. Two-dimensional model for proton exchange membrane fuel cells. AIChE Journal, 44:2410 – 2422, 11 1998.

[178] C. Wang, W. Gu, and Bor Yann Liaw. Micro-macroscopic coupled modeling of batteries and fuel cells: I. model development. Journal of The Electrochemical Society - J ELECTROCHEM SOC, 145:3407–3417, 10 1998.

[179] T. Zhou and H. Liu. 3-d model of proton exchange membrane fuel cells. 366:43–49, 01 2000.

[180] Suhas V Patankar. Numerical heat transfer and fluid flow. CRC press, 2018.

[181] COMSOL Multiphysics. Introduction to comsol multiphysics®. COMSOL Multiphysics, Burlington, MA, accessed Feb, 9:2018, 1998.

[182] Melanie Pfaffe. Which current distribution interface do i use?

[183] https://doc.comsol.com/5.3/doc/com.comsol.help.echem/ ElectrochemistryModuleUsersGuide.pdf.

[184] Robert Byron Bird, Warren Earl Stewart, and Edwin Niblock Lightfoot. Transport Phenomena, Revised 2nd Edition. John Wiley & Sons, 1993.

[185] Ross Taylor and Rajamani Krishna. Multicomponent mass transfer, volume 2. John Wiley & Sons, 1993.

[186] Edward Lansing Cussler. Diffusion: mass transfer in fluid systems. Cambridge university press, 2009.

[187] Libretexts. 18.8: Gibbs energy changes in chemical reactions, Aug 2020.

[188] Libretexts. 16.4: The nernst equation, Aug 2022.

[189] DA Noren and Myron A Hoffman. Clarifying the butler–volmer equation and related approximations for calculating activation losses in solid oxide fuel cell models. Journal of Power Sources, 152:175–181, 2005.

[190] Danlei Li, Chuhong Lin, Christopher Batchelor-McAuley, Lifu Chen, and Richard G. Compton. Tafel analysis in practice. Journal of Electroanalytical Chemistry, 826:117–124, 2018.

[191] Martin Bazant. Study materials | electrochemical energy systems | chemical engineering ..., 2014.

[192] Colleen Spiegel. Polarization curves. `https://www.fuelcellstore.com/blog-section/polarization-curves`.

[193] Francesco Valle. Electrocatalyst degradation in high temperature PEM fuel cells. PhD thesis, 04 2015.

[194] Rafael Linares, Stéphane Raël, Kévin Berger, Melika Hinaje, and Jean Lévêque. Pem single fuel cell as a dedicated power source for high-inductive superconducting coils. International Journal of Hydrogen Energy, 43(11):5913–5921, 2018.

[195] Xiao-Zi Yuan and Haijiang Wang. Pem fuel cell fundamentals. In PEM fuel cell electrocatalysts and catalyst layers, pages 1–87. Springer, 2008.

[196] Sang Moon Kim, Yun Sik Kang, Chiyeong Ahn, Segeun Jang, Minhyoung Kim, Yung-Eun Sung, Sung Jong Yoo, and Mansoo Choi. Prism-patterned nafion membrane for enhanced water transport in polymer electrolyte membrane fuel cell. Journal of Power Sources, 317:19–24, 2016.

[197] Dirk Henkensmeier, Quoc Khanh Dang, N. Nambi Krishnan, Jong Hyun Jang, Hyoung-Juhn Kim, Suk-Woo Nam, and Tae-Hoon Lim. ortho-dichlorobenzene as a pore modifier for pemfc catalyst electrodes and dense nafion membranes with one porous surface. J. Mater. Chem., 22:14602–14607, 2012.

[198] Segeun Jang, Minhyoung Kim, Yun Sik Kang, Yong Whan Choi, Sang Moon Kim, Yung-Eun Sung, and Mansoo Choi. Facile multiscale patterning by creep-assisted sequential imprinting and fuel cell application. ACS Applied Materials & Interfaces, 8(18):11459–11465, 2016. PMID: 27116979.

[199] Francis R Hama, James D Long, and John C Hegarty. On transition from laminar to turbulent flow. Journal of Applied Physics, 28(4):388–394, 1957.